Università di Pisa

Facoltà di Scienze Matematiche Fisiche e Naturali

Corso di Laurea Specialistica in Scienze Fisiche

Anno Accademico 2003–2004

Tesi di Laurea Specialistica

Analysis of the optical background sources in the ANTARES experiment and preliminary studies related to a larger scale detector.

Candidato:
Sara Vecchio

Relatore:
Chiar.mo Prof. Vincenzo Flaminio

Contents

Introduction

Observational Astronomy is probably as ancient as is the very presence of man on earth. The earliest recorded observations, due to Egyptian and Central American Civilisations, go back to about 4000 years b.C., while the first written material on Astronomy is found about 1000 years later. All experimental observations, up to the 17^{th} century had relied on the human eye as an "optical instrument". The situation changed drastically in 1609, when Galileo first made use of the telescope, invented one year earlier by Lippershay, a Dutch spectacles maker.

In the 19^{th} century, the discovery of the Doppler effect and the development of optical spectroscopy allowed again a big step forward, yielding, at the end of the century, the discovery of optical binaries and, around 1915, that of the relationship between the star spectral type and absolute magnitude by Hetzsprung and Russell. The field of Astronomy had gradually developed into the more general one of Astrophysics.

All observations up to the 20^{th} century were done in the visible region of the spectrum. Astrophysics, aiming at an understanding of the Physical Processes taking place in stars, galaxies, galaxy clusters etc. could not have developed to the advanced stage in which we find it today, without an extension of the range of wavelengths used. Thus, it would not be possible to study processes occurring in the region of the center of our galaxy, without the use of detectors working in the infrared and in the radiowaves. Analogously, it is only thanks to instruments working in the radio, X and γ ray regions that pulsars have been discovered and studied in detail. A giant step forward has come with the advent of satellite-born X and γ ray detectors.

Detectors sensitive to higher and higher energy γ rays are now being built. They fall either in the category of satellite-born tracking-calorimetric detectors, characterised by an acceptance in energy limited to $\approx 300\ GeV$ (for the forthcoming experiment GLAST) or in that of large area surface detectors, using the Cerenkov technique, that can reach the energy range above $10^{10} \div 10^{11}\ GeV$,

where the flux has fallen to very small values. All these detectors can, however, cover a region in space around the Earth limited to about $100\ Mpc$ at $10\ TeV$, because of γ ray absorption by the 3^oK cosmic microwave background.

Ground-based hadron detectors and underground muon detectors have been used since the beginning of the 20^{th} century, for the study of cosmic rays. These may also bring useful information on the Physics taking place in stars, galaxies, pulsars, etc. However, only the highest energy protons ($E > 10^{10}\ GeV$) could possibly point to their sources and, as for the photons, the region which can be explored is limited by interaction with the extragalactic backgrounds.

The neutrino, on the other hand, thanks to its tiny cross section and lack of electric charge, is a new excellent candidate for probe able to bring information from objects located at large distances and, what is even more important, from the core of such objects. In chapter 1, I will discuss advantages of using neutrinos as probes of the Universe. Detection of MeV neutrinos from the nuclear reactions in the core of the Sun or from supernova explosions in our galactic neighbourhood is by now largely used. However the main interest of neutrino astronomy at the moment is focused on neutrinos with energy above $GeV \div TeV$ for several reasons: the neutrino cross section as well as the muon range and the detector angular resolution increase with energy, large natural target media (like water, ice or the atmosphere) can be used and much less is known on the underlying astrophysics. In the same chapter 1, I will briefly report the astrophysics and particle-physics problems that high energy neutrino astronomy may help to solve, like e.g. the understanding of the acceleration mechanisms for high energy cosmic rays or of the composition of the "dark matter".

The advantage that νs have compared to other particles, the tiny cross section, turns into a disadvantage when one tries to detect them. Enormous detectors are needed, and they have moreover to be well screened from the large cosmic ray muon background, through the use of massive layers of inert material.
The only means of detection that appears feasible for the low fluxes of high energy neutrinos is through the use of deep lake or sea water as target, combined with large photomultiplier arrays to capture the Cerenkov light emitted by charged secondaries produced in the ν interaction.

A first attempt to build such a detector was made more than twenty years ago by the DUMAND collaboration, who chose a site close to the Hawaii islands. The experiment demonstrated that muons could indeed be detected, but it was afterwards prematurely terminated. The first real detection of neutrino-induced muons in a similar setup was achieved only much later by a Russian group working at great depths in Lake Baikal. In chapter 2, I will discuss the general features of

the detection technique used in a Čerenkov neutrino telescope. I will briefly describe the main results obtained up to now by the experiments which are already taking data, and summarize the status of new experiments which are still under development.

The work described in this document has been carried out in the framework of the ANTARES experiment which aims at building a neutrino telescope in the Mediterranean. The ANTARES architecture, electronics and data acquisition are briefly illustrated in chapter 3.

Since bioluminescence and ^{40}K radioactive decay are a non-negligible source of background in any experiment performed in the sea, I have analysed data collected by a prototype string of ANTARES in 2003, specifically aiming at a quantification and charaterisation of these noise sources. The analysis methods and the results obtained are described in chapter 4.

In addition I have tried to understand what improvement could be brought in by the use of a photodetector of a new type, the hybrid photodiode (HPD). In this context I have designed, making use of commercial software, an HPD with a convenient geometry and verified the possibility of its use in a neutrino telescope by means of a modified version of the ANTARES Monte Carlo. Details of the HPD and of the experimental layout, together with the performance of such detector, are given in chapter 5.

A discussion of the main results obtained and conclusions are given in the closing chapter.

Chapter 1

High energy neutrino astronomy

1.1 A new glance at the edge of the Universe

In order to investigate phenomena very far from us, it is important to use particles whose direction is not scrambeld during propagation. Therefore, first of all, particles must not be affected by the ambient magnetic fields. Good candidates may then be neutral radiations - such as gamma rays, gravitational waves, neutrinos - or charged and massive stable particles (like protons) with an extremely high energy.

Gravitational waves are predicted by General Relativity, which is one of the most supported theories in science. The best evidence, for the moment, that gravitational waves exist comes from the orbits of close binary pulsars; binary systems are predicted to emit gravitational waves: it has been found that the orbits decay at exactly the correct rate predicted by the theory of gravitational radiation and have no other explanation available. Nevertheless, gravitational waves have not yet been detected, mostly because of the difficulty involved in the endeavour.

Proton astronomy may be possible at EeV energies and above: the arrival directions of electrically charged cosmic rays are no longer distorted by the magnetic field of our own galaxy and the Bremsstrahlung and syncrotron radiation - which make electrons totally unusable - are negligible. Protons point back to their sources with an accuracy determined by their gyroradius in the intergalactic magnetic field B: $\theta \approx \frac{d}{R_{gyro}} = \frac{Bd}{E}$, where d is the distance to the source. Scaled to units relevant to the problem, $\frac{\theta}{0.1^o} \approx \frac{B}{10^{-9}\ G}\ \frac{d}{1\ Mpc}\ \frac{3{\cdot}10^{20}\ eV}{E}$.
Speculations on the strength of the inter-galactic magnetic field range from 10^{-12} to $10^{-7}\ G$ in the local cluster. For a distance of $100\ Mpc$, the angular resolution may therefore be anywhere from sub-degree to almost zero. It is still possible that

the arrival directions of the highest energy cosmic rays provide information on the location of their sources. However, in principle, if the GZK-cutoff were confirmed (see section 1.2) it would rule out the possibility of proton-astronomy as a means of investigation: protons would be unable to access regions at distances above $50\ Mpc$ for energies larger than $50\ EeV$.

Neither is the Universe transparent to photons of TeV[1] energy and above: energetic photons are absorbed on infrared and microwave background by pair production of electrons $\gamma + \gamma_{bg} \rightarrow e^+ + e^-$ above a threshold $E_\gamma \approx (2m_e)^2/4\epsilon_{bg}$ for the high-energy photon.
The equation implies that TeV photons are absorbed on infrared light, PeV photons on the cosmic microwave background and EeV photons on radio-waves.

Only neutrinos - electrically neutral and weakly interacting - can reach us without attenuation from the edge of the Universe or simply from dense cores of potential, both close or distant, sources. The existence of point-like neutrino sources is still unproved, although different astronomic objects are considered capable of emitting high energy neutrinos, as predicted by different theoretical models (see section 1.3). Simultaneous source detection through neutrino and gamma astronomy would bring a big progress in the check of such theoretical models.

The development of novel ways of looking into space has also the appeal of possibly leading to the discovery of unanticipated class of phenomena hidden to the "standard" astronomy.

1.2 Cosmic rays and open problems

Since 1912, long before the existence of the neutrino was suspected, it was known that an extra-terrestrial charged radiation arrived on Earth. We know that primary cosmic rays consist of an isotropic flux of ionized atomic nuclei (mainly protons, 89%, and helium) that reach the Earth at a rate of thousands per m^2 and per s (see figure 1.1) and interact with the atmosphere producing a large flux of secondary particles. It is also accepted that the origin of high energy cosmic rays must be intimately related to the origin of high energy cosmic neutrinos, though we still do not know exactly how and where they are accelerated.

The spectrum of primary cosmic ray has now been measured for energies up to $10^{20}\ eV$, as shown in figure 1.1. Above 10 GeV, the spectrum can be characterized by power-laws over wide ranges of energies. Up to a steepening point at $\approx 4 \cdot$

[1] $10\ TeV$-photons cannot acces regions at beyond $100\ Mpc$.

$10^{15}\ eV$, called *knee*, the flux is proportional to $E^{-2.7}$, above this energy the power index changes from 2.7 to 3. Above $5 \cdot 10^{18}\ eV$, a point called *ankle*, the power law is again $E^{-2.7}$.

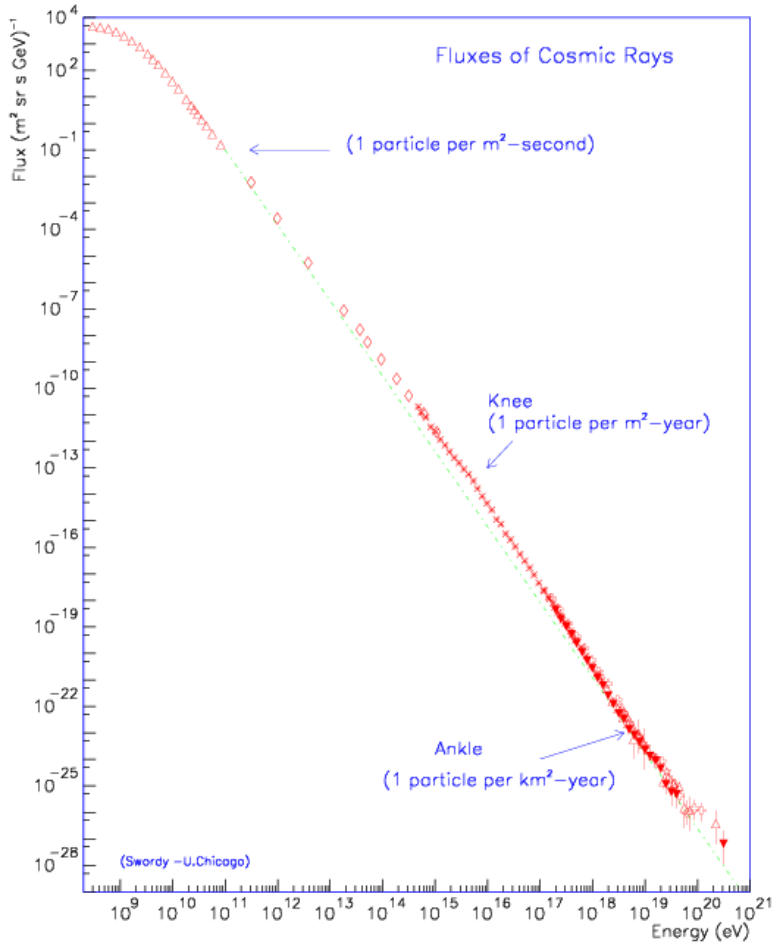

Figure 1.1: Primary Cosmic Rays Spectrum.

This large uniformity of the power-law index over many orders of magnitude could be explained by the analogy of acceleration mechanisms at all energies, and the nodal points (*knee*, *ankle* and maybe a *toe* at higher energies) may be

interpreted as a change in particles' origin and composition.

There is evidence that the highest energy[2] cosmic rays are extra-galactic: they cannot be contained by the magnetic field of our galaxy because their gyroradius far exceeds its dimension (see section 1.2.1) and they do not show the spatial anisotropy expected for particles of galactic or super-galactic origin.

However, elementary particle physics dictates a universal and robust upper limit on the energy of cosmic rays. The photoproduction of the Δ-resonance, $p+\gamma_{CMB} \rightarrow \Delta \rightarrow \pi+N$, becomes the major source of proton energy loss once the threshold energy $E_p \approx (m_\Delta^2 - m_p^2)/2\epsilon_\gamma \approx 5 \cdot 10^{19}\ eV$ is reached. The absorption length, which establishes the so-called Greisen-Kuzmin-Zatsepin (GZK) cutoff, is $\lambda_{\gamma p} \approx (n_{CMB} \cdot \sigma_{p+\gamma})^{-1} \lesssim 10\ Mpc$ when the proton energy exceeds $50\ EeV$. But particles with energy beyond this limit have been observed by Haverah Park, AGASA, Fly's Eye and other experiments [58].

There are three possible solutions for the inconsistency of data with predictions:

- the highest energy cosmic rays might be nuclei different from protons.
- proton sources might be closer than we think
- the original energy of cosmic rays might be much higher than we observe (see section 1.2.1)

A rough estimate of energies reachable via the known acceleration mechanisms and our knowledge of the distribution of nearby galaxies show that the last two possibilities are unlikely.

1.2.1 Reachable energy in the acceleration process

There cannot be static electric fields in the universe, because the particle flow would quickly destroy them. Acceleration is therefore due only to electric fields produced by variable magnetic fields.

The standard model for the cosmic ray acceleration is known as *first order Fermi mechanism* [60] and it consists in the acceleration by shockwaves in the interstellar medium. This mechanism is able to explain the shape of the cosmic ray spectrum, however the existence of the ultra-high energy cosmic rays above $10^{11}\ GeV$ is a serious challenge for the model.

[2] Above the ankle: $10^{18}\ eV$.

In order to accelerate a proton ($Z = 1$) to an energy E in a magnetic field B, the size R of the accelerator must be larger than the gyroradius of the particle: that is to say, the accelerating magnetic field must contain the particle orbit. This condition yields a maximum energy

$$E = \gamma(Z)BR \tag{1.1}$$

by dimensional consideration only. The γ-factor has been included to take into account the possibility that we may not be at rest in the frame of the cosmic accelerator.

The acceleration can take place only in dense regions where huge gravitational forces create relativistic particle flows. All speculations involve collapsed objects and we can therefore replace R by the Schwartzschild radius $\rho \approx GM/c^2$ and obtain $E \propto \gamma(Z)BM$. Given the microgauss magnetic field intensity in our galaxy, no structures are large or massive enough to reach the energies of the highest energy cosmic rays. This rough analysis therefore limits their sources to extra-galactic objects, as those shown above the red lines in figure 1.2. As shown by the green line in the same figure, if primaries have bigger charge and mass than protons the constraints on the acceleration sites are lowered.

However it must be pointed out that the limit stated in equation 1.1 holds for perfect accelerators with optimized design and perfect alignment of magnets. The more realistic approach involving a complete description of the acceleration mechanism occurring in shock waves turns out to have an efficiency of about 10%.

The astrophysics problem of obtaining such high-energy particles is so daunting that many believe that cosmic rays are not the beams of cosmic accelerators but the decay products of remnants from the early Universe, such as topological defects associated with a Grand Unified Theory (GUT) phase transition (section 1.3).

1.3 Neutrino signature for different sources

Accelerating particles to TeV energy and above requires relativistic, massive bulk flows. In such situation, accelerated particles are likely to pass through intense radiation fields or dense gas clouds surrounding the bulk. This leads to the production of secondary photons and neutrinos associated with the primary cosmic ray beam. The target material, either a gas of particles or of photons, is likely to be tenuous enough so that the primary and the photon beams are only partially attenuated. However, shrouded sources from which only neutrinos can emerge, are

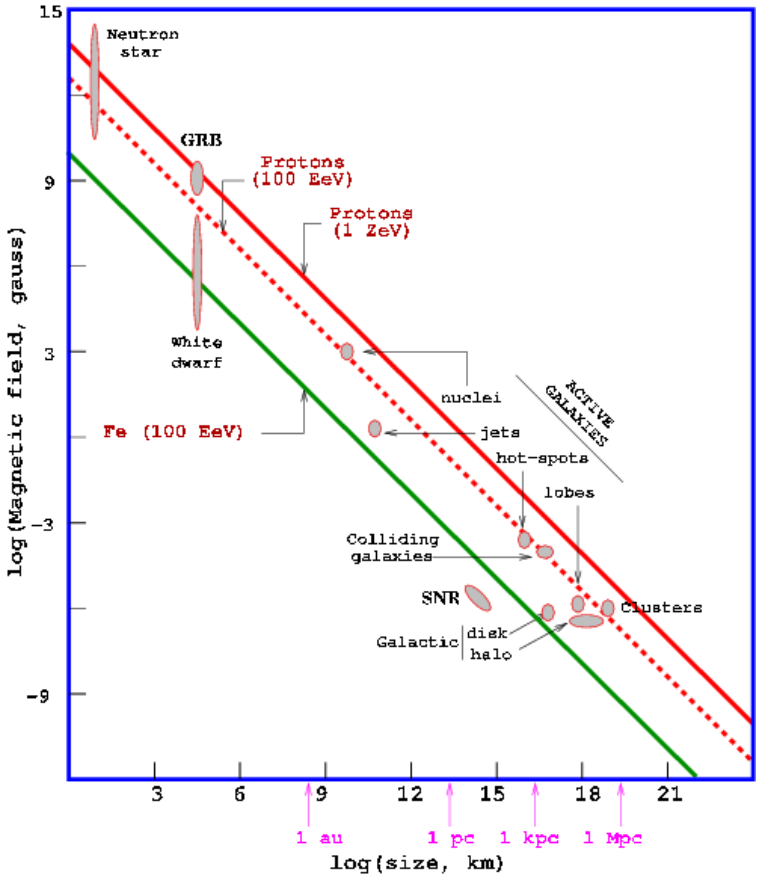

Figure 1.2: Hillas Plot. Red, green and dotted lines show the relation between the magnetic field and the size of an accelerator which follows from equation 1.1 once energy and charge of the accelerated particle are fixed. Astrophysics objects placed above a line are candidate sites for acceleration.

also a possibility. These "hidden" objects cannot be the sources of cosmic rays, conventional astronomy does not reveal them, and as a consequence no prediction on neutrino flux can be made for them.

On the contrary, such a prediction of neutrino flux for a "trasparent" source, in which every observed cosmic ray interacts once and only once, is referred to as the Waxman-Bahcall (W&B) flux. The W&B limit [61], derived normalizing the observed cosmic ray spectrum at $10\ EeV$ and extrapolating it to lower energies using an E^{-2} source spectrum, results in a maximum yield of 200 events per

$yr \cdot km^2$ in a large water-Čerenkov detector.

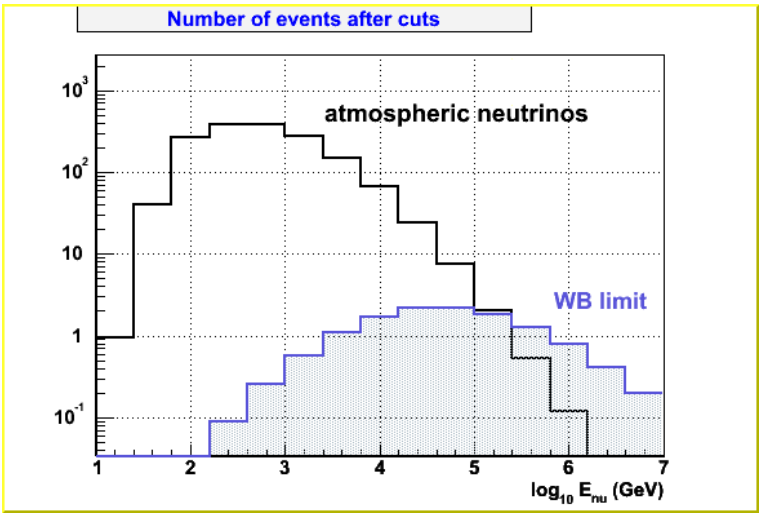

Figure 1.3: Atmospheric neutrino flux, which is a background for high energy neutrino astronomy, compared with the upper limit on neutrino flux from extragalactic sources as derived by Waxman and Bahcall. Spectra shown for the ANTARES sensitivity, after reconstruction and quality cuts.

The observed gamma ray fluxes may also constrain the flux of potential neutrino sources, if a hadronic model is assumed for gamma production: for every parent neutral pion (decaying into two gamma rays), a charged pion (thus a neutrino, from $\pi \rightarrow l + \nu$) is produced. The resulting ν-flux would then turn out to be of the same order of magnitude as that predicted by W&B. It is important to realize, though, that the present energy resolution of existing or planned detectors is not adequate to disentangle the hadronic contribuition $\pi^0 \rightarrow \gamma + \gamma$ to the γ spectrum.

The list of proposed sources is quite long. Below we recall the main neutrino sources associated with the observed cosmic and gamma rays. Theoretical calculations lead to predictions of a few tens of events per km^2 and per year in a undersea detector, for each class of sources; but the arbitrariness of some model assumption should invite to consider these numbers with caution.

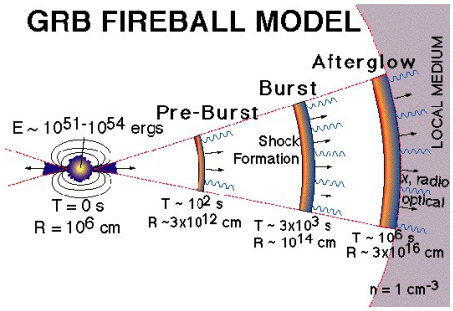

Figure 1.4: The GRB fireball model.

Gamma Ray Bursts (GRB) Gamma Ray Bursts, cosmological events releasing $10^{51} \div 10^{54}\, erg/s$ over a duration of seconds or tens of seconds, are perhaps the best motivated source for high-energy neutrinos. Although we still do not understand the internal mechanisms that generate GRB, the model of a relativistic expanding fireball provides us with a successful phenomenology accommodating observations like the spectrum and the light curve. It is very likely that GRB are generated in some kind of catastrophic process involving dying massive stars or cohalescence of compact objects like black holes or neutron stars.
Several mechanisms have been proposed for the production of neutrinos, and moreover before to state a flux prediction we need to consider the variations that may occur in the dynamics from burst to burst or simply the uncertainties due to the lack of knowledge about the GRB mechanism itself.

Thermal Neutrinos (MeV). The core collapse of massive stars is, arguably, the most promising mechanism for generating GRB. As with supernovae, GRB are supposed to radiate the vast majority of their initial energy as thermal neutrinos - though the spectrum may be expected at a higher average temperature than in the supernova case: the average neutrino energy will be around $100\ MeV$. Neutrinos with this energy are below threshold for the detection methods used in large area neutrino telescopes.

Stellar Core Collapse (TeV). The fireball produced is likely to be beamed in jets along the collapsed object's rotation axis. If the jets successfully emerge from the stellar envelope, a GRB results; but failed "invisible" jets, which do not emerge and do not produce a GRB, will still produce observable neutrinos.

Shocked Protons (PeV). Accelerated protons can interact with fireball gamma rays and produce pions, predominantly via the Δ-resonant process $p+\gamma \rightarrow N+\pi$. When the target are instead $eV \div KeV$ backshock photons[3], the energy of the produced neutrinos will be lower ($TeV \div EeV$). While astronomical observations provide information on the fireball gamma rays, the proton flux is a matter of speculation.

Decoupled Neutrons (GeV). The conversion of radiation into kinetic energy in

[3]Radiated by electrons and positrons in the reverse shock that propagates back into the burst ejecta.

the fireball will accelerate neutrons along with protons, especially if the progenitor involves neutron stars. Neutrons and protons are initially coupled by nuclear elastic scattering, but if the expansion of the fireball is sufficiently rapid they will decouple from each other. If their relative speed is sufficiently high, proton-neutron interactions will be the source of pions which decay into GeV neutrinos.

Active Galactic Nuclei (AGN): Blazars Although their isotropic luminosities of $10^{45} \div 10^{49}\ erg/s$ is lower than the one of GRBs, Active Galactic Nuclei radiate this luminosity over much longer time periods with regular flares extending from fraction of a day to years. Flares from all AGN are believed to be produced by relativistic jets projected out of an extremely massive ($10^7 M_\odot$ or more) accreting black hole located in the center of galaxies.

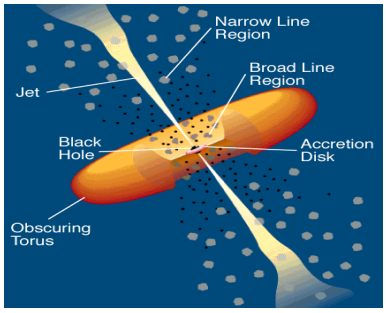

Figure 1.5: Schematic view of an AGN.

Blazars are a particular class of AGN with the boosted jets pointed to the observer, which are therefore seen through emission of γ rays, together with the standard AGN emission spectrum. The radio emission from the jets is mainly electron synchrotron radiation, which is an indirect evidence for particle acceleration. In addition, sequential images of the radio jets have shown distinct moving "blobs" of material exiting the nucleus with relativistic velocities.

Highly Shocked Protons (EeV). If protons are present in blazar jets, they may interact with photons via the Δ-resonance to generate pions which then decay into EeV neutrinos. This process is similar to the process generating PeV and EeV neutrinos in GRB, but the Lorentz factor of the motion of the blob is typically smaller than for GRB and the geometry of the shocked material is a sphere rather than a shell.

Moderately Shocked Protons (TeV). In line-emitting blazars, external photons with energies in the $KeV \div MeV$ range are known to exist and protons of lower energy relative to those considered in the previous paragraph can photoproduce pions by interacting with them.

Other Sources Associated with Stellar Objects Other theorized neutrino sources associated with compact objects include supernovae exploding into the interstellar medium, X-ray binaries, microquasars and even the Sun, any of which could

provide observable fluxes of high-energy (*TeV*) neutrinos.

Propagation of Cosmic Rays The photopion production following collision of protons with cosmic microwave background is among the most likely sources of high-energy neutrinos and the most easily predictable. Furthermore, cosmic rays interact with the hydrogen concentrated in the galactic plane producing high-energy neutrinos. It has also been proposed that cosmic neutrinos may themselves produce cosmic rays and neutrinos in interactions with relic neutrinos $\nu + \nu_{bg} \rightarrow Z^0 \rightarrow any$: this is called the Z-burst mechanism.

Top-Down Models: Dark Matter, Primordial Black Holes and Topological Defects In recent years it has become generally accepted by astrophysicists that most of the matter in the universe is *dark matter*. The clearest evidence for this is the observed flatness of the rotation curves of spiral galaxies, which implies a dynamical mass far in excess of that accounted for by the constituent stars and gas. Constraints from the observed abundances of light elements indicate that much of the dark matter in the cosmos must be non-barionic. No presently known particle has the required properties, but a good theoretical candidate are the stable neutral particles expected in most versions of supersymmetry theory.

The lightest supersymmetric particle (neutralino, labelled as χ), or other Weakly Interacting Massive Particles (WIMPs) proposed as particle candidates for cold dark matter, should become gravitationally trapped in the Sun, Earth or galactic center. There, they would annihilate generating high-energy neutrinos observable in neutrino telescopes.

Another class of dark matter candidates are superheavy particles with GUT-scale masses that may generate the ultra high-energy cosmic rays by decay or annihilation, as well as solve the dark matter problem. These will also generate a substantial neutrino flux. Extremely high-energy neutrinos are also predicted in a wide variety of top-down scenarios invoked to produce cosmic rays, including decaying monopoles, vibrating cosmic strings and Hawking radiation from primordial black holes.

However, conventional particle physics implies that ultra high energy jets fragment predominantly into photons with a small admixture of protons, and this seems to be in disagreement with mounting evidence that the UHECRs are not photons. This does not necessarily rule out superheavy particles, because the uncertainties associated with the universal radio backgroundand the strength of intergalactic magnetic fields leave open the possibility that photons may be depleted

from the cosmic ray spectrum near $10^{20}\ eV$.

Chapter 2

Present status of very high energy neutrino experiments

2.1 Neutrino Telescopes

2.1.1 Detection techniques

Neutrino detection at energies larger than $100\ GeV$, requires large detector volumes as a consequence of the low cross-section and flux expected. Large-scale neutrino detectors, with dimensions of several thousands cubic meters for the instrumented volumes, primarily focus on detection of muon neutrinos. From the detection of muons following the CC neutrino interaction, pointing accuracies of one degree[1] are achieved for the parent neutrino after few hundreds of GeV. This is comparable to the angular resolution achieved in satellite-borne γ ray detectors, covering the multi-GeV energy region, or in large area ground based atmospheric telescopes and (γ and particle) air shower detector arrays, covering the energy region above few TeV [62].

If the incoming muon neutrino undergoes a charged current interaction with a nucleus, a muon is produced. Given the long range of muons in water[2], one can instrument a large sensitive volume with a reasonable number of phototubes. The neutrino interaction may be detected not only if it takes place inside the instrumented volume but also at distances larger than $1\ km$ ahead of the detector, as long as the muon reaches it. Therefore the effective volume of the detector is

[1] See following sections for details of single experiments.

[2] About $360\ m$ at $100\ GeV$. [2]

substantially larger than the instrumented volume.

The muon detection utilizes the Čerenkov light generated around the track in a transparent medium. The energy threshold is $160\ MeV$ for $n = 1.33$, and both liquid and solid water have a refraction index around that value in the wavelength window $300 \div 600\ nm$ [66]. The only practically possible medium is water, in liquid or solid form. An example of Čerenkov light spectrum is shown in figure 2.1. The Čerenkov light is detected by an array of large photomultiplier tubes (PMT)

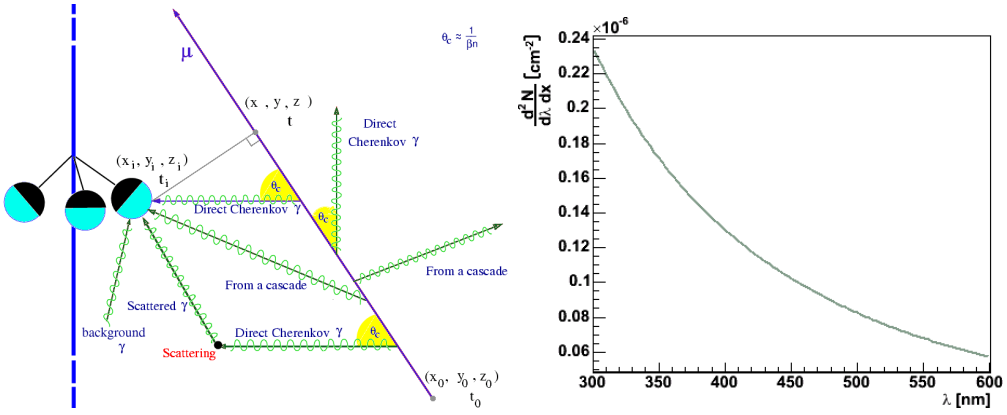

Figure 2.1: *Left:* Schematic view of the possible origins of the photons that produce signals in an optical module. *Right:* Differential light yeld per unit path length from Cherenkov light in salt water computed using the refraction index measured at the ANTARES site [3].

distributed inside the medium. From the time evolution of the Čerenkov light it is possible to obtain the parameters of the muon track. The signals in the PMT are predominantly from single photoelectrons and the required time resolution is a few ns.

In the high-energy neutrino telescopes the emphasis is placed on the directional resolution, of great importance in the search for point sources. Energy resolution is intrinsically limited, since the energy information is obtained from the amount of light produced by electromagnetic showers, generated along the muon path. In those cases in which the neutrino interaction occurs inside the array, also the light from the hadron cascade at the vertex can be used for an estimate of the energy. For fully contained events, where both the start and stop points of the muon track are within the detector, it may be possible to deduce the muon energy from the track length. This only works for the lower energy part of the muon spectrum, below $\approx\ 50 \div 100\ GeV$, and is mostly of value for neutrino oscillation

measurements using fairly low-energy atmospheric neutrinos.

Electron-neutrino measurements are more difficult. The effective volume is reduced, only electron-neutrino events occurring inside, or close to, the instrumented volume will be detected. The electron shower produces a large amount of light, but within a relatively small volume. Having full containment is useful for these events, in order to identify them positively and exclude possible backgrounds.

If the incoming neutrino undergoes a neutral current interaction, only very energetic events may be detected, through hadronic cascades. Nobody has demonstrated yet that we can even get coarse directional information using the cascade events [13].

2.1.2 Background sources

Background rejection is of prime importance in neutrino telescopes. Two types of background are present: physical background due to muons or neutrinos of non-astrophysical origin and detector-related optical background. The physical background is due to cosmic rays interacting in the atmosphere above the detector and producing a large number of atmospheric muons, via a hadronic cascade and subsequent π/K decays. The rejection of these events requires that the neutrino detector be located deep under as much water or ice as practically possible. Still it is not possible to clearly interpret downward going muons as induced by neutrinos: at a depth of $2\ km$, the flux of surviving atmospheric muons exceeds that of ν-induced muons reaching the detector by about 6 orders of magnitude (see figure 2.2). Only those muons that are observed to move upwards (or nearly horizontally) can be neutrino event candidates. For those the atmospheric muon background is filtered away by the large mass of the Earth and only neutrinos remain. Upgoing muons may come from atmospheric neutrinos, i.e. neutrinos produced by the interaction of cosmic rays in the atmosphere, but they may be rejected by applying an energy cut. Misinterpretation of a small fraction ($\approx\ 10^{-6}$) of the atmospheric muon events as up-going tracks would be a possible background to the neutrinos. With increasing depth (i.e. water shielding) and array size the risk for misinterpretations will be reduced. Already in the present day telescopes the possible misinterpretations are mastered by the application of strong selective cuts, at the expense of some efficiency.

The detector-related optical background depends on the surrounding medium. For example, in an under-ice detector the only kind of background comes from radioactive decays within the glass sphere and the surroundings. In an underwater

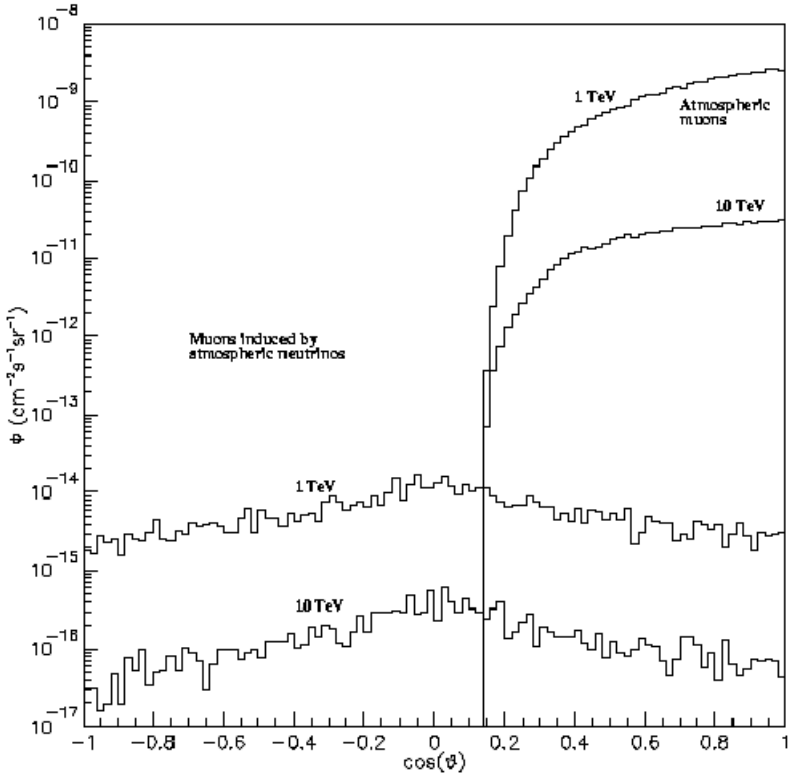

Figure 2.2: Atmosferic muons and muons induced by atmospheric neutrinos as a function of the zenith angle for a detector depth of $2300\ m$.

detector an additional contribution from chemiluminescence (see section 4.1.2) is present, and if the detector is deployed in the sea instead of fresh water, it also suffers from the decay of radioactive isotopes present in salt water. Since both the atmospheric-muon background and bioluminescence decrease with increasing depth, the only way to improve the signal to noise ratio is to place the detector at the largest possible depth.

2.1.3 Detector parameters

Neutrino astronomy is a signal-limited science: there is nothing one can do to increase the signal at the production site, and it has already been stated that huge detectors must be built. In order to quantify and compare acceptance of different neutrino telescopes for specific sources, an *effective area* is computed by Monte

Carlo simulations.

One in general defines, to begin with, an *effective volume* as follows. A volume V_{gen}, larger than the detector volume, is arbitrarily chosen and events are generated within this volume for many different values of the neutrino energy E_ν and incoming direction (θ_ν, ϕ_ν). Let $N_{gen}(E_\nu, \theta_\nu, \phi_\nu)$ be the number of generated events for each given set of values of the kinematic variables E_ν, θ_ν and ϕ_ν. Assume now that $N_x(E_\nu, \theta_\nu, \phi_\nu)$ events survive after applying a given requirement x, which may consist in: trigger requirements, trigger + reconstruction requirements or trigger + reconstruction + quality requirements. The effective volume is computed as:

$$V_{eff}(E_\nu, \theta_\nu, \phi_\nu) \equiv \frac{N_x(E_\nu, \theta_\nu, \phi_\nu)}{N_{gen}(E_\nu, \theta_\nu, \phi_\nu)} V_{gen}. \tag{2.1}$$

The effective volume can be combined with the target nucleon density (ρN_A) and the neutrino cross-section per nucleon $\sigma(E_\nu)$ to obtain a quantity having dimension of area:

$$A_{eff}^{(\nu \ at \ detector)}(E_\nu, \theta_\nu, \phi_\nu) \equiv \rho N_A \cdot V_{eff}(E_\nu, \theta_\nu, \phi_\nu) \cdot \sigma(E_\nu). \tag{2.2}$$

This effective area is then combined with the differental neutrino fluxes at the detector to give event rates.
Absorption in the earth can be expressed as $P_{Earth}(E_\nu, \theta_\nu) = e^{-N_A \sigma(E_\nu) \int \rho dl}$, hence the effective area for neutrinos at the detector can be converted to an effective area for neutrinos before entering the earth multiplying by this probability.

An effective area can also be usefully defined directly for muon reconstruction as a function of muon parameters:

$$A_{eff}(E_\mu, \theta_\mu) \equiv \frac{N_x(E_\mu, \theta_\mu)}{N_{gen}(E_\mu, \theta_\mu} A_{gen}(\theta_\mu). \tag{2.3}$$

In general, for a cylindrical "can" generation (see appendix B), the zenith angle dependent surface area is $A_{gen}(\theta) = 2rh \sin\theta + \pi r^2 cos\theta$. The effective area can be averaged over isotropic upward going muons, leaving only the energy dependence. This second definition, relative to muon detection, has the advantage of being independent from both the ν-physics and ν-fluxes: it parametrizes only the detector capabilities, free from any bias due to our present knowledge. Effective areas for neutrino telescopes are usually quoted for muons rather than for neutrinos.

A fundamental parameter in a neutrino telescope is the angular resolution in event reconstruction. A poor resolution, in fact, compromises the ability to search

for neutrino sources within definite small regions of the sky from which signals have been detected using different probes. The angular resolution is usually expressed by the median value of the difference between the true and reconstructed angle. The angular resolution is limited by the PMTs density, the optical properties of the medium, and the recostruction algorithm.

At high energies, the light yield is extremely high and the tracks are long enough that highly efficient detectors may be constructed with low PMT density. At low energies, however, the angle between the incoming neutrino and the generated lepton dominates the detector resolution.

Among the water optical properties, greatest importance assumes the photon scattering length. If photons are scattered, information on the direction of the originating Čerenkov cone is lost. If they undergo a large number of scatterings before being detected, photons are completely useless and the reconstruction algorithm may not converge. One can manage to reconstruct tracks with reasonable accuracy by demanding hits with very large pulse heights on a large number of PMTs, on the assumption that high pulse heights will correspond to unscattered photons. But this is then paid with a significant decrease of the effective area.

A quantity which is usually adopted to compare characteristics of different sites is the *effective scattering length* $\lambda_{eff} = \lambda_{scatt}/(1 - \langle\cos\theta\rangle)$, [3] which represents the length after which the direction of the Čerenkov photon is essentially randomized.

The angular resolution is also compromised by the background hits which are not well rejected by the filters within the reconstruction algorithm. Further improvements could be then obtained by reducing the background contamination. An attempt in this direction is presented in chapter 5.

[3] $\langle\cos\theta\rangle = \int_{4\pi} \cos\theta \cdot f(\theta) d\Omega$ is the mean cosine of the scattering angle, averaged with the differential cross section $f(\theta)$ for each scattering process: $\int_{4\pi} f(\theta) d\Omega = 1$.

2.2 Present projects

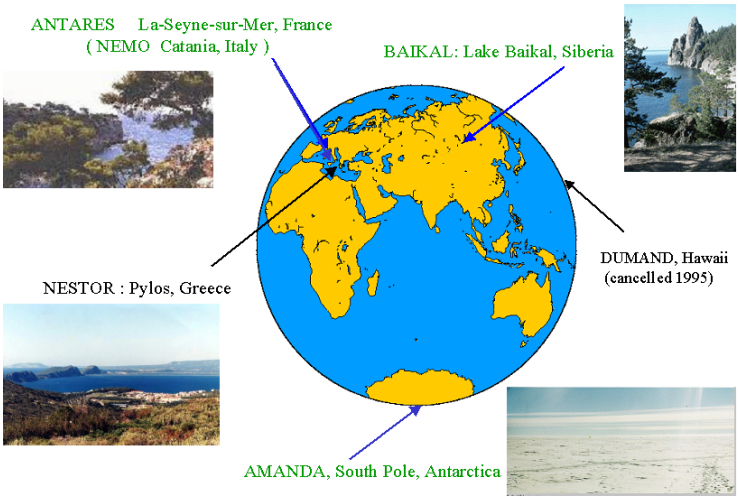

Figure 2.3: Location of present neutrino telescope projects.

There are five major collaborations working on the construction of large neutrino telescopes: Baikal, AMANDA, ANTARES, NESTOR and NEMO. An earlier projet, DUMAND, aimed at installing a telescope deep in the Pacific Ocean close to Hawaii, was proposed at the end of the 1970s after several years of discussions. Prototype deployments of DUMAND were performed in the 1980s and beginning of the 1990s. The experiment was plagued by technical problems and has been cancelled, but the collaboration demonstrated the feasibility of such a project.

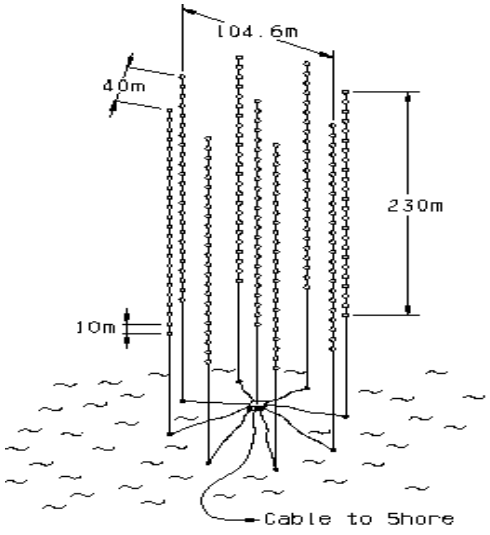

Figure 2.4: The DUMAND II detector.

The Baikal and the AMANDA projects have both built working detectors and have demonstrated their ability to identify neutrino events.

The ANTARES, NESTOR and NEMO projects, all three in the Mediterranean, are in a state of development and prototyping. The realization of the ANTARES

demonstrator will be a fundamental step to acquire experience in submarine technology and to seriously begin the activity of neutrino astronomy in the Mediterranean.

2.3 Baikal

The Baikal telescope is installed in Lake Baikal, Siberia, at a depth of $1100\ m$. It has been built in successive steps; the first part containing 36 optical modules was ready in 1993. Since 1998 [5] the array has reached 192 optical modules, NT-200 (see fig. 2.5). These modules are arranged along 8 strings, one central string and seven strings on a circle with $22\ m$ radius. The instrumented height is about $75\ m$. The system is installed $3.6\ km$ from shore[4]. The thick ice surface layer, which forms during the cold season, provides a stable platform at the end of winter. The array is time-calibrated by two nitrogen lasers. Three underwater electrical cables connect the detector with the shore station. The whole system is retrievable for maintenance and reconfigurations.

The Baikal optical modules contain a special type of photomultiplier tube, the QUASAR. In this tube the photoelectrons are accelerated by a $25\ kV$ potential difference from the photo-cathode to a centrally positioned scintillator. The scintillator is placed on the entrance window of an ordinary PMT. The largest QUASAR has a diameter of $37\ cm$. The optical modules are installed in close pairs. They are operated in a local coincidence mode to suppress the high count rate from PMT-noise and from chemiluminescence down to a few hundred Hz.

The main trigger in the array is formed requiring a reasonable number[5] of these local coincidences within $500\ ns$. For such events, amplitude and time of all fired channels are digitized and sent to shore. Another trigger searches for clusters of sequential coincidences occurring in the characteristic way of a slowly moving object, e.g. a GUT-monopole.

Initially, half of the PMTs were installed looking upwards. The light transmission to these tubes decreased by 50% after 150 days due to sedimentation on the top surface. Hence, in the presently installed array, almost all tubes are facing downwards.

The maximum light absorption length between 470 and $500\ nm$ is $20 \pm 2\ m$

[4]The opposite shore is about $30\ km$ away. The collaboration has recently tuned the reconstruction program well enough to see the effects of the lake shore terrain in the angular distribution of reconstructed atmospheric muons.

[5]Typically set to 3 or 4.

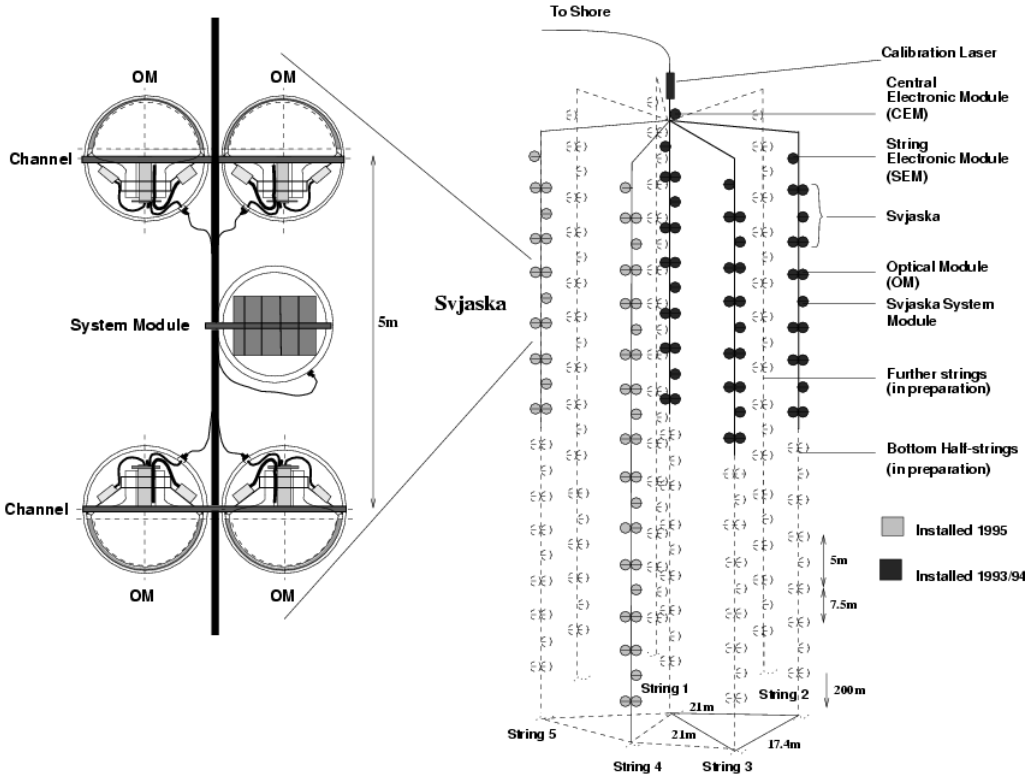

Figure 2.5: Schematic view of the Baikal Telescope NT-200. On the left we show an expanded view of 2 pairs of optical modules (*svjaska*) with the svjaska electronics module, which houses parts of the read-out and control electronics.

with an about 20% seasonal variation. The effective[6] scattering length is $300\ m$. Light emitting biological activity is present in the water and contributes to the noise in the PMTs. Strong variations in this activity is correlated with seasonal changes and with outflow of nutrients due to heavy rains. The PMT noise rate may then reach a few hundred kHz. Still, the increased noise rate does not affect the trigger rate of the array in a noticeable way. Correlating the noise data with other measurements will be also useful for limnological studies[7] [4].

Since 1998 a calibration of the angular resolution of the detector has been

[6]The scattering length is about $15 \div 30\ m$, but scattering is strongly forward peaked: $< \cos\theta >$ is $0.85 \div 0.95$.

[7]Limnology is the scientific study of physical, chemical and biological characteristic of fresh water.

performed thanks to a (Čerenkov and scintillator) array for EAS measurements on the ice cover present in the cold season above the Baikal telescope. Results for energies above $200\ TeV$ show that the angular resolution is better than 5^o. The same scintillator array has been used as trigger of an array of hydrophones, to search for acoustic signals (see last section of this chapter) generated by very high energy ν-induced showers: with a threshold at PeV energies, 2-3 events per hour have been observed.

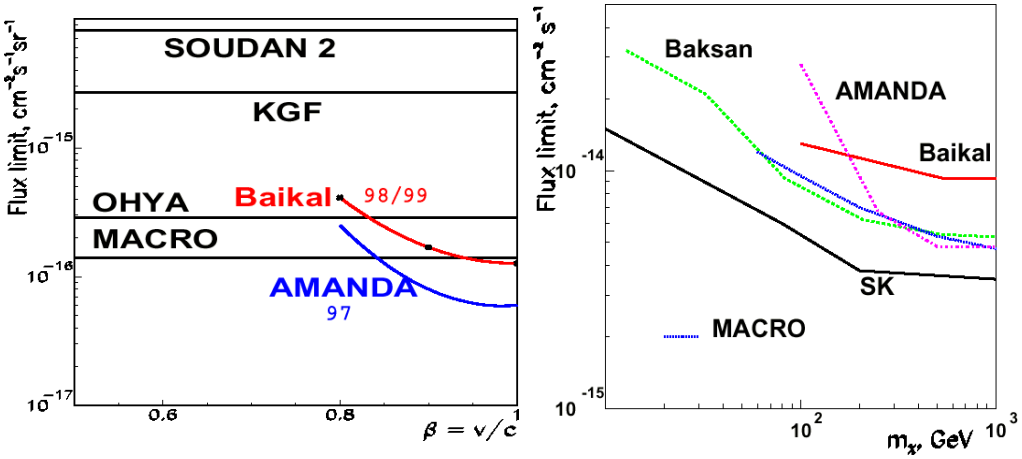

Figure 2.6: *Left:* Upper limits on the flux of fast monopoles obtained in different experiments. *Right:* Upper limits on the excess muon flux from the center of the Earth as a function of the WIMP mass.

Summed over 840 days effective lifetime, $4.6 \cdot 10^8$ muon events have been collected with NT-36, -72, -96, -144. The collaboration has also analyzed the NT-200 data up to 1999, a total of 572 additional live days. Figure 2.6 shows the upper limits derived for the flux of muons from the center of Earth (related to WIMP annihilation) and the flux of relativistic magnetic monopoles [6]. The limits on the diffuse neutrino flux are shown in figure 2.10.

Figure 2.7 shows the celestial distribution of events recorded in 1999 (268 days of effective lifetime): this data set yields 84 reconstructed events with upward tracks, to be compared with the MC result of 80.5 muon tracks expected from atmospheric neutrinos.

The NT-200 effective area is between 1000 and $5000\ m^2$, depending on the energy, and it investigates atmospheric neutrino spectra above $10\ GeV$ detecting about 1 atmospheric neutrino per day.

An upgrade of NT-200, called NT-200+ [7], is now uderway. This consists of

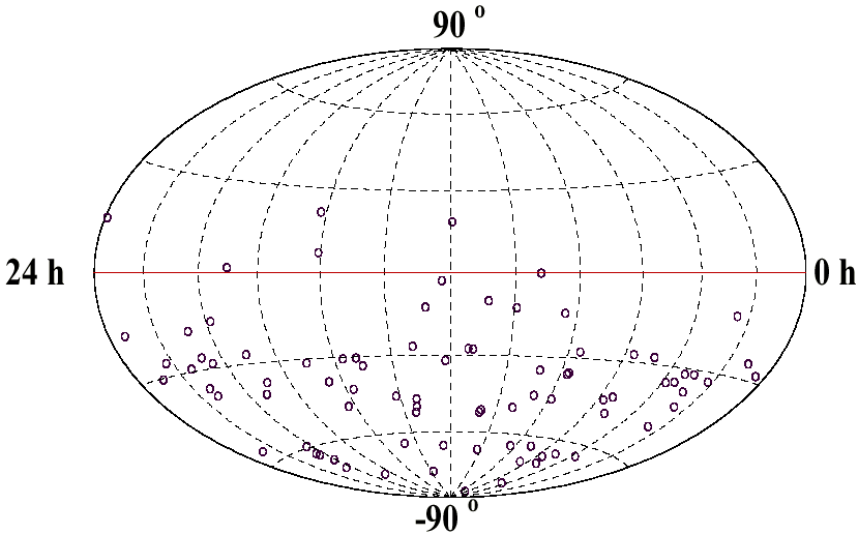

Figure 2.7: Baikal skyplot from data taken in 1999 with NT-200. [6]

three sparsely[8] instrumented outer strings, deployed $140\ m$ below the present detector, at the edges of an equilateral triangle centered on NT-200, having a $150\ m$ long side. The basic principle will be the search for cascades produced in a large volume below NT-200. Most of the expected events would be produced by neutrinos in the energy range $10^2 \div 10^5\ TeV$, with a mean energy around $1\ PeV$. Two of the outer strings have already been installed. The construction will be completed in 2005. For higher neutrino energies, such a configuration could be used as a basic subarray of a Gigaton Volume Detector (GVD), which could be achieved with about 1300 OMs arranged in 91 strings. This would have a muon threshold between $10 \div 100\ TeV$ and an effective volume between $0.5 \div 1.0\ km^3$ for $100\ TeV$ muon cascades.

2.4 AMANDA

The Antarctic Muon And Neutrino Detector Array (AMANDA) is installed in the $2.8\,km$-thick glacier at the geographic South Pole. Installation of the detector

[8] 6 pairs of OMs on each string. The pairs are arranged in three groups, with a vertical separation of $6\ m$ between the two pairs of each group of and a vertical separation between groups of $70\ m$.

takes place only in the Antarctic summer when the Amundsen Scott Polar Station is open to a larger population of scientists. During the winter season a crew of less than 30 persons takes care of the running of the various experiments, including AMANDA. The telescope effective area is of the order of $10^4\ m^2$ for TeV neutrinos. It has a threshold near $50\ GeV$ and a pointing accuracy of $2 \div 2.5^o$ per muon track.

Once installed in the ice, the detector remains geometrically stable and the strings deviate from the vertical by less than $1\ m$ over $2.4\ km$. Holes have been drilled into the glacier by using hot water down to $2400\ m$. The cost and the limited supply of fuel at the South Pole limit the maximum hole diameter to $60\ cm$ and the drilling speed to $1\ cm/s$. The detector modules are connected along electrical and optical cables and lowered into the hole. The refreezing of water in the hole takes about one week.

As the stable temperature is low, around -30^o, the internal noise in the PMTs is small. The absence of radioactive substances and of bioluminescent living organisms results in a very low noise rate, about $300\ Hz$ for the best part of the array[9]. The low noise level facilitates triggering and data acquisition, allowing detection even at low energies.

Figure 2.8 shows the AMANDA telescope setup after the deployments that took place in the year 2000.

The first installation to take place in 1993/1994, was that of AMANDA-A. Eighty optical modules were installed at dephts between 800 and $1000\ m$. At this depth the ice has a very long absorption length, greater than $200\ m$, but remaining air bubbles were found to make the scattering length short, $20 \div 40\ cm$. During 1994-1996 a deeper detector[10], having ten strings and reaching a total of 302 optical modules, was installed between 1500 and $2000\ m$. The diameter of this array, AMANDA B10, is $120\ m$.
The installation of 9 more strings in an outer ring at a diameter of $200\ m$ was completed in the austral summer 1999/2000. This final array, AMANDA-II, consists then of 677 8" Hamamatsu R5912-02 PMTs arranged in strings of beads on 19 electrical cables.

The optical properties of the ice have been measured for several wavelengths in the range from 313 to $540\ nm$. The absorption length is found to be $90 \div 220\ m$

[9] After a change of the pressure-housing supplier (from Billings Inc. to Benthos Inc. Company) the modules have higher noise, up to $1.5\ kHz$. The increase is due to potassium, which had been added to the glass.

[10] Below $1400\ m$, where ice is almost bubble free except for bubbles produced in the drilling procedure. [8]

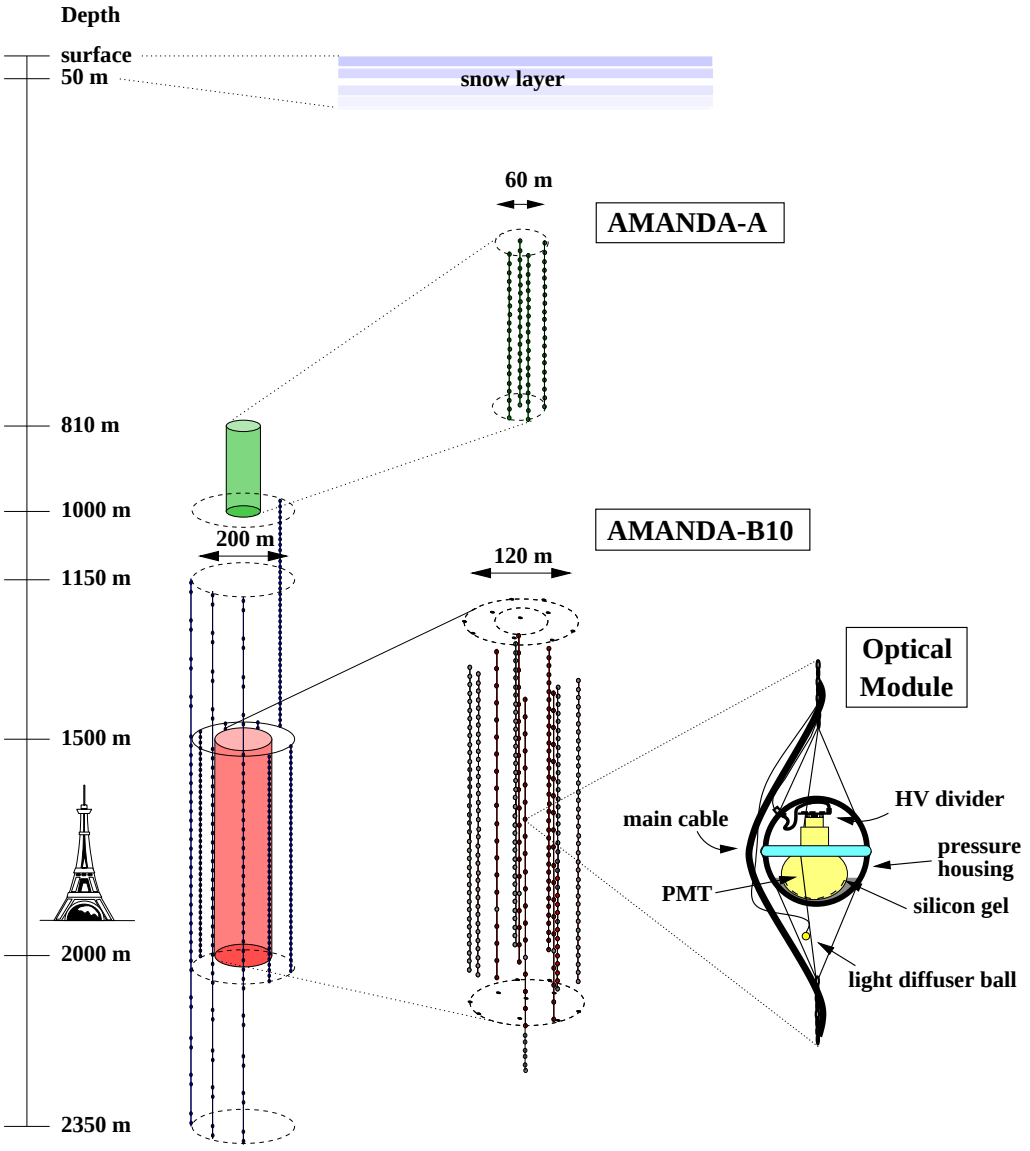

Figure 2.8: The AMANDA II detector after the 1999/2000 deployment (left) and zoomed views of the earlier detectors (center) and of an optical module (right).

for light with wavelengths around $400\ nm$. The effective scattering length in the ice is not more than $25\ m$ for $523\ nm$ light at the depth of the final detector[11]. The collaboration anyway does manage to reconstruct tracks with reasonable accuracy by demanding at least 6 PMTs with very large pulse heights, but the sensitive area is then reduced by a factor 20.

The SPASE air shower array and the GASP atmospheric Čerenkov telescope at the surface of the ice measure air showers from high-energy ($E > 100\ TeV$) cosmic rays [8]. AMANDA events in coincidence with detection by experiments at the surface can be used for calibration and for checking the performance of the AMANDA array.

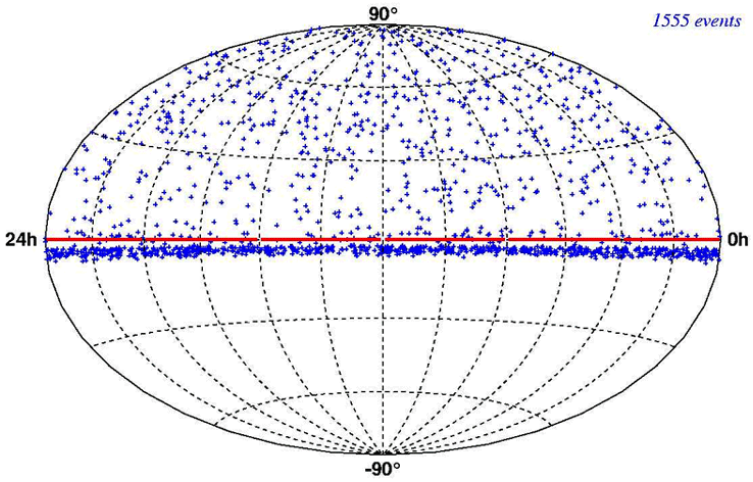

Figure 2.9: Skyplot in equatorial coordinates of events recorded by AMANDA-II in year 2000. The thick band of events below the horizon shows the onset of the down-going cosmic ray muon background contamination. [9]

One of the major goals of AMANDA-II is to search for astrophysical point sources of high energy neutrinos. All the data taken in 1997 (AMANDA B10) and in 2000 (AMANDA II) have been analyzed. As shown in figure 2.9, no statistically significant excess over the atmospheric background is seen in the search for point sources. The most significant excess, observed at about 68^o Dec., $21.1h$ R.A., is 8 events observed on an expected background of 2.1. Simulations predict a probability of 51% to observe such an excess as a random upward fluctuation

[11]The depth-dependent variations are correlated to known differences in the dust concentration and depend on the conditions when the ice was formed, around $5 \cdot 10^4\ yr$ ago.

of the background. AMANDA-II has operated continuously since the year 2000: the additional data which are now being analyzed should improve the sensitivity of the results.

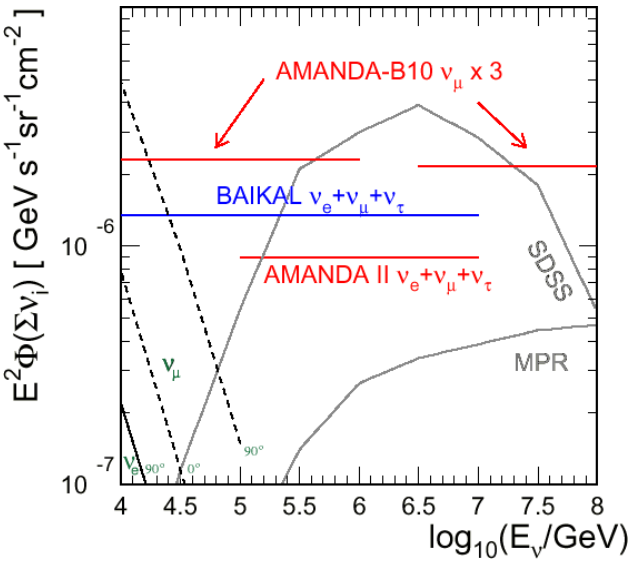

Figure 2.10: The limits on the diffuse neutrino flux, summed over the three flavors, shown for AMANDA-II and Baikal. A multiplicative factor is applied as indicated to permit comparison of limits derived for ν_μ in AMANDA B-10. The predicted atmospheric ν_μ, ν_e fluxes are also shown. [10]

Using the cascade events the collaboration also derived constraints on the diffuse flux of extraterrestrial neutrinos, shown in figure 2.10. Demonstrating ν-induced cascade sensitivity is an important step for neutrino astronomy because the cascade channel probes all neutrino flavours. Compared to muons, cascades provide more accurate energy measurement and better separation from background, but they suffer from far worse angular resolution and reduced effective volume.

The continuation of the experiment towards the km^3 scale, the IceCube project, has been already approved and partially funded. It will be composed of 80 strings, each one kilometer long (depht $1400 \div 2400\ m$) with 60 PMTs each. The 4800 PMTs will be a modified version of the AMANDA ones, the 10" Hamamatsu R-7081 PMTs. The detector volume will be one cubic kilometer and its instrumented mass will be one Gigaton. The factor which determines the construction time is

the speed of boring holes in the ice: a six year construction time is expected, and work will start the next Austral summer.

IceCube has been designed to detect neutrinos of all flavours from $10^7\ eV$ (supernova neutrinos)[12] to the highest energy of $10^{20}\ eV$. Muons can be observed from about $10^{11}\ eV$, cascades (generated by $\nu_e,\ \overline{\nu}_e\ \nu_\tau$ and $\overline{\nu}_\tau$) can be observed and reconstructed at energies above $10^{13}\ eV$, tau events can be identified above energies of about one PeV.

A surface airshower detector consisting of 160 stations over $1\ km^2$ augments the deep ice component by providing a tool for calibration, background rejection and air shower physics.

2.5 Future projects: KM3-net

The obvious evolution for Neutrino Telescopes is the kilometer-cube size, in order to become sensitive to very far or rare sources.

As a complementary project to the already approved ICECUBE experiment at the South Pole, the European astroparticle physics community's aim is to build a very large volume neutrino telescope in the northern hemisphere. Co-ordination between the various groups already existing, ANTARES, NEMO and NESTOR, is needed to attract the necessary funding and manpower for this large project. To this purpose, an application for a design study has been submitted to the European Union in the framework of the 6^{th} *EU's Framework Programme for Research and Technological Development* (FP6). A decision on funding for this project is forthcoming.

In chapter 5 we shall discuss attempts, going on within the KM3-net collaboration, towards the design of a km^3 detector in the Mediterranean.

In the following sections the present situation and future planning of demonstrator experiments in the Mediterranean, NESTOR and NEMO, will be briefly described. The ANTARES experiment will be described in detail in the following chapter.

[12] By using only the dense AMANDA array.

2.5.1 NESTOR

The NESTOR (Neutrino Extended Submarine Telescope with Oceanographic Research) collaboration has located a $8 \times 9\ km^2$ horizontal plateau at a depth of $4000\ m$ and only $14\ km$ off the coast near Pylos, Greece. The conditions are very favorable for the operation of an optical detector system: the depth is constant to within $50\ m$ over the entire plateau and the connection with close shore requires an electro-optical cable of modest length, the water transmission length in the blue part of the spectrum is about $55\ m$ [12], and underwater currents are below $10\ cm/s$. A total of 144 large 15" Hamamatus R2018-03 phototubes will be employed. The optical background due to radioactive decays was measured to be $75\ kHz$ per optical module at the 0.25 p.e. level. Bioluminescence bursts of duration $3 \div 5\ s$, with frequency of 1% of the experiment live time were detected.

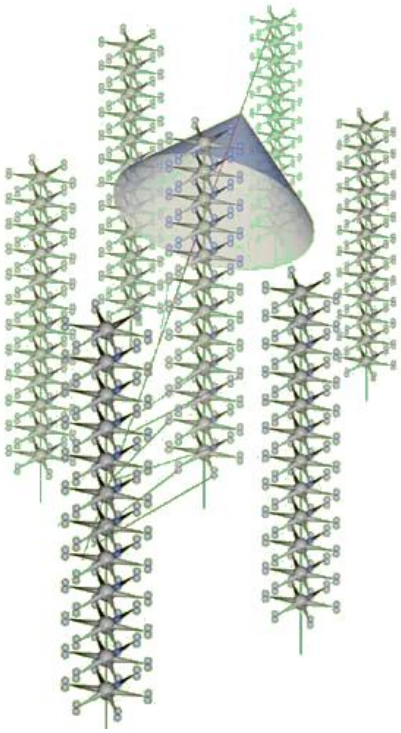

Figure 2.11: Layout of the final NESTOR telescope.

A modular, and hence expandible, design has been chosen for the detector. The basic detector element is a star-like hexagon made out of titanium with a $32\ m$ diagonal. A central casing supports a spherical titanium pressure housing which contains the readout and data acquisition electronics, power converters, monitoring, control and data transmission equipment. Attached to the central casing are six titanium arms. At the end of each arm a pair of PMTs is mounted, with one PMT looking up and the other down, making a total of 12 PMTs per floor. Using this configuration gives 4π coverage, enhances the discrimination between upward and downward going particles and improves the background rejection. By stacking 12 of these hexagonal floors along the vertical, with a distance between floors of $20 \div 30\ m$, a tower is created. As soon as the first tower is deployed, the collaboration plans to deploy the 3 strings they have been given by the DUMAND collaboration at a distance of $80\ m$ around the tower. The effective area of the combination reaches $10^5\ m^2$ for PeV neutrinos [13].

The first floor has been already successfully deployed at the end of March 2003 [14], and 745 atmospheric muons have been recorded. Figure 2.12 shows the zenith angle distribution of the observed events, compared to a MC predicition.

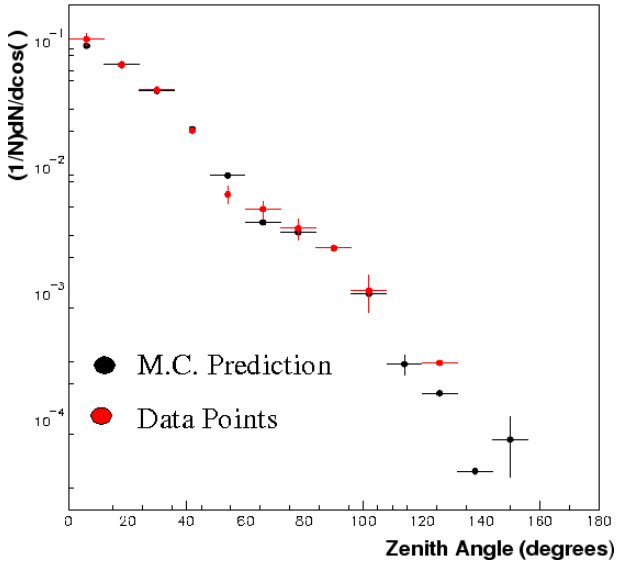

Figure 2.12: Zenith angle distribution of detected atmospheric muons, compared with MC prediction.

Additional funds could then allow to build six more towers, in order to deploy them in a hexagonal fashion around the first tower (figure 2.11) and at a distance of $150\ m$ from it. This array would have, for PeV neutrinos, a sensitive area three times larger than the previous configuration. The detection threshold is forseen to be $10\ Tev$ for muon tracks, but events contained within one tower can be reconstructed down to $4\ GeV$.

In order to be independent of cable-laying ships and to accelerate progress, the NESTOR Institute has built a highly specialized deployment platform, the DELTA-BERENIKE (see figure 2.13): it has a central well, is a ballasted, self-propelled equilateral triangular platform ($51\ m$ side), which can keep its position in the high seas to a few meters using dynamical control GPS systems. All connections would be made dry in air and no bathyscaphs would be required to make connections under water.

Figure 2.13: The DELTA-BERENIKE platform

2.5.2 NEMO

NEMO is a research and development project directed towards the construction of a submarine laboratory for high energy neutrino detection and interdisciplinary activities, using a 1 kilometer cube detection system. The present activities [16] include site search and characterisation, Monte Carlo simulation studies of the detector capabilities, and construction of a $0.1\ km^2$ demonstrator.

Since 1998, the NEMO collaboration has performed more than 20 sea campaigns on three possible sites, to establish a permanent site for the full study involving a cubic kilometer neutrino telescope. A site in the Ionian Sea, $70\ km$ SE of Capo Passero (Sicily), is currently the favoured option. The favoured site, has a water depth of 3350 metres and fulfills all the needs regarding optical transparency (λ_{abs} is $67\ m$ at $420\ nm$, close to the value of optically pure water, and the overall attenuation[13] is characterized by a $\lambda_{att} \approx 33\ m$ [17, 18]), low biological activity and good oceanographical properties (like sedimentation, seabed geology and deep sea currents).

Recently, a common effort has been undertaken by NEMO together with the ANTARES collaboration, aiming at the design of a km^3 telescope. The simulations have been based on the ANTARES software package [56, 57]. Several geo-

[13]The used AC9 transmissometer does not allow to measure directly the scattering parameters.

metrical configurations, instrumented with different numbers of large area PMTs have been tested. The simulations assumed a detector instrumented with 6000 PMTs, arranged in a lattice of 400 square towers ($800\ m$ height) with horizontal (string) and vertical (storey) distance between downlooking sensors equal to $60\ m$. Such a detector may achieve an effective area greater than $2\ km^2$ for $E > 100\ TeV$ muons, and an angular resolution below 0.2^o at the same energies.

After a long phase of R&D, the collaboration is installing a deep sea test site facility.

This project, called NEMO Phase 1, will be a submarine laboratory for prototyping mechanical structures and data transmission systems. It will be composed by a network of Junction Boxes (a main one and two secondary) and two NEMO towers. A tower is a three-dimensional structure composed by a sequence of storeys that host the instrumentation, interlinked by a system of cables, anchored on the seabed and kept vertical by an appropriate buoyancy on the top. The final features of the tower (number of storeys, number of optical modules per storey, distance between the storeys) can be optimized following the results of numerical simulations. However, the modular structure of the tower will allow to adjust these parameters to the experimental needs. In the preliminary design an 18-storey tower is considered. Each storey consist of $20\ m$ long pipe housing 2 OMs at each end (4 OMs per storey). The vertical separation between storeys is fixed at $40\ m$, giving a total active height of $680\ m$. An additional spacing of $150\ m$ is added at the base of the tower, to allow for a sufficient water volume below the detector. In its working position each storey will be rotated by 90^o, with respect to the upper and lower adjacent ones, around the vertical axis of the tower.

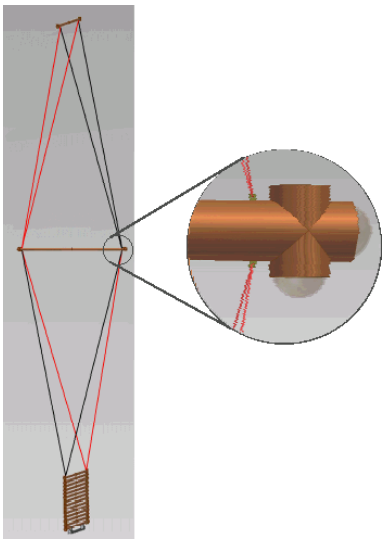

Figure 2.14: The NEMO tower, partly packed with two unfurled storey. *In the circle:* close up view of one end of the tube with the optical module assembly.

In the meantime, the collaboration is developing a light detector prototype, based on an improved (multianode) version of the BAIKAL hybrid PMT coupled to a matrix of Winston cones [69]. Though the presently available photomultipliers generally match energy and time resolution requirements, the possibility to

recognize the Čerenkov light direction could drastically reduce the background primarily generated by the ^{40}K decay, allowing to improve the detection performances at lower neutrino energies. Similar goals are foreseen for the light detector development described in chapter 5.

2.6 Other detection techniques

The flux of neutrinos with energies higher than $10^6\ GeV$ is so low that even cubic kilometer size detectors are too small to detect point sources. For cost reasons the water Čerenkov technique is not affordable if one wants to instrument the required tens of cubic kilometres. There is a lot of activity in developing the necessary alternative experimental techniques.

Significant efforts are going on towards the detection of acoustic pulses produced in water by local heating from neutrino-induced showers of almost joule energies. The (electromagnetic or hadronic) cascade of a neutrino interaction at those energies is confined roughly in a cylinder with radius of a few mm and length $5 \div 10\ m$ [1]. The resulting local energy deposition heats the water causing an adiabatic expansion and a bipolar pressure pulse which can be detected up to a few kilometres away. The acoustic signal is emitted preferentially in a disk perpendicular to the cascade axis in a rather narrow solid angle.

The hardware and techniques for ocean acoustics are not expensive and have already been developed for military research. The disadvantage is that the ocean backgrounds are not well understood and the signal is very small, thus pushing the detectable neutrino threshold to ultra high energies. However, there is some activity going on [14].

An alternative under test consists in the detection of coherent Čerenkov radiation produced in the radio and microwave regions by a charge asymmetry in electromagnetic cascades at EeV energies [1]. The detection requires a medium transparent to radio waves like Antarctic ice[15], natural salt domes[16] or the upper $10\ m$ of the Moon's regolith[17].

[14] Baikal and AMANDA arrays, SADCO (Greece) and AUTEC (US) are few examples.

[15] ANITA propose the use of a ballon borne antenna; RICE is an already working antennae array buried close to the AMANDA strings.

[16] SALSA, still at the conceptual stage, aims to reach a sensitive mass of several hundreds of cubic kilometres by using a radio array.

[17] GLUE utilizes the NASA Goldstone Deep Space telescope: its effective target volume is $10^5\ km^3$, but the observation time is very limited (300 hours in the next 3 years).

Lastly, people are studying how to detect neutrinos travelling in a horizontal direction with very large extensive air shower arrays like AUGER or with proposed spaceborne instruments EUSO/OWL. Neutrinos are in fact the only particles that can survive the $30 \div 40$ interaction lengths which constitute the atmosphere along the horizon, hence an extensive air shower coming from that direction may only be due to them. Space borne experiments also hope to detect upward coming tau neutrinos, which have been degraded in energy by CC-interacting in the Earth and being regenerated again (through τ decay) until they interact in the atmosphere.

Chapter 3

The ANTARES experiment

The ANTARES experiment (Astronomy with a Neutrino Telescope and Abyss environmental RESearch) aims at the construction in the Mediterranean Sea of an array of about 1000 optical modules to form a high-energy (in the $TeV \div PeV$ range) neutrino detector. In figure 3.2 the energy dependence of the effective area (see definition in chapter 2) for muon and neutrino detection is shown.

The experiment is somehow complementary to AMANDA. As can be seen in figure 3.1, the ANTARES detector covers the sky hemisphere opposite to the one visible from the South Pole (the total field of view is $3.5\pi\ sr$, of which $0.6\pi\ sr$ overlap with AMANDA) and is therefore able to look at the galactic center 67% of the time.

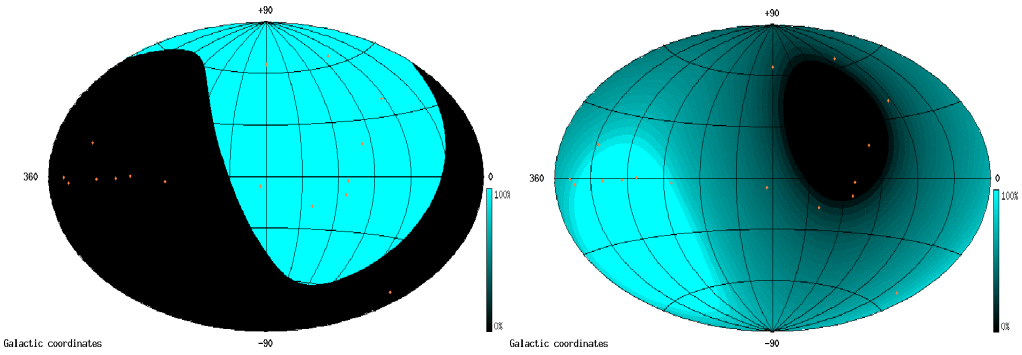

Figure 3.1: Comparison between the field of view of the AMANDA (left) and ANTARES (right) experiment.

Furthermore, sea water is characterized by a longer scattering length than ice.

Hence a better angular resolution [1] can be achieved, allowing optimization for specific physics targets and counterbalancing the drawback of the optical background (higher in sea than in ice). ANTARES will be characterized by a maximum angular resolution better than 0.2^o and a maximum energy resolution of about $10\ GeV$ at $100\ PeV$. The energy dependence of these parameters is displayed in figure 3.3.

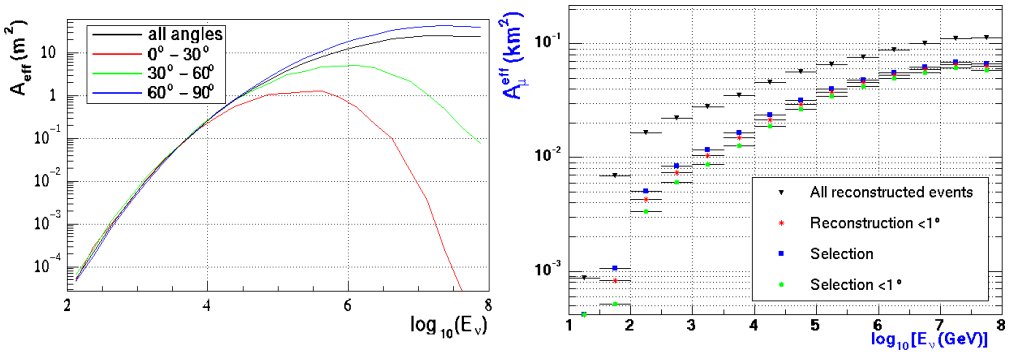

Figure 3.2: Effective area for neutrinos entering the Earth (left) and for ν-induced muons at the detector (right) as function of energy.

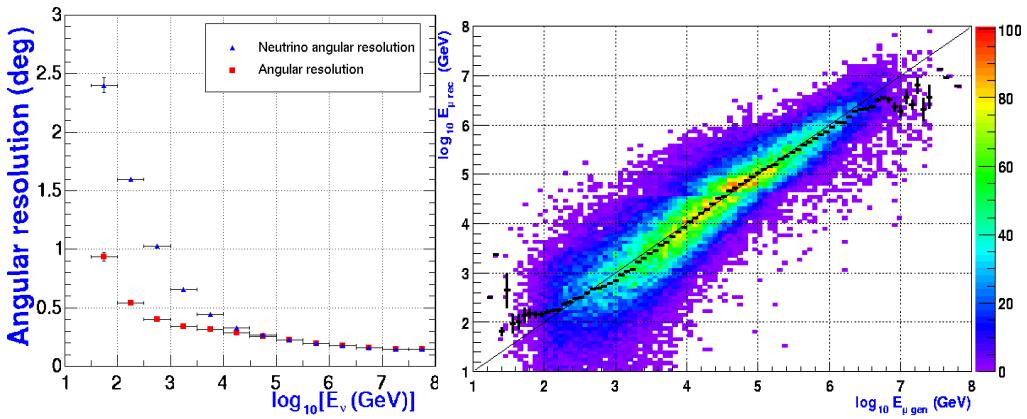

Figure 3.3: *Left:* Angular resolution for neutrinos and for muons as functions of energy. *Right:* Muon reconstructed vs generated energy for Monte Carlo events. Black crosses superimposed are a profile of the two-dimensional scatter plot.

[1] See definition in chapter 2.

The ANTARES telescope would extend its scientific programme within particle physics and astrophysics.

The particle physics area, mainly concerning neutrino oscillations, has partly lost the importance it had when the ANTARES design started, in 1996, after the successful efforts of SNO [63], Kamland [64], SK and K2K [65] in validating the theory of neutrino oscillations and constraining the mixing angles and squared mass differences. Moreover, the energies involved in the study of atmospheric neutrino oscillations don't well match the detection capabilities of ANTARES.

The detection of high energy neutrinos with unprecedented angular resolution is the most important aim of the ANTARES experiment mainly because of its astronomical implications. The principal mechanism for generating high energy neutrinos is through decay cascades originating in the interaction of high energy protons with matter or radiation. Hence the astrophysical sources of high energy neutrinos may also be the sources of the highest energy cosmic rays. Neutrino astronomy has already been discussed in the previous chapter.

The ANTARES sensitivity to muon fluxes expected after one year of data taking is shown in figure 3.4, compared with upper limits already set by measurements performed by other experiments. The estimate of the expected fluxes from sources already known from gamma astronomy is very model dependent and it is not reported here.

Another ANTARES goal is a search, through the detection of neutrinos, for supersymmetric dark matter relics in a region of the model parameter space which is interesting for cosmology and particle physics. Neutrino telescopes are not directly sensitive to WIMPs. However such particles could have been gravitationally captured in the cores of the Sun and the Earth or in the centre of the Galaxy. Their resulting high density would lead to annihilation reactions, which would then yield high-energy neutrinos through the decays of the gauge bosons and heavy particles produced. Compared to ongoing direct detection experiments, neutrino telescopes are generally more suitable for large WIMP masses, although resonances in the Earth's capture cross-section are believed to strongly enhance the signal at certain lower masses, particularly around $56\ GeV$.

The two main noise components for the ANTARES experiment are an optical and a physical background. The first one is due to light sources different from the Čerenkov light from cosmic particles, like bioluminescence or Čerenkov light from radioactive decay products.

The behaviour of this background places constraints on the trigger logic and the electronics as well as on the mechanical layout of the optical modules. The measured rates are in fact very high, such as to constitute a hazard to the very

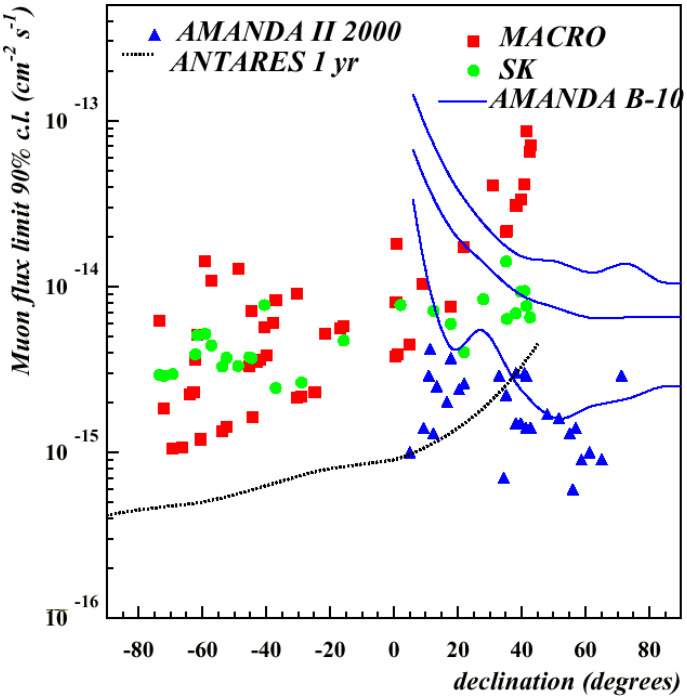

Figure 3.4: 90% confidence level upper limits on μ fluxes induced by neutrinos with E^{-2} spectrum as function of source declination for SK, MACRO, AMANDA-B10 and AMANDA II. ANTARES sensitivity after $1\ yr$ is also shown. It has not been possible to apply a correction due to different μ average energy thresholds ($1.5\ GeV$ in MACRO, $3\ GeV$ in SK, $50\ GeV$ in AMANDA and ANTARES). Nevertheless, the maximum of the response curves of all detectors is at $E_\mu \approx 10\ TeV$, hence events contributing below $50\ GeV$ should not make a large correction to these limits. [19]

functionality of the photomultiplier tubes (PMT) or to increase by large amounts data to be transferred to shore. A contribution of about $30\ kHz$ comes from radioactive decays, in particular of the ^{40}K isotope. Bioluminescence present in sea water increases up to $50 \div 100\ kHz$ the base noise rate and it also causes intense bursts up to tens of MHz. Assuming the PMT nominal gain of 10^8, the charge per single photoelectron can be estimated as $\approx 10\ pC$: this means that the maximum anode current tolerated by the PMT ($0.1\ mA$) is reached already at a rate of $10\ MHz$.

The optical background is the main subject of this thesis and will be described in detail in chapter 4.

Besides ^{40}K and bioluminescence, the main light sources in deep sea originate from atmospheric muon Čerenkov light emission (about $300\ \gamma/cm$ in the interesting wavelength range, between $300 \div 600\ nm$). Multiple downgoing muon events, which could constitute a background when misreconstructed as upgoing events, is suppressed by the detection depth. However, the vertical downgoing muon flux at a depth of $2400\ m$ ($10 \div 30\ Hz$ depending on threshold energy and solid angle definition) is still about 10^6 times larger than the vertical upgoing muon flux from atmospheric neutrinos (see again figure 2.2). This is a formidable challenge for the detector. This second background component cannot be reduced with an appropriate on-line trigger, but it will need an ad-hoc filter based on the physical characteristics of the events.

3.1 Architecture

The detector consists of an array of 900 PMTs arranged in 12 vertical structures, called *strings*, anchored to the sea bed, spread over an area of about $0.05\ km^2$ [23] and characterized by an active height of about $350\ m$. Figure 3.5 shows a schematic view of part of the detector array indicating its main components.

In conjunction with the detector string is foreseen the deployment of a dedicated line for monitoring environmental parameters (see section 3.1.2) and a facility, the General Purpose Experimental Platform (GPEP), for oceanographic research which will be connected to the shore via the same junction box and electro-optical cable as the neutrino telescope lines.

The basic sensitive unit of the detector is the optical module (OM), consisting of a PMT, a set of sensors for calibration purposes, and the associated electronics. The electronics includes a custom-built digital electronic circuit for PMT data acquisition, the high-voltage power supply for the PMTs and the network nodes for data transmission and slow control. The optical modules are housed in pressure-resistant glass spheres and are grouped together in clusters of three. Each of the 25 clusters of a single string is controlled by a separate electronic crate called *local control module* (LCM). All the LCMs in a string are interconnected via an electro-mechanical cable. This composite segment (OM cluster + LCM) is called *storey*, and a *hydrophone* and (eventually[2]) an *optical beacons* (OB) are also placed in it. The three OMs of a storey, the OBs, the hydrophone and the associated LCM are held by the optical module frame (OMF). The spacing between storeys is fixed to

[2]Since one OB is able to illuminate 8-10 storeys of each neighbour string, each detector line is equipped with 4 OBs only.

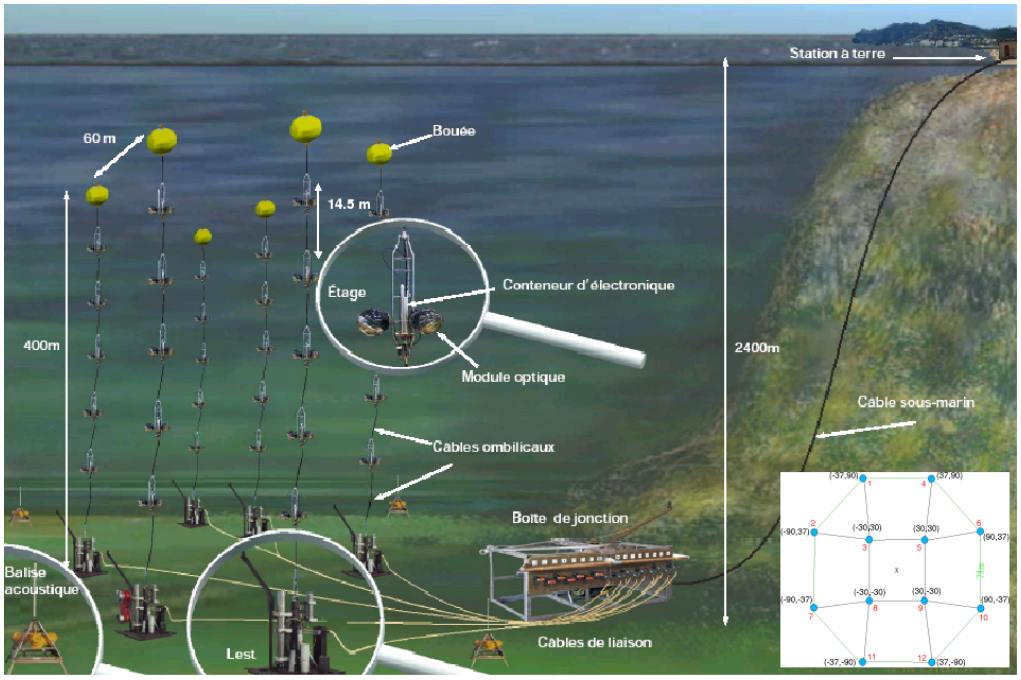

Figure 3.5: An artist view of the ANTARES detector. In the white square on the right, the horizontal layout of the 12 string is shown.

$14.5\ m$ and about $100\ m$ divide the last storey from the sea bed, hence the total height of each line is about $450\ m$. As shown in the bottom-right corner of figure 3.5 the strings are arranged in an octagon with a minimum horizontal spacing of $60\ m$.

The optical modules in a storey are rigidly arranged in such a way that the axes of the PMTs point downwards, at an angle of 45^o to the horizontal and with a horizontal angle of 120^o between them. The angular acceptance of the optical modules is broader than $\pm 70^o$ ($1.3\pi\ sr$) with respect to the PMT axis. This means that the proposed arrangement detects light in the lower hemisphere with high efficiency, and also has some acceptance for muon directions above the horizontal. Moreover, in the hemisphere below the sea horizon, there is an overlap in angular acceptance between modules, allowing the possibility of an event trigger based on coincidences between nearby modules.

The relative positions and orientation of all storeys in the detector are given in real time by two independent positioning system.

A string, in fact, does not provides a rigid support for the optical modules,

and event reconstruction has to take into account their real position at each given moment. The precision of this spatial positioning should be better than the time uncertainty in light detection by the PMT ($1\ ns$ is equivalent to $22\ cm$ of light travel path in water). The relative positioning of every OM of the detector is hence determined to an accuracy of $10 \div 20\ cm$ (depending on the OM location and the current speed).
The first part of the positioning system is based on a set of tiltmeters and compasses which measure local tilt angles and orientation of each cluster. The reconstruction of the line shape, as distorted by the water current flow, is obtained from a fit of measurements taken at different points along the lines: a maximum error of $1\ m$ on the reconstructed shape is estimated, assuming a precision of 0.05^o in tilt and of 0.3^o in direction.
The second system, based on acoustic triangulation, is more precise but requires more complex and expensive electronics. The *trasponder*[3] placed at BSS of each string send an acoustic signal to a minimum of three transponders fixed to the sea bed, each of whom replies with its characteristic frequency which will detected by the hydrophones placed on each storey. A global fit of the measured acoustic paths gives the precise three-dimensional position of the rangemeters, provided that the positions of the transponders and the sound velocity in water are known[4]. The systems are complementary: a few points of the line can be measured acoustically and other points are obtained by line shape fitting.

In addition to the relative positioning of the OMs, the reconstruction of the muon tracks in the ANTARES detector depends on the relative timing of each phototube signal with respect to the others. A timing calibration with an accuracy of 0.5 ns must be achieved in order to avoid degradation of the $1\ ns$ precision of the Cerenkov light arrival time measurements given by the photomultiplier.

A string is instrumented with several electronics containers. Each of these containers constitutes a node of the data transmission network, receiving and transmitting data and slow-control commands. At every storey, a local control module (LCM) is located, and at the base of each string there is a string control module (SCM). Special containers house acoustics and calibration equipments. The control modules support front-end electronics readout, sensor readout, slow-control parameters adjustment and trigger generation. Electronic containers also provide the distribution of power, master clock and reset signals to the front-end electron-

[3]Acoustic emitter-receiver.

[4]It is continuously monitored by a sound velocimeter with a precision of $5\ cm/s$ and some Conducivity Temperature Depth (CTD) devices record the variations of water temperature and salinity on which the speed of sound depends.

ics.

The individual SCMs are linked to a common *junction box* (JB) by electro-optical cables which are connected using a manned submarine. A standard deep sea telecommunication cable links the junction box with the shore station where the data are filtered and recorded.

The trigger logic off shore has been designed to be as simple and flexible as possible. Its main goal is to reduce the optical background contamination of physical events, without introducing a bias on event reconstruction. In the original intentions[5]: following a second-level trigger the full detector would have been read out.
The first-level trigger (L1) requires a coincidence between any two OMs in a single storey, which is highly likely in case of Čerenkov emission from an energetic muon, thanks to the typical wide emission cone in water and to the overlap between PMTs angular acceptance in the same cluster.
A second-level trigger (L2) is based on combinations of first-level triggers. A more refined third-level trigger, imposing tighter time coincidences over larger numbers of optical modules, must be implemented using a farm of processors on shore: the readout rate is expected to be hundreds of kHz, but the corresponding data recording rate should be lower than 100 events per second.

The following sections of this chapter describe the various components of the detector in more detail.

3.1.1 The Detector Strings

Each of the 12 strings is mantained vertically by a buoy on the top and anchored on the sea bottom. Between the buoy and the anchor, the active part of the string comprises a series of elementary detector segments. These segments are standardised and can thus be mass-produced and (if necessary) interchanged. String components are designed to resist corrosion by salt water and high pressure, to be watertight and to minimize light reflection. The planned minumum lifetime for each component is 10 years.

The configuration of the principal elements of each string is illustrated in figure 3.6.

The *bottom string socket* (BSS) anchors the string to the sea bed, facilitates the electrical connection of the string to the network and permits the release and

[5]Recently it has been suggested to avoid in the initial phase of the experiment the use of any off-shore trigger.

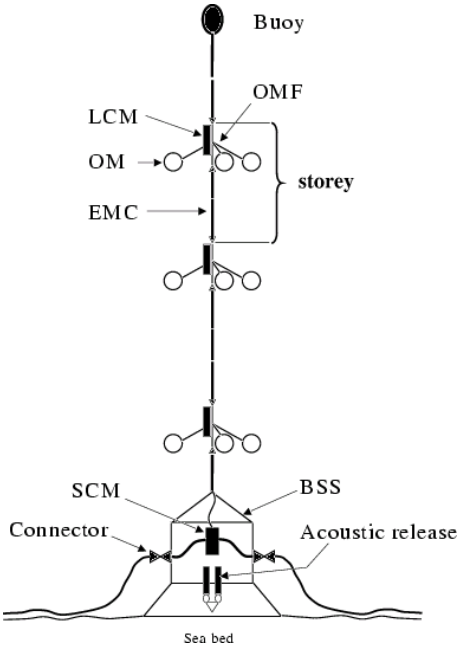

Figure 3.6: Schematic view of a detector string. Only 3 of the 25 storeys are drawn here. Acronyms are defined in the text and itemized in appendix A.

subsequent retrieval of the string itself. Connection of the string to the network is performed by a submarine. In order to allow precise and simple string installation, its construction has been optimized for handling on the deployment ship, resistance to shock, stability during descent. The BSS is instrumented for acoustic positioning.

The *electro-mechanical cable* (EMC) provides mechanical support for the string and enables the electrical interconnection of the detector string elements. It is capable of supporting tensile, torsion and bending stresses maintaining the string's stability, and is flexible enough to facilitate string handling, deployment and retrieval. Electrical cables and optical fibres run through the EMC and enable power distribution and transmission of signals between two consecutive electronic containers (LCM or SCM).

A schematic view of the ANTARES storey and its main components is shown in figure 3.7.

The OMF is a titanium structure which supports the various elements placed within it, namely the optical modules, the LCM container a hydrophone[6] and

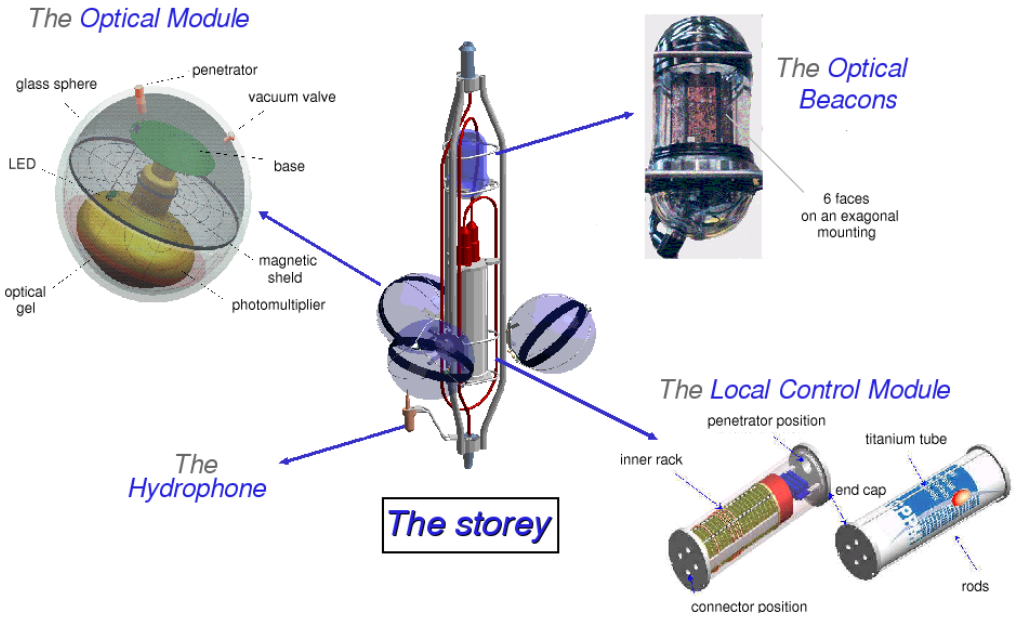

Figure 3.7: The base elements of a storey.

possibly an optical beacon[7] and supports the major traction forces that work on the string during deployment and recovery without transmitting them to the active elements.

Out of each set of five consecutive LCMs in every string, one is a *master LCM* (MLCM) with a predominant role for trigger logic and clock distribution. The MLCMs act as mediators between the SCM and the other four slave LCMs. Each group of five LCMs constitutes a *sector*: each string consists of five sectors. The Pisa group contributes to the ANTARES experiment with the integration and testing of a large part of the slave LCMs which will be necessary for the $0.1\ km^2$ phase.

The top of the string consists of a buoy whose dimension and geometry are optimised to minimise hydrodynamic effects, such as dragging and vibration, by maintaining a suitable tension in the string. In addition, the buoyancy ensures a controlled resurfacing of the string during retrieval.

[6]For acoustic positioning.
[7]For the OM time calibration.

The optical module The optical module is the main sensitive element of the detector. The PMT and its associated electronics are housed in a $43\ cm$ diameter, $15\ mm$ thick, glass sphere, which can withstand pressures of up to 700 bars, produced by the Benthos Inc. Company. The sphere is made of two halves, one of which (the one opposite the PMT photocathode) is painted in black on its inner surface so as to give the OM some minimal directionality with respect to Čerenkov light detection without degrading its acceptance. The two halves have machined edges which form a seal when subjected to an external over-pressure. Attenuation of light at $\lambda = 450\ nm$ due to the sphere was measured to be less than 2%.

Silicone gel, covering the entire photocathode area, ensures both optical coupling and mechanical support of the PMT. Its refractive index ($n_{gel} = 1.40$) does not exactly match that of the sphere ($n_{glass} = 1.48$) but is higher than the refractive index of water ($n_{water} = 1.35$) in such a way as to minimize the amount of light reflected out of the OM. The attenuation of light caused by the gel is negligible with respect to the one due to the glass sphere.

A cage made of $1.1\ mm$ thick high-permittivity alloy wire is used to shield the PMT from the Earth's magnetic field and minimize the dependence of the detector response upon its angle to the magnetic North. The mesh size of the cage ($6.8\ cm$) was optimized to reduce the non-uniformity of the PMT angular response to less than 5% while minimizing the fraction of light lost due to the shadow on the photocathode.

Several PMTs of different diameters have been studied before coming to the final choice of the Hamamatsu R7081-20 PMT. It is a hemispherical tube made of borosilicate glass, 10 inches in diameter, with a bialkali photocathode and a 14-stage amplification system. The quantum efficiency for the specific combination of window and photocathode materials is shown if figure 3.8. The nominal gain of 10^8 is reached for a high voltage of about $2500\ V$. Its performances are summarised below in terms of a small number of critical parameters, only a fraction of those which have been measured [27].

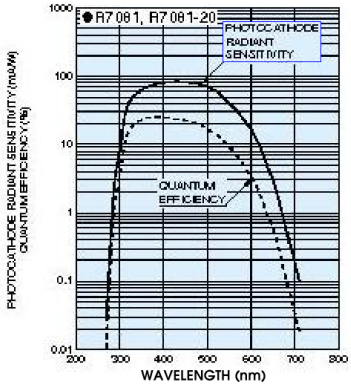

Figure 3.8: Hamamatsu measurements of Q.E. for PMT R7081.

Electromagnetic interference in the OM induces less than $5\ mV$ (rms) noise at the PMT anode. The gain at which the PMT is operated must be chosen taking this noise

into account. A factor of 10 between the average pulse height for a single photo electron (SPE) and the pedestal is sufficient to ensure efficient discrimination of the signal. This corresponds to an effective working gain of the order of $5 \cdot 10^7$, but in view of ageing a maximum gain of at least 10^8 is required.
The effective photocathode area is defined as the detection area of the photocathode weighted by the collection efficiency. It was measured by scanning the entire photocathode surface with a collimated blue LED and a value of $440\ cm^2$ has been obtained.
The peak to valley ratio is computed from the observed charge spectrum of single photoelectrons with the high voltage adjusted to give $50\ mV$ amplitude for SPE. It is measured to be 2 at the nominal gain of 10^8.
Due to small imperfections in the electron optics and the finite size of the photocathode, the SPE transit time between the photocathode and the first dynode has a measurable width, usually referred to as the transit time spread (TTS). This defines the timing resolution of the PMT, which is required to be comparable to that from the overall positional accuracy ($1.3\ ns$ RMS) and the timing precision in the readout electronics ($3\ ns$ FWHM). The measurement of the TTS is performed over the whole photocathode area with the PMT operating at a gain of 10^8 yelding $3.3\ ns$ FWHM.

3.1.2 The Instrumentation Line

Knowledge of light and sound speed in water is essential for track reconstruction, while knowledge of deep sea currents will help to correlate effects visible in the data (detector position variation, optical background modulation, effect of sedimentation) with marine properties. The main ANTARES detector strings host a few instruments[8] providing the minimum amount of information needed for data analysis.

The Instrumentation Line (IL) is a totally dedicated tool for monitoring environmental properties relevant to the detector calibration and data analysis. running in parallel to the rest of the experiment.

In order to simplify the construction and the data collection the Instrumentation Line uses the same mechanics developed for the other detector strings and the same read-out electronics and data transmission.
The basic instruments installed on the Instrumentation Line are:

[8] CTD and sound velocimeters. See footnote on page 49.

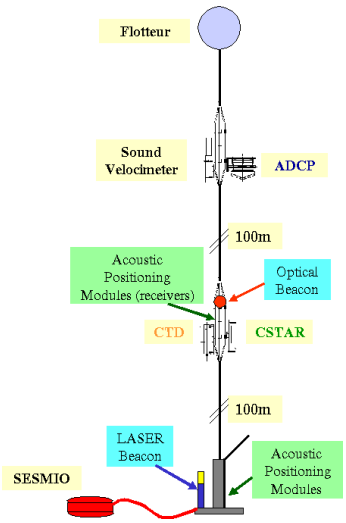

Figure 3.9: The Mini IL, a prototype of the final Instrumentation Line design.

- Acoustic Doppler Current Profiler (ADCP), to monitor the water current flow along the full height of the detector strings;
- Conductivity-Temperature-Depth (CTD) sensors, to monitor the temperature and salinity of the sea water at various depth;
- Sound Velocimeter, to monitor the sound velocity in sea water;
- Device to measure the light attenuation and absorption in sea water: a transmissiometer CSTAR of WetLabs;
- Seismometer.

It is also foreseen, at least at the beginning of the detector operation when only a few strings are deployed, that the Instrumentation Line will host the Laser Beacon and an Optical Beacon used for Optical Module time calibration.

The IL will be recovered (if needed) every one or two years to maintain instruments, to install new devices, and to monitor the behaviour of immersed material.

3.2 Offshore electronics and DAQ

The detector size and the distance between the detector and land do not allow to transmit analog signals and preclude a point-to-point connection between each OM and the shore station. Instead, an electro-optical cable from the shore station supplies electrical power to the detector array and permits data to flow in both directions using optical fibres. The electro-optical cable ends at the juction box to which the strings are connected. A star-topology network architecture is used, running from the string control module to the optical modules via the local control modules. A digital scheme has been devoloped for the necessary data multiplexing. This network is used to distribute power, collect data, broadcast slow control commands, distribute master clock signals, and form the trigger.

The OM electronics is constrainted by the limited space and power available. An Application Specific Integrated Circuit (ASIC) has been developed for the digital front end at the PMT output, tailored to the experiment needs. The circuit is called Analogue Ring Sampler (ARS) and three[9] of them are placed on the motherboard of each OM. Its block diagram is shown in figure 3.10. They

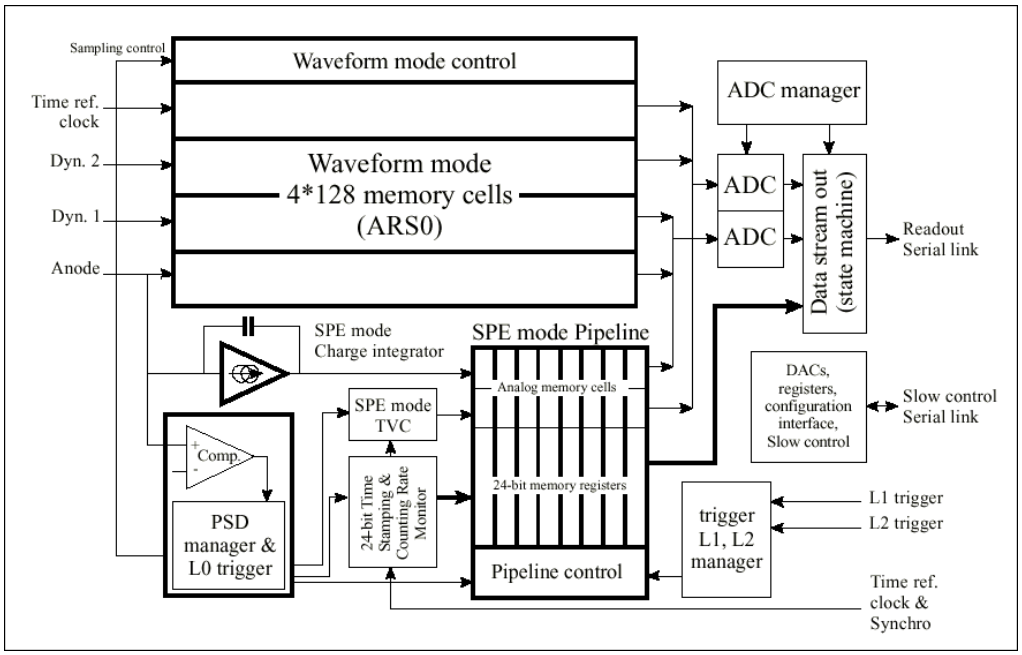

Figure 3.10: ARS1 block diagram

basically record all the pulse shapes either simple or more complex: the signal type is determined from a pulse shape discriminator (PSD) and processing is run in two different modes (WF and SPE). The PSD criterion is displayed in violet in the center of figure 3.11. The system allows to adjust the main parameters of the PSD, i.e. the large pulse threshold, the time over threshold and the time window for multiple pulses.

In figure 3.11 the main steps of data processing are shown. The chip samples the PMT signal[10] continuously at $1\ GHz$ and holds the analogue information on 128 switched capacitors when a low-level threshold is crossed (L0 trigger). A

[9]Only two ARS per OM are used for data taking in a "token ring" (see below), while the third one is used for triggering purpose only.

[10]The anode output, an attenuated anode output and a dynode output.

timebase $20\ MHz$ clock generated on shore is also sampled at $1\ GHz$ on one channel, giving a relative timing of the signals to better than $1\ ns$. Only if the

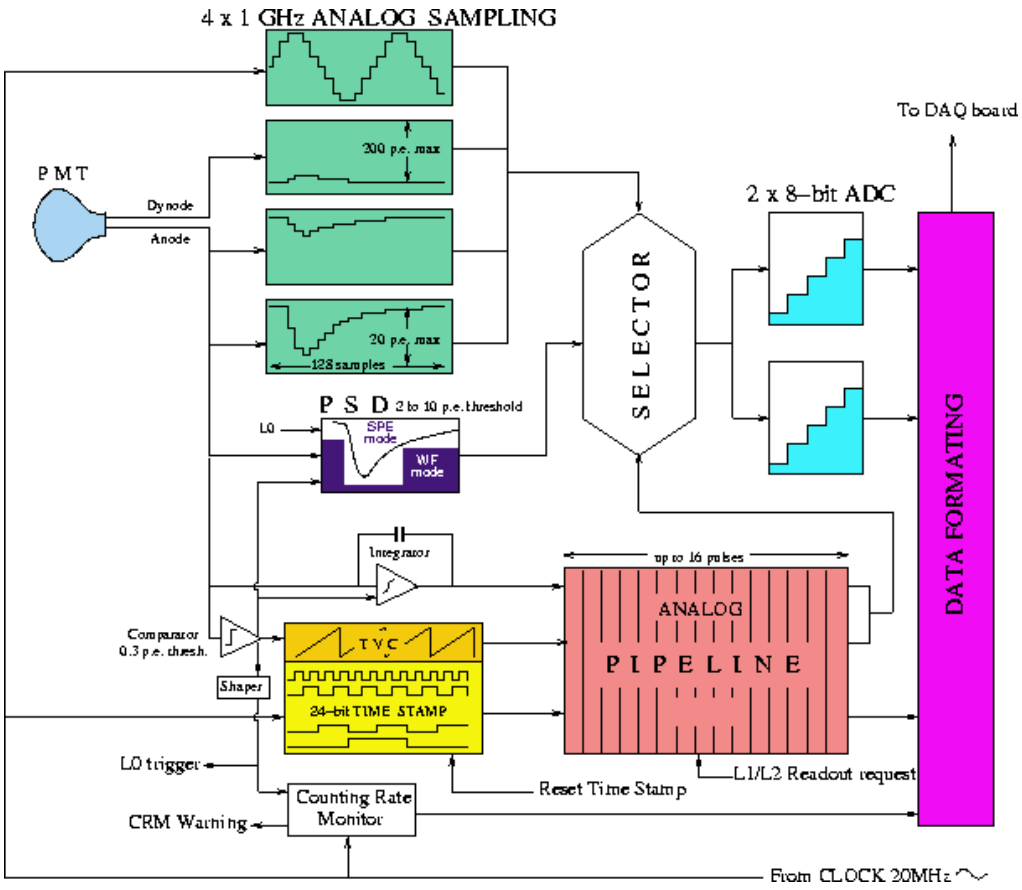

Figure 3.11: General description of signal processing.

PSD finds that the PMT signal output is longer or higher than the reference value, the information is digitized by an external 8-bit ADC , i.e. the event is processed in the full wave form (WF) mode.

The same external $20\ MHz$ clock is used by the Time-to-Voltage Converter (TVC) as well as the Time Stamp (TS). The TVC provides an analogue value proportional to the time when the L0 threshold was crossed in between two consecutive timebase clock cycles. Digitization by using 8-bit ADC provides time resolution of $0.2\ ns$.

The time stamp is obtained for each event by counting with 24-bit registers the $20\ MHz$ reference clock cycles.

A reset command sent through the clock stream is used to restart all the counters of the array synchronously.

Almost 99% of the pulses are single photoelectrons, whose pulse shape is implicitly known from PMT calibration measurements. Hence, if the signal is within the PSD gauge, the processing returns only the charge and the arrival time at a threshold crossing, and the information is transmitted to shore along with the OM address. This SPE mode reduces the dead time due to the event processing and the data flow, because the related information needs only four words (8 bytes). For the remaining 1% of the pulses processed in the WF mode, the pulse shape is also transferred to shore for offline analysis and this implies the processing of a larger amount of data, namely 263 bytes per event.

The ARS chip has also two extra features independent from the signal processing: the counting rate monitor (CRM), which generates a CRM event after a predefined[11] number of pulses, and the pulse generator for LED command[12].

A pipeline memory is implemented to store the SPE information long enough to match the readout request (RoR) propagation and formation time, which is around $10\ \mu s$ in the case of a RoR following a global L2 trigger. Two memories per optical module are used, in a token ring: the DAQ itself shares the data between them sending the event to the first free memory. This will permit the chip to be used in case of counting rates exceeding $60\ kHz$ and for a km-scale detector, where the trigger formation and propagation time may reach $30\ \mu s$.

3.2.1 Data formats

A summary of hit types and the corresponding data volumes can be found in table 3.1.

Event Type	SPE	WF	WF + dynode	RTS	STATUS	CRM
data (Bytes)	6	263	519	4	4	5

Table 3.1: Summary of the ARS hit data.

[11] This precount value is an adjustable number between 1 and 155.

[12] Single or 1024 pulses synchronised to the reference clock are delivered at a predefined rate or on the Time Stamp reset.

SPE A single photo-electron hit is generated if an input trigger (L1 or L2) coincides with the (internal) L0 trigger of a hit. It contains the header, the integrated charge (1 Byte), the time stamp (3 Bytes), and the TVC.

WF A waveform hit is generated if the signal passes the PSD criteria. It contains the SPE information and 128 samples of the anode signal. When both ARS chips are occupied by waveform hits, the data are reduced to those of a SPE hit. The PSD flag in the header is then set correspondingly.

WF+dynode A subset of waveform hits can contain waveform information from dynode signals as well.

RTS Reset time stamp events are generated each time the internal clock register is reset. This reset occurs when the ARS counter reaches its maximum or when an external RTS signal is applied. The header contains the last time stamp value before the reset.

STATUS Status events are generated by the ARS at power on or when slow control access starts or terminates. The ACQ/BUS flag in the header indicates the actual status. Status events contain the current time stamp value.

CRM Counting rate monitor events are generated by ARS each time the L0 precount is reached. It contains the header, time stamp and the time needed to reach the precount.

The data of each ARS are packed into *frames* and sent to shore by the process running on the LCM. A frame contains a header with information on the source, time stamp, data type, etc. When applicable, a list of hit items is included behind the header.

The frame header format[13] that was read by the datafilter has the following format:

[13] For a detailed explanation of data formats, see [51, 52].

Raw ARS frame header (32 bytes):		
FrameSize	U32	Total length of frame in 4-byte words
DataType	U16	Data type code (SPE, WF etc.)
FrameTarget	U16	On-shore farm PC handling this time slice
FrameTime	U64	Frame time stamp (units 50 ns)
FrameIndex	U32	Frame number since start of run
NbItemsOrg	U16	Number of L0 trigger happened in this data frame^{+}
NbItems	U16	Number of items sent in this data frame*
LCM_ID	U16	Identifier of originating LCM
ARS_ID	U16	Identifier of originating ARS inside LCM
RunNumber	U32	Unique run number

$^{+}$ From the FPGA, and not from the ARS. Implemented later.

* That is CRM items, for the PSL, rather than SPE items. The SPE format has been used for sending CRM events, hence 6 Bytes instead of 5 Bytes are used with one Byte set to zero.

The setup of the run (ARS threshold and CRM precount, PMT voltages, etc) is stored in a database together with the run number and the frame-time duration. The frame time duration is set through the slow control. During the entire life of the PSL in 2003 (see section 3.5.2), it was 2^{19} LCM clock cycles[14], i.e. $13107200\ ns$.

3.3 On shore data handling

Two main functions are implemented on shore: the data acquisition and the slow control for various aspects of detector operation.

The aim of the onshore data acquisition is to maintain an experiment status database using the slow control information, apply a filter of higher level with respect to offshore triggers (in order to reduce rates to a reasonable level for archiving on tape) and verify the data integrity.

The main purpose of the slow control system is to initiate and verify the configuration of the detector (through in-situ calibrations and instrument settings), the initialisation of all processes and the changes between the possible states of the DAQ system.

The first step of the on-shore processing is event building. Here, time-stamped data from various parts of the detector are assembled into events. Most of the

[14]For the CPU clock on each backplane, one cycle lasts $25\ ns$.

triggers are caused by accidental coincidences and these may be filtered in off-line reconstruction. The event building will associate both digital data from the OMs and slow-control data in the same event. Fully built events will be used for feedback in controlling the detector, as well as for event display and data monitoring. A Unix-based event display has been developed (and tested using the prototype strings) for this purpose. An online monitoring system is also used to monitor the quality of the data and the stability of the detector. This reduces the time required to detect errors and speeds up the verification procedure after expert intervention(s).

PMT voltage, temperature and power-supply voltages are read from the OMs, while information on string attitude, water current speed, acoustic positioning information and other control data are provided by dedicated instruments. Parameters to be adjusted during detector operation include the PMT voltage, thresholds involved in pulse detection and triggering, and various calibration systems.
Slow-control data acquisition and execution of slow-control commands are carried out by the processor on the motherboard of the relevant electronics container (OM, LCM, SCM or specialized instrumentation containers).

3.4 Trigger logic and rates

A schematic drawing of the off-shore trigger logic is displayed in figure 3.13. Only a level zero trigger is still used for the readout of single hits.

The level zero trigger occurs when the output of a PMT crosses a threshold corresponding to 30% of a SPE amplitude. Two peculiar examples of L0 triggers depending on the time duration of an event are shown in figure 3.12. The L0 trigger signal has a minimum time duration of Tw_{min}, adjustable between $10\ ns$ and $70\ ns$, and the maximum pulse width is 4 times Tw_{min}. Setting limits to the pulse width is needed in order to made coincidences between two OM in case of low amplitude pulses leading to very short Time Over Threshold (TOT) and to avoid any extra triggers in the falling tail of large amplitude pulses.

In order to deal with the high counting rate in the sea (see section 4.1), a level 1 trigger is built out of a tight time coincidence ($20\ ns$) between two L0 triggers from the same storey.

A level 2 trigger can be formed by requiring multiple L1 triggers in a coincidence gate whose width is of the order of that needed for a track to pass through the entire detector (about $2\ \mu s$). The L2 trigger condition could be at least two L1 triggers on the same string (L2_1: *string trigger*) or at least three L1 anywhere in

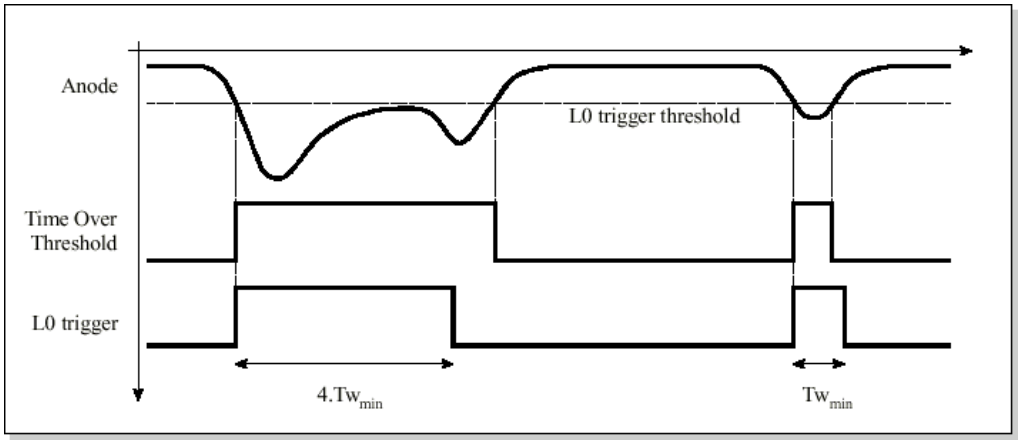

Figure 3.12: L0 trigger timing examples

the detector (L2_2: *array trigger*).

When either the string trigger or the array trigger conditions is satisfied, a readout request is sent to the entire array. The readout request is received in each ARS, which starts the digitization of all the information within the maximum allowed muon crossing time. Internal delays specific to each OM compensate for the trigger formation and readout request propagation times. When an L1 trigger occurs in a storey, the two OMs involved are read out, even if they do not participate in the subsequent L2 trigger.

The L1 trigger logic will be installed in each LCM, in the ARS motherboard and in a specific trigger motherboard of each LCM which uses Field Programmable Gate Array (FPGA) circuits. The L2 trigger logic must be linked to all the LCMs which may participate in the trigger, therefore the array trigger is installed in the junction box, while the string trigger will be installed at the bottom of each string (in the SCM) and then sent to the JB from which the readout request will originate.

The volume of data transmitted to shore depends on the trigger rate, the OM background and the proportion of WF events. Trigger rates and data flow due to random coincidences from background counting rates will be here estimated, in both cases of a readout request following either L0 or L1 trigger, assuming optimistic values of $75\ kHz$ for the L0 trigger base rate and a contribution from burst events during 30% of the time.

During a bioluminescent burst, L1 triggers from affected storeys provide no discrimination against noise, because often all the OMs in the storey “see” the

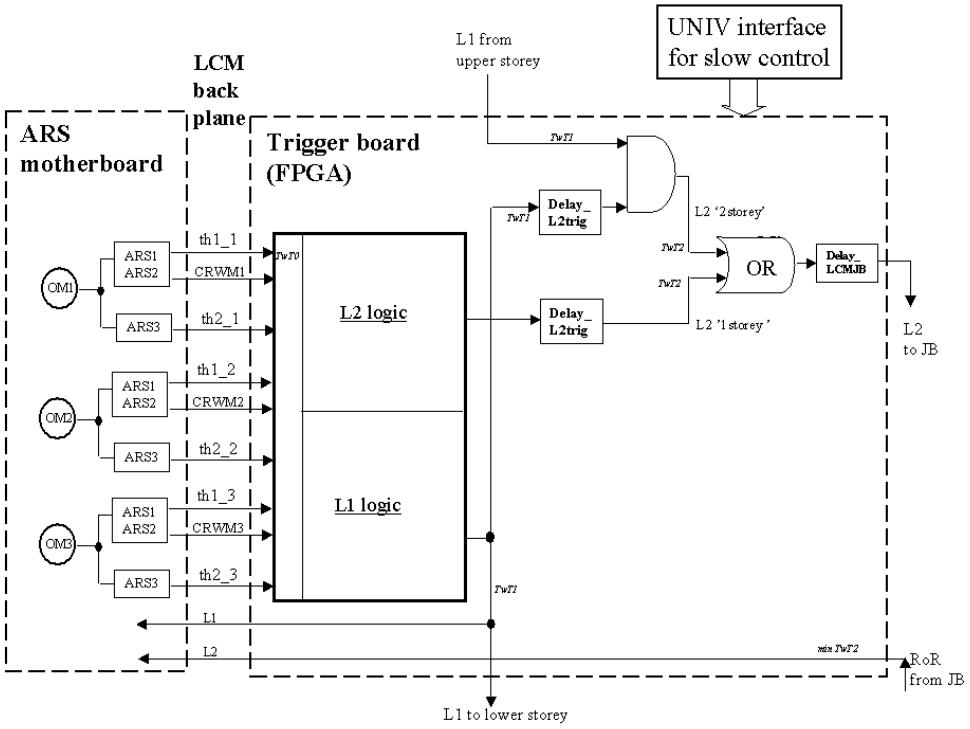

Figure 3.13: Trigger logic. The avoidance, in the initial phase of the experiment, of global RoRs has been recently suggested: all data generating a L0 trigger would be sent to shore.

burst. These storeys are removed from the trigger logic in real time, but the OMs are still read out, though it will be hard to recover the signal from the noise when tracks are reconstructed. Let us assume that the L1 trigger is disabled for modules affected by bioluminescence events (threshold at $500\ kHz$). From a distribution of raw rates one can extrapolate that the dead time in the detector will be less than 10% and the effective burst fraction will be reduced to 20% (with an average rate reduced at $300\ kHz$).

The average number of possible random coincidences in a OM triplet is $2 \cdot \frac{3!}{2!(3-2)!} \cdot R_1 \cdot R_2 \cdot \tau$. Assuming $R_1 = R_2 = R_3 = 75\ kHz$ 70% of the time and $R_1 = R_2 = R_3 = 300\ kHz$ 20% of the time, and using the L1 coincidence window $\tau = 20\ ns$, the L1 trigger rate will be: $6 \cdot (112.5 \cdot 0.7 + 1800 \cdot 0.2)\ Hz \approx 2.6\ kHz$ per storey, or $12 \cdot 25 \cdot 2.6\ kHz \approx 800\ kHz$ for the entire detector.

Accidental overlap of consecutive signals in the $50\ ns$ integration gate produces wide pulses detected as WF events 1% of the times at the base rate and 4%

of the times in burst regime, which on average correspond respectively to 68.6 bits and 130.2 bits per hit. Under these assumptions, the data flow rate for a readout[15] of the entire detector (900 OMs) following a L1 trigger is $6 \cdot (112.5 \cdot 0.7 \cdot 68.6 + 1800 \cdot 0.2 \cdot 130.2) \cdot 3$ bits$/s \approx 940$ Kbits$/s$ per storey or ≈ 2 Gbits$/s$ for the entire detector. The use of one of the type of L2 triggers described above will further reduce this number.

In a future situation of single L0 triggers readout, assuming the same $500\ kHz$ cutoff for bioluminescence, the average OM trigger rate would be $(75 * 0.7 + 300 * 0.2)\ kHz \approx 100\ kHz$, the average OM data flow rate would be $(75 * 0.7 * 68.6 + 300 * 0.2 * 130.2)$ Kbits$/s \approx 11$ Mbits$/s$, and the average data flow rate for the entire detector would reach 10 Gbits$/s$.

3.5 Status of the experiment

Since its very beginning ANTARES has followed an R&D programme focused on three major milestones:

- The construction and deployment of test lines dedicated to measuring environmental parameters such as optical background, biofouling and water transparency.
- The development of prototype strings to acquire the necessary practical expertise in the deployment and operation of an undersea detector up to the kilometer scale (see chapter 2).
- The development of software tools to explore the physics capabilities of the detector (see section B).

This R&D phase has demonstrated that the deployment and physics operation of such a detector is feasible. As a consequence, the construction of the detector is starting.

3.5.1 Site environmental parameters

The Mediterranean Sea represents an environment for a neutrino telescope that is quite different from those of the operating arrays at Lake Baikal (a freshwater lake which freezes in winter) and the South Pole.

[15] In the optimistic assumption that on average a single hit per OM is readout.

Therefore, in order to ensure the success of the deployment of a large scale detector in such an uncontrollable environment, an extensive programme of site evaluation and prototype testing has been necessary. A continuous environment monitoring will be done during the entire detector operation, thanks to a dedicated instrumented line deployed in conjunction with the 12 detector strings (see section 3.1.2). The detector will be deployed at a site near Toulon, at $42^o50'$ Northern latitude and $6^o10'$ Eastern longitude, at a depth of 2400 m under the sea level. The final choice of the site, illustrated in figure 3.14 satisfies the requirements

Figure 3.14: The ANTARES site, in the South cost of France.

on water transparency, optical background, fouling of optical surfaces, strength of the deep sea currents, meteorological conditions and depth. It also presents several advantages for the geographical position which allows an efficient on-shore support and is characterized by a large availability of infrastructure and pier.

Water optical properties The water transparency affects the muon detection efficiency, while the amount of scattered light determines the detector angular resolution. The optical properties also place strong constraints on the detector

geometry, because light attenuation limits the maximum spacing between optical modules that allow a good reconstruction of tracks with no information loss. Measurements and analysis performed in the ANTARES site [21, 22] give an absorption length in the range $25 \div 55\ m$ and an effective scattering length in the range $120 \div 300\ m$ from UV to blue light ($370 \div 470\ nm$).

Fouling The surfaces of optical modules exposed to sea water are affected by the combination of two fouling processes. The first one is the growth of living organisms, mostly bacteria, on the entire outer surface of the glass sphere. The second process is the fall of sediments, mainly originating from continental river beds, on upward-looking surfaces. The bacterial growth is almost transparent, but sediments adhere to the surface and make it gradually opaque. As shown in figure 3.15, measurements have demonstrated that fouling is significantly reduced for polar angles larger than 50 degrees with respect to the zenith. At the equator ($\theta = 90^o$ in figure 3.15), the fouling induces a transmission loss which saturates to 1.5% after eight months of immersion. This is an upper limit on the loss expected on the actual detector, where optical module axes will be oriented at a polar angle of 135 degrees with respect to the zenith [34].

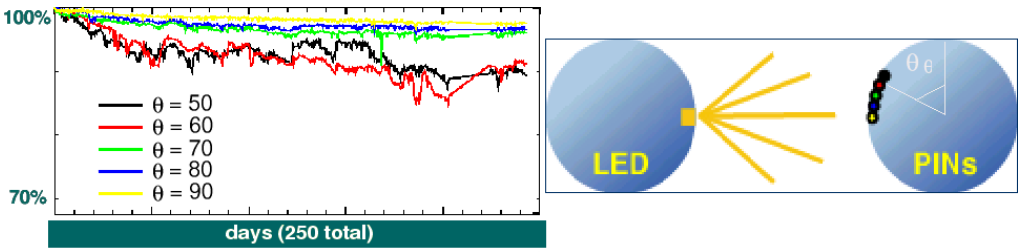

Figure 3.15: Light transmission as a function of time and polar angle.

Sea conditions Suitable sea conditions are required to perform deployment and recovery operations. These conditions depend both on the nature of the operations and on the characteristics of the ship. The favorable sea conditions specified for operations with the boat *Castor*[16], for example, are a wave height lower than $1.5\ m$ and a wind speed lower than 25 knots[17]. The analysis of data from a number of sources leads to the conclusion that periods of three consecutive days with these

[16] Belonging to the SERRA-MARINE company.
[17] Force 5 on the Beaufort scale.

specific conditions occur less than five times per month between October and April, and more than five times per month from May to September.

The strength and direction of undersea currents has been taken into account in the mechanical design of the detector. The strings well tolerate the maximum current speed presently observed, namely $19\ cm/s$ (see section 4.1.3).

A visual and bathymetric survey of the sea floor was also performed in the potential sites. It checked the absence of topographical anomalies, such as steps or rocks, which could obstacle the string deployment and anchoring and it also made sure that the floor substrate will be a satisfactory support for the detector.

3.5.2 Prototype lines deployed in 2003

In 2002/2003, the ANTARES collaboration has deployed at the ANTARES site a prototype line made of one single sector (PSL, Prototype Sector Line: deployed in December 2002) and a first version of the instrumentation line (MIL, Mini Instrumentation Line: deployed in February 2003) which have allowed the verification of the "final" design, in the final environment, using prototype electronics boards. They were intended to identify any problems as early as possible, in order to correct them before the production of the full $0.1\ km^2$ detector.

The sea deployment has permitted testing of many aspects of the design which would have been impossible to study in on-shore tests: the deployment/recuperation procedure itself, the power distribution via the sea electrode, the line movement, the acoustic and absolute positioning, the medium term corrosion effects, the evaluation of system reliability, to name but a handful.
Unfortunately, testing trigger rates and data volumes in final conditions, as well as in situ time calibration with OM flashers and optical beacons (with real scattering and absorption effects), had not been possible because of the lack of the global $20\ MHz$ clock from shore, due to a problem with the optic fiber which was intended to transmit the clock signal generated on shore.

The sector line consists of a single sector of 5 storeys, with the associated SCM/SPM and BSS, and a minimal DAQ system at the on-shore station. The lowest storey is at the nominal position, $100\ m$ from the sea bed, and the spacing between storeys is the old standard $12\ m$.

The MIL was equipped with 2 storeys separated by $100\ m$ and a BSS. The devices in the upper storey were the ADCP and the sound velocimeter, while in the bottom storey the CT probe and the transmissiometer were located. The seismometer was positioned $50\ m$ away from the MIL anchor.

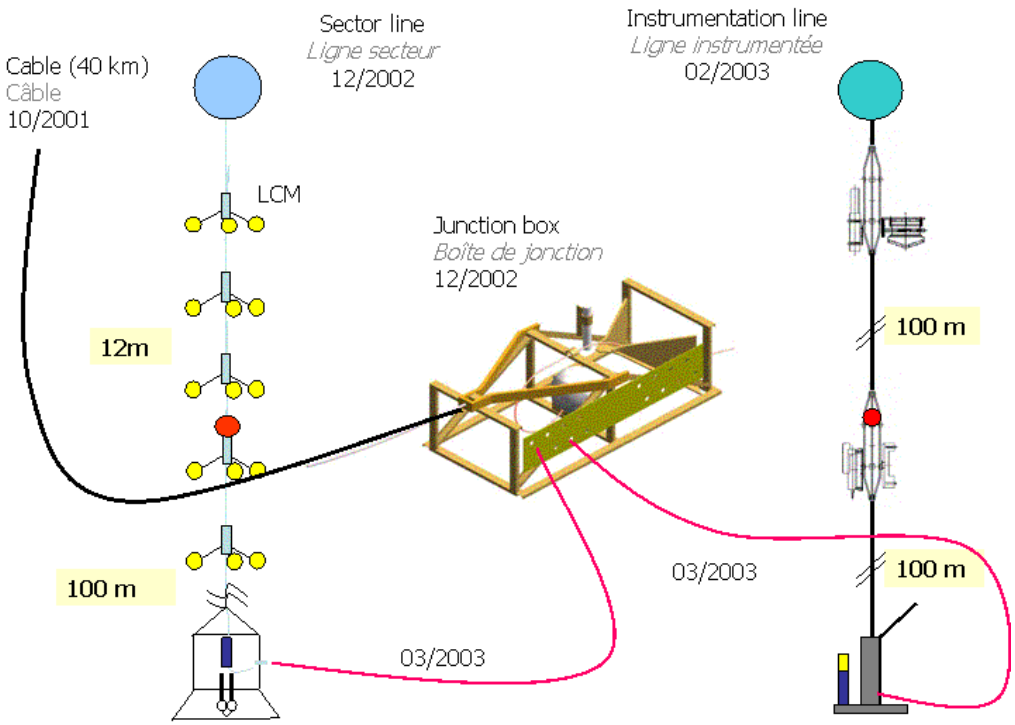

Figure 3.16: The layout of the two prototype strings as appeared after March 2003. PSL shown on the left, MIL on the right.

Both the MIL and the PSL were connected to the Junction Box in March 2003, and it was planned that they would be operating in conjunction. However, a water leakage due to a faulty washer of the MIL forced the recovering of the line for debug almost immediately (April 2003), while the PSL continued its operations until the first weeks of July.
Furthermore both lines have been affected by several problems.
The main issues on the MIL have been the failure of clock distribution for triggering the acoustic positioning system (because of a break of the optical fibre), and the water leak on the MLCM which damaged MLCM and LCM electronics (the latter because of migration of water through the EMC). The acquisition of the environmental parameters (seismic activity, light absorption, sea currents, sound velocity, conductivity, pressure, temperatures) was not impeded by the clock problem, but data were collected for 3 days only due to the flood of the MLCM.
In the PSL, the early failure of some capacitors on the PMT basis, a problem with

a DC/DC converter on the same location and some booting problem caused the malfunctioning of all three OMs of LCM 2, while the LCM 3 stopped working because of a water leak. Moreover the clock did not propagate from the SCM to the LCM clock-boards, because the high pressure and tension endured by the demanded fiber harmed the signal transmission. Without the clock, the ARSs cannot be enabled, therefore neither SPE[18] nor WF events could be acquired, but they did transmit some data even though not enabled: the CRM events. These can be used to measure the singles rates as functions of time, HV and ARS threshold values. In absence of the global clock, the LCM clocks have local $20\ MHz$ oscillators, which are *not* synchronised[19], though.

For the next future, between the end of this year and the beginning of 2005, the deployment of two "new" test strings is scheduled: the MILOM, a new 3-storeys version of the MIL with optical modules and the old devices but new electronics, and again the (repaired) PSL line, with 4 storeys only (the broken LCM 2 will not be replaced) and using a new reinforced EM cable.
The main objectives of MILOM and PSL2 are the validation of the new EM Cable in real conditions, the test and validation of the new electronics, long term monitoring of environmental parameters and their correlations, procedure developments and checks for in situ calibration, and all those tests which were not possible with the MIL and PSL because of the failures mentioned above.

The deployment of the first of the 12 final strings will take place only a few months later and the whole detector will be operational within the following two years.

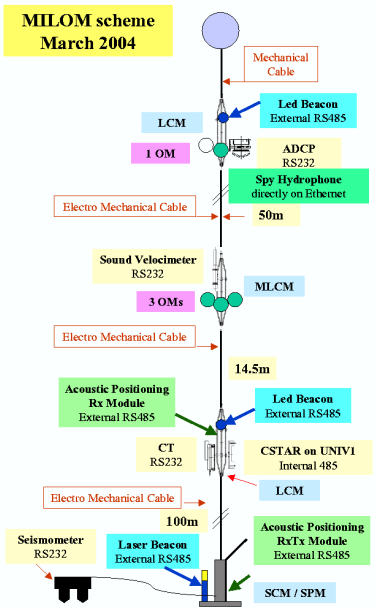

Figure 3.17: MILOM layout, as agreed upon in March 2004.

[18]For more details on data formats, see section 3.2 and section 3.2.1.

[19]If they had been synchronized a time resolution $\approx 25/\sqrt{12}\ ns$ would have been gained on every L0 by setting the CRM precount equal to 1.

Chapter 4

The Optical Background

4.1 Background analysis

The analysis presented in this chapter aims at establishing the nature and behaviour of the optical background sources and determining the possible long-time variations and correlations with other environmental parameters. A precise characterization of the background sources is necessary to optimize the choice of the detector trigger, by tuning the algorithms in order to minimize the dead time. To this purpose, in the MonteCarlo simulation an accurate parametrization of the background is equally important as the physical event generation.

Since the beginning, several measurements of the optical background have been performed at different depths on the ANTARES site as well as on another site near Corsica[1], in order to perform a comparison. These results have been reported in a large number of publications and presentations. Because of different hardware problems and slight modifications to the string arrangement from test to test, it is not always possible to apply appropriate corrections to the data in order to compare the different results. Consequently, only the ones which are more relevant for the experiment will be reported here.

The general line setup used in the tests consisted essentially of two or three optical modules, located in such a way as to have at least one close pair, and a currentmeter. The two close OM (called A and B) are mainly used to study coincidences and correlations. If present, the third OM (called C) was located further down in the line ($10 \div 40\ m$ deeper), in order to study the dependence of signal correlations upon PMT separation. Each optical module consisted of a

[1] About $40\ km$ off Porto ($42^o22'$ N, $8^o15'$ E), at a depth of $2680\ m$.

$10''$ Hamamatsu PMT[2], shielded by a μ-metal cage and enclosed in the standard Benthos glass sphere. Recorded data comprised the time needed to reach a preset value on the single counter for OM A, the counts reached during this period by the OM B (and C) single counter and the number of coincidences for all possible pairs. The threshold on the PMT output signal was normally set to 0.3 p.e.; higher threshold values were also sometimes used to check the background contribution at larger photon yields.

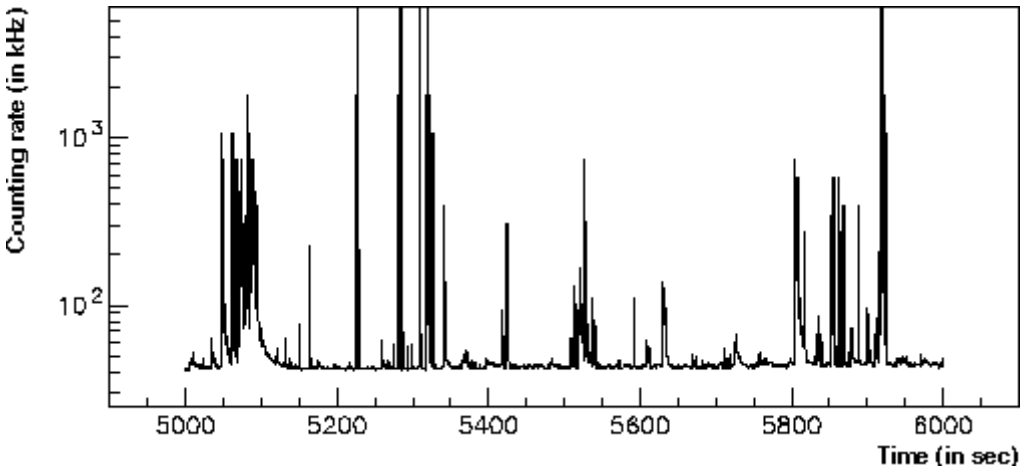

Figure 4.1: Example of background rate time stream. [30]

Two different components can be identified. A continuous background, whose frequency varies slowly in time over periods of several hours, and usually corresponds to several tens of kHz for a $10''$ PMT; a few sharp peaks, ranging up to tens of MHz and lasting few seconds, sticking out of the continuous component. In order to quantify the background, two definitions were introduced: the *continuous component* is the lower envelope of the plot representing the counting rate of a given OM as a function of time; the *bioluminescence activity* (or *burst activity*) is the fraction of time during which a given OM exhibits a counting frequency higher than $200\ kHz$[3] at the 0.3 p.e. level. Both quantities are usually evaluated over time spans of half an hour.

[2]Before 1999, the $8''$ Hamamatsu R5912 PMTs were used. Anyway, all the data presented here are re-scaled to the $10''$ Hamamatsu R7081 PMT, which is the one chosen for the final detector.

[3]This frequency corresponds to the one for which a sizable amount of dead time was expected. Periods of high bioluminescence activity can last for as long as a day, causing a large dead time on the affected PMTs during this period [34].

As already introduced in the previous chapter, the background light is known to be caused by the radioactive decay of isotopes naturally present in the sea salt and bioluminescent living organisms.
The activity of the continuous component is expected to be caused mainly by ^{40}K-decay, however another contribution must be present. Since the water salinity remained approximately constant to $3.85\ PSU$[4] throughout the tests, and the Potassium contribution to the salinity is stable at 1.11%, the large modulation[5] registered in the tests cannot be explained by a varying level of ^{40}K counts. Moreover simulations (see section 4.1.1) set for the ^{40}K contribution an upper limit consistent with the lower rate observed, which is $\approx 27\ kHz$ for a $10''$ PMT with the threshold set at 0.3 p.e. . The excess observed in the continuous component is therefore probably caused by a slightly variable bioluminescence component, due for example to large numbers of bacteria glowing. The modulation of the continuous component is, in fact, not correlated[6] with periods of high burst activity, and this suggests that the two effects may be caused by two distinct biological populations [30].

By setting the threshold at 2 p.e. one suppresses the noise by about a factor 100, reducing the continuous component to $\approx 300\ Hz$. Coincidences of two photons on a single module account for roughly $50\ Hz$ only. Most of the contribution comes instead from the tail of the 1 p.e. distribution. This assumption is confirmed by the coherent modulation with the same relative amplitude of the 2 p.e. with respect to the 0.3 p.e. signals [30].

Although the singles rates exhibit a large modulation caused by bioluminescence, the coincidence rate between nearby PMTs are constant at $25.4\ Hz$ over a 12-hour period: this indicates that coincidences are only produced by the (constant) ^{40}K background.

There is a clear indication of correlation[7] of signals from two nearby modules in periods of high activity. This correlation is strongly dependent on the PMT separation.

A pronounced dependence of bioluminescence activity on current speed is also

[4] 1 *Pratical Salinity Unit*= 1 g of salt per Kg of water.

[5] The base-line background is found to double over a time scale of a few hours at the ANTARES site. The Corsica site presented a lower activity.

[6] The correlation between the two components appears only when the intense burst activity artificially increases the continuum level. [33]

[7] The correlation coefficient is defined as $\frac{<f_A(t)\cdot f_B(t)> - <f_A(t)><f_B(t)>}{\sqrt{<f_A(t)^2> - <f_A(t)>^2}\sqrt{<f_B(t)^2> - <f_B(t)>^2}}$, where $f_A(t)$ and $f_B(t)$ are the background rates respectively for the OM A and B. It ranges from -1 to 1 and it is 0 for totally uncorrelated signals.

found. It exhibits slight variations both from site to site and within the same site in different seasons.

In the present MonteCarlo version, the continuous background component is simulated (as 1 p.e.-events) together with Čerenkov light from physical events, while no simulation of the bioluminescence bursts is used[8].

4.1.1 Radioactive decays

Radioactive decays affect the entire detector 100% of the time, so that all triggered events will contain a significant fraction of this hard to remove background. The presence of this background somehow worsens not only the trigger rate (and the effective area), but also the whole analysis, including the angular and energy resolution.

^{40}K decay is the main source of radioactive background. Its contribution is easily simulated since the physics involved is well known. ^{40}K decays with a half-time of $1.277 \cdot 10^9\ yr$ [67] in two dominant modes, both usually resulting in Čerenkov radiation between 300 and $600\ nm$.

- In the case $^{40}\mathrm{K} \longrightarrow {}^{40}\mathrm{Ca} + e^- + \overline{\nu}_e$ (BR = 89.3%) the electron, emitted with a maximum kinetic energy of $1.311\ MeV$ (mean total energy of $1.12\ MeV$), is 90% of the time above the threshold for Čerenkov light emission in water. The electrons travel an average length of $2.3\ mm$ emitting on average 43 photons. Due to multiple scattering of electrons, photons may lose much of the information concerning the initial electron direction. No secondary particles are produced above Čerenkov threshold.

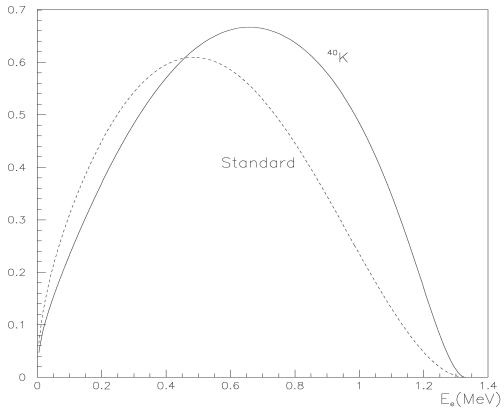

Figure 4.2: β^- decay spectrum, compared to a standard β spectrum without Coulomb and spin corrections. The spectrum is shifted towards higher electron energies, and the probability of being above the Čerenkov threshold for light emission in water is therefore increased. Figure taken from [31].

[8]Though an old simulation existed within the Trigger Simulation Software. It generated ^{40}K and bioluminescence hits within the ARS data generation simulation. [24]

- In the case $^{40}\mathrm{K} \xrightarrow{\mathrm{EC}} {}^{40}\mathrm{Ar}^{*}\ (+\overline{\nu}_e) \longrightarrow {}^{40}\mathrm{Ar} + \gamma$, which has a 10.7% probability, the emitted γ ($1.461\ MeV$) gives (on average) 1.6 Compton electrons which can in turn radiate Čerenkov light.
  Electrons produced have a mean energy of $1.2\ MeV$, and 1 EC generates on average about 85 Čerenkov photons.

These calculations show that Čerenkov photons are more efficiently produced starting from the $1.461\ MeV$ photon: the contribution of the EC decay mode to the observed signal is 18%, higher than the BR for this channel.

Only few other isotopes can produce significant signals in a water Čerenkov detector. Apart from ^{40}K, ^{238}U is worth noting: it has a long decay chain with many β-decays above the Čerenkov threshold. The overall rate of the β-decays in the ^{238}U chain is about a factor 50 lower than the ^{40}K rate, but some of such decays produce many more Čerenkov photons than a ^{40}K event. Therefore their contribution to coincidence rates could be detectable. Apart from radioactivity due to long lived species, some cosmogenic isotopes are continuously produced by cosmic ray interactions. However, the endpoints of the corresponding electron energy spectra are below Čerenkov threshold and cannot contribute to a detectable signal.

With the assumption that at the ANTARES site the salinity is $38.5\ PSU$ and the attenuation length is $41 \pm 2\ m$, Monte Carlo simulations [31, 32] predict a contribution from radioactive decay of $26 \pm 5\ kHz$ for the $10''$ PMT.

The GEANT3.21-based simulations that lead to these results take into account all the relevant processes involving e^-. The only limitations to the precision of the result lie in the accuracy with which the OM and PMT are modeled and the amount of CPU resources available. These are critical, because a significant contribution to the observed rate comes even from radial distances of $20\ m$ from an OM. The r^{-2} suppression factor due to the isotropy of the decay process is roughly compensated by the increased volume (and hence the increased potassium amount) in the water shell of interest. Only the particle range (the γ's from the EC travel on average $68\ cm$) and the attenuation length ($\approx 50\ m$) limit the water volume which contributes to the signal. Therefore an analytical extrapolation towards radii even larger than $20\ m$ is necessary to obtain precise results.

4.1.2 Bioluminescence

Bioluminescence, phosphorescence and fluorescence are different forms of luminescence. The last two phenomena are characterized by the absorption of pho-

tons, followed by their re-emission at red-shifted wavelengths; the duration of the emission is longer for phosphorescence than for fluorescence. On the contrary, bioluminescence is not stimulated by light: at its origin there is a chemical reaction which takes place in a living organism[9].

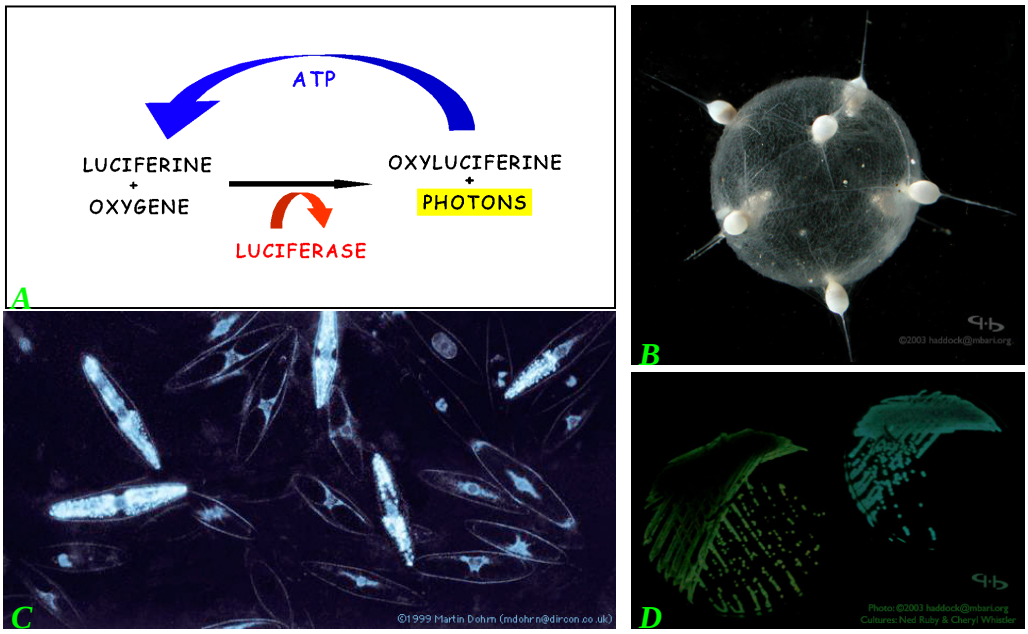

Figure 4.3: Courtesy of [37]. ***A*:** Schematic diagram of the chemical reaction which forms the basis of bioluminescence. ***B*:** A colony of radiolarians *Tuscaridium cygneum* (diameter $\approx 1.2\,cm$). ***C*:** Bioluminescence in a population of the dinoflagellate *Pyrocystis fusiformis* (unicellular alga with a length $1\,mm$). A black-and-white image was recorded with a low-light camera connected to a microscope, while full natural colour was added afterwards. ***D*:** Most luminous bacteria produces blue or blue-green light, but the culture plate of a strain of *Vibrio* on the left exhibits a yellowish color: this is not the case for the normal wild type (on the right). The image has not been colourized, but may not be spectrally perfect due to the settings of the camera.

There are a multitude of ways that bioluminescence serves to augment visual communication and optical concealment in the pelagic enviroment and these can generally be grouped into three major categories: hunting, reproduction, deterrent to predation.

[9]Chemiluminescence is a general term for production of light when the excitation energy originates from a chemical reaction. Bioluminescence is a kind of chemiluminescence, where the light-producing chemical reaction occurs inside an organism.

In dim light, it can aid in the search for prey, either by enhancing the visibility of a lure or by illuminating prey with a luminescent flashlight. Species specific bioluminescent displays can also be used to attract a mate. Bioluminescence also serve for camouflage, to distract or blind a predator or even to call for help.

The emission mechanism has been studied on several organisms, especially those belonging to the marine fauna, among whom bioluminescence is most frequently present. There exists a large number of chemical mechanisms involving a big variety of enzymes (depending on the different organisms) and sometimes also a co-factor (which is calcium, most of the times), but the general mechanism is substantially the same. A *luciferase* molecule catalyzes the oxydation of the pigment *luciferin*, and this reaction produces a photon plus the inactive *oxyluciferin* molecule (see figure 4.3-***A***). *Adenosine TriPhosphate* (ATP) is involved both in the oxidation itself and the inverse reaction from oxyluciferin to the fundamental

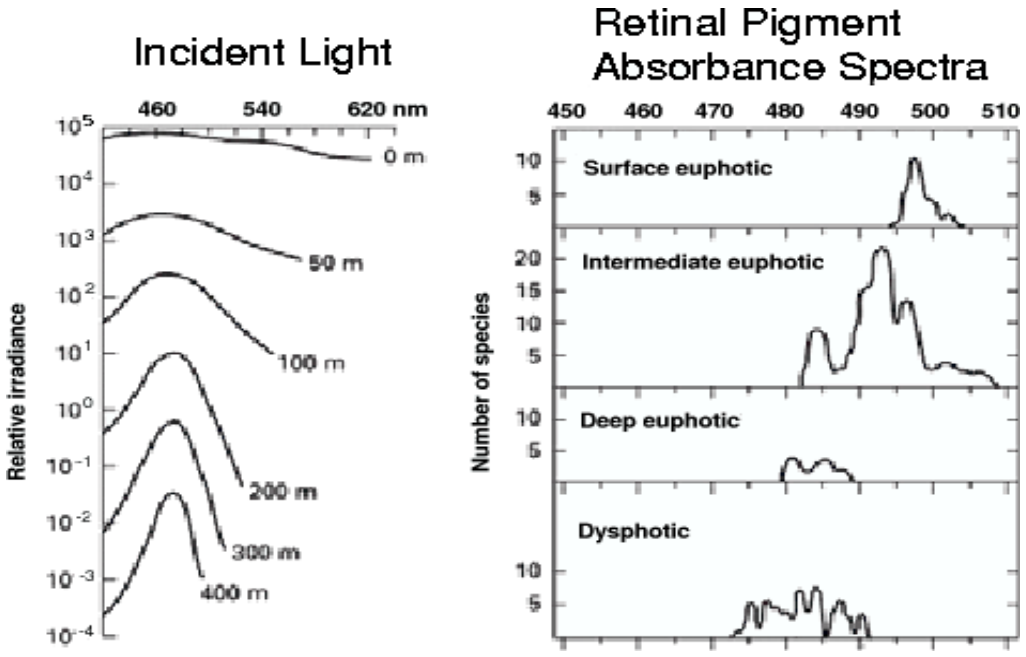

Figure 4.4: Wavelengths in the sea: incident sunlight (left) and retinal absorption spectra (right) as functions of depht. The water depths where photosynthesis may occur (up $120 \div 130\ m$ maximum) are called *euphotic*. At larger dephts the light is still sufficient to allow vision, but not for the photosynthesis process: this is the *dysphotic* region, which reaches dephts of $500 \div 800\ m$. Greater dephts, where there is a perpetual darkness, is called *aphotic* zone.

state of the substrate. Whatever the luciferase and luciferin molecules are, in any case the efficiency of the bioluminescence mechanisms is always 100%.

Marine bioluminescence is produced by an incredible range of organisms, from bacteria and mono-cellular protists to squid, fish and jellyfish: 70% of all species and 90% of all organisms living in the deep sea[10] are bioluminescent. Examples of the smallest ones are shown in figure 4.3. In the large majority of multicellular species, luminescence is controlled through the nervous system. In unicellular organisms like dinoflagellates or radiolarians, instead, bioluminescence is caused by an internal pressure gradient ($1\ dyn \cdot cm^{-2}$) which follows a deformation of the cellular membrane.

At depths around $1\ km$, due to spectral filtering by the upper water column, the residual sunlight is restricted to a narrow band of radiation around 470 which is the window of greatest optical transparency of seawater. In figure 4.4 we may see that absorption spectra of fish living at these depths undergo a shift in frequency parallel to the change in frequency of residual sunlight yield. It is not surprising, therefore, that the second source of light in the sea, the bioluminescence produced by the fauna itself, has an emission maxima at the same wavelengths as the remaining sunlight.

Beyond $1\ km$ sunlight totally disappears, but bioluminescence light is still present at the same wavelenghts which correspond to the minimum in light absorption by seawater.

Bioluminescent organisms in the deep sea usually emit between $430\ nm$ and $480\ nm$, though few species have fluorescent proteins that absorb an initially blue emission and emit it shifted towards the green or even the red. Some examples of emission spectra are shown in figure 4.5.

At shallow depths, the intensity of luminescence by photosynthetic organisms can be influenced by the intensity of sunlight the previous day. In some instances, in the case of marine invertebrates with light receptors, light emission can be induced by photic excitation: this *empathetic* luminescence has a

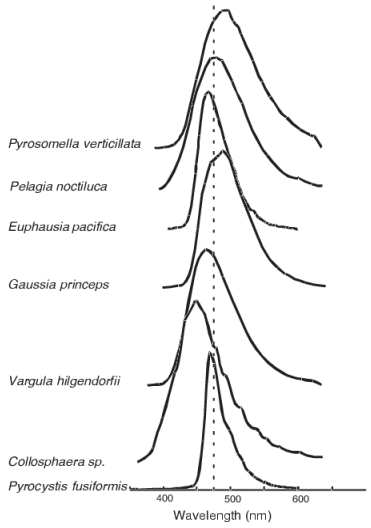

Figure 4.5: Bioluminescence emission spectra measured from some common planktonic organisms. Dotted vertical line at $475\ nm$. [42]

[10] Below $500\ m$.

yet undemonstrated potential to enhance the luminescence generated by external sources, even by another luminescing organism [37].

Bacteria emit light continuously, but most organisms emit flashes of durations ranging from about $0.1\ s$ (like dinoflagellates) to tens of seconds (like some jellyfishes). Even the total number of photons emitted in a burst may vary from 10^8 for dinoflagellates to 10^{12} for jellyfishes [40].

Though the existence of bioluminescent organisms at great dephts is well established, no precise information is available. A direct study of the fauna is indeed difficult at these prohibitive depths; furthermore the environmental conditions are hardly reproducible in a laboratory. And even if something is known about bioluminescence in the deep ocean, there is presently almost no data on Mediterranean fauna at depths beyond $1\ km$[11].
Thanks to the collaboration with a skilled and equipped sea science institute external to the ANTARES experiment, the University of Aberdeen (Scotland), some

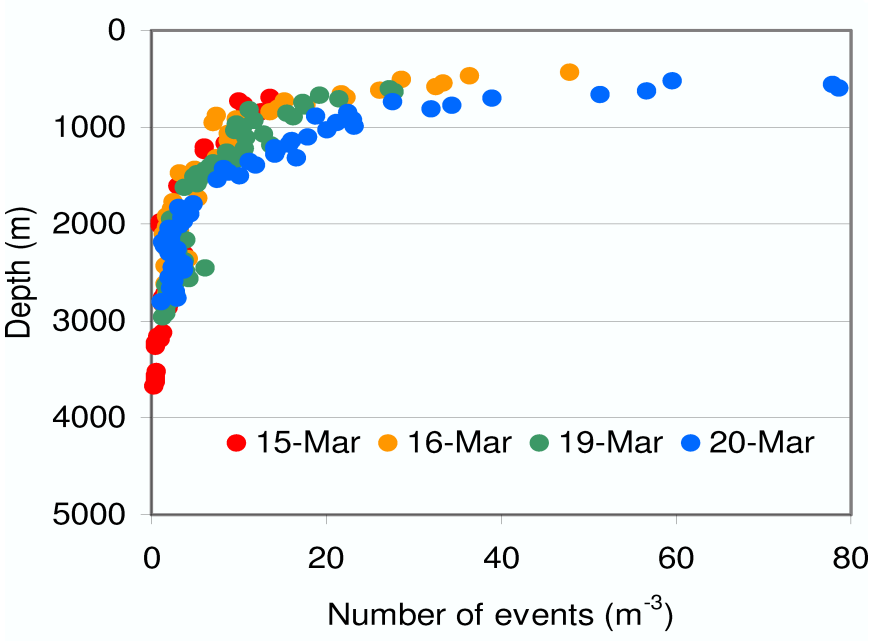

Figure 4.6: Bioluminescence intensity vs depth [41]. Measurements taken at Porcupine Seabight (West of Ireland) in March 2002 with the same apparatus which is now used at the ANTARES site by the Aberdeen group.

[11]Private communication by Anne Sophie Cussatlegras, Centre d'Océanologie de Marseille, and Amandine Heger, University of Aberdeen.

campaigns (in January and May 2004) at the ANTARES site have already been performed. Unfortunately an analysis of the most recent data is still not available. Anyway it is well known that the importance of the phenomenon is reduced with increasing depth, following a profile similar to the one in figure 4.6.

The decrease of the signal correlations upon the PMT separation, evidenced since earlier measurements [30], favours the idea that light emission is local, close to the optical modules. This also corroborates the hypothesis that the bioluminescent fauna of interest is mainly composed of unicellular plankton, which flashes because of a pressure gradient.

Though hard to model and predict, bioluminescence will only affect some parts of the detector at given moments in a very specific and recognizable manner: biological activity is known to produce light in an incoherent way. This means that photons are detected on a 1 p.e. basis and they arrive uncorrelated on time scales of a few nanoseconds.

The occurrence of bioluminescence can then be easily detected and its effect filtered out by "switching off" (at a software level) those parts of the detector which have entered a "bioluminescence state"[12]. The resulting effect will be to occasionally create "holes" in the detector, leaving the rest largely unaffected.

4.1.3 Sea current $\&$ background

The current speed and direction have been monitored for several days in different periods of the year. The current intensity globally varied from 0 to $19\ cm/s$, but the range and average value may differ considerably from test to test. As an example, results of current measurements obtained in March 1999 are shown in figure 4.7: a clear preferential direction of the current, from East to West (corresponding to the Ligure current) was observed. A general trend of increasing burst rate with increasing current speed always appears in the data. As an example, results from measurements in 1997-1998 are shown in figure 4.9. This corroborates the hypothesis that the current reaching the line creates turbulence perturbing bioluminescent organisms. A similar correlation was also seen between current speed and the continuous component of the background, during the same periods in which a correlation between burst activity and base-line rate was noticed. An interesting effect that has been picked out in the current behaviour are inertial oscillation, due to the action of the Coriolis force on moving fluids. It is a well

[12] In ANTARES, when a given OM exhibits a counting rate higher than $500\ kHz$, a "bioluminescence state" is entered.

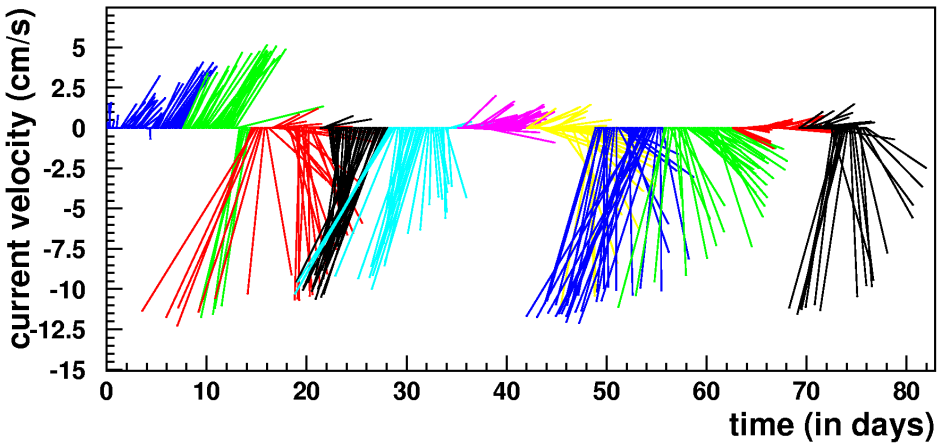

Figure 4.7: Polar plot of the water current as a function of time. The length of each segment indicates the current intensity in cm/s on both axes. The orientation of the segment indicates where the current comes from (in the horizontal plane): North is to the right, East is down. The abscissa of the origin ($y = 0$ axis) of each segment indicates the time at which the measurement was started. The different colours draw a distinction between successive 8-days periods of data taking, for the sake of clarity. Data from measurements performed on the ANTARES site [33].

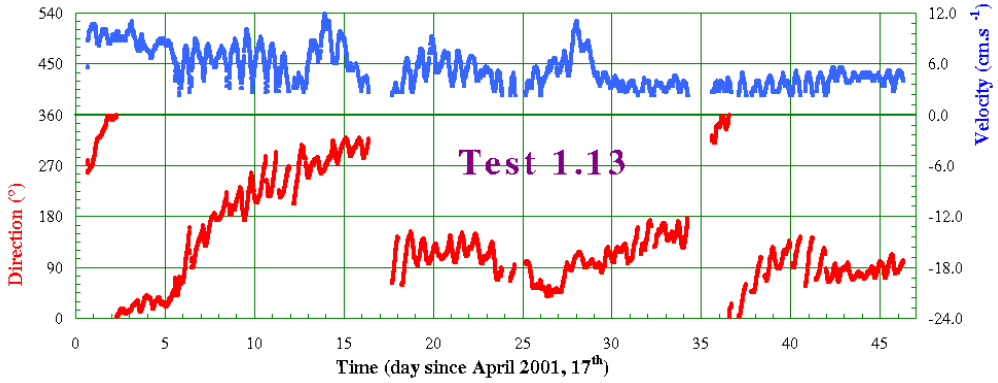

Figure 4.8: Current measurements in test 1.13: direction and speed. [35]

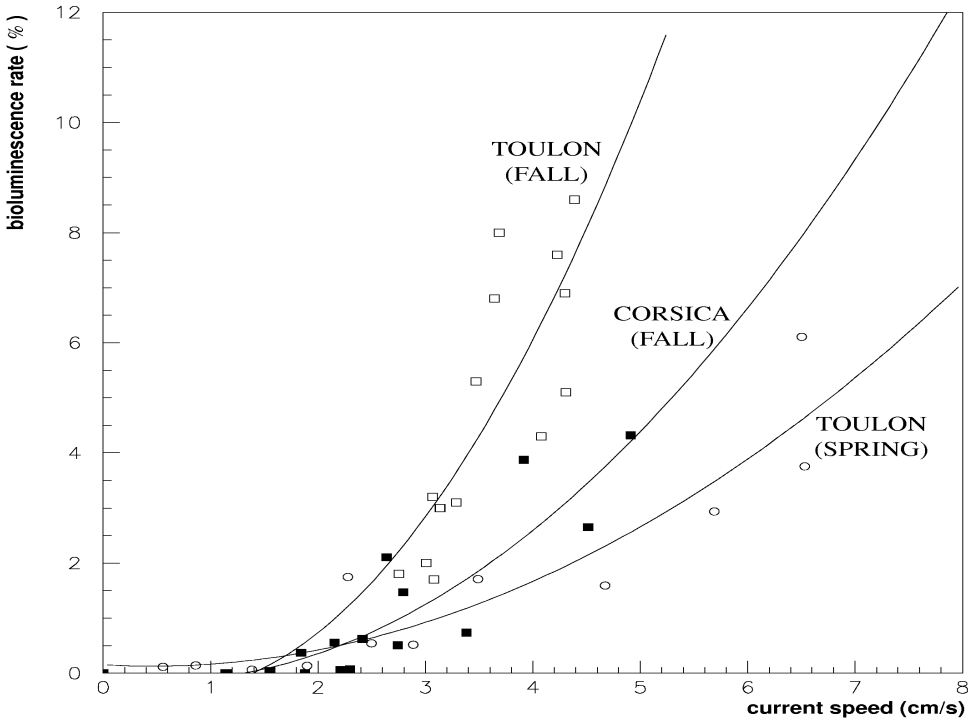

Figure 4.9: Correlation between bioluminescence activity and current speed for tests 1.6 (open squares), 1.7 (filled squares) and 1.8 (open circles). A fit with a second degree polynomial is superimposed on top of the data from each individual test. [30]

known effect in oceanography: assuming that only Coriolis force and gravity act on the water, and that the vertical[13] motion of water is negligible, one may predict an oscillation in current direction and speed[14] with a frequency $2\Omega \sin\lambda$, where $\Omega^{-1} = 23.9344696\ h$ is the sidereal day and λ is the latitude. The resulting period of oscillation at the ANTARES latitude[15] is $17.6\ h$, in satisfactory agreement with measurements shown by the plot in figure 4.8 where 7 oscillations can be counted in approximatively 5 days.

[13] Parallel to gravity.
[14] In case that an additional not-inertial contribution to the sea current does exist.
[15] $42^o 50'$.

4.2 Data obtained in 2003

The most recent background measurements are those from the Prototype Sector Line (see section 3.5.2). It acquired data from March 31 to July 10, 2003 and, in spite of several problems met during its operating period, the PSL provides the most abundant and complete information on the background at the ANTARES site when compared with previous tests. During the last weeks of operation, moreover, the standard test line was deployed again in order to obtain some comparative measurements. This last test will be referred to as 1.17 from now on.

In the PSL data analysis, the quantities previously used in the study of the background behaviour are now replaced by the *baseline* and *burstfraction*, which have definitions slightly different from, respectively, the "continuous component" and the "bioluminescence activity".
The *baseline* is defined as the median of consecutive samples of background rate values, each sample being evaluated as the average over 20 consecutive frames[16] to reduce the quantization effect due to the precount. The calculation of the median is performed over periods of 15 minutes, i.e. on a sample of about $7 \cdot 10^4$ frames.
Test 1.12, which shows very high rates for the continuous component as well, underlines the limits of the definition of bioluminescence activity used in previous measurements: if the base-line is near $200\ kHz$, using this old definition a larger portion of each peak that emerges over the continuous component would be counted as biological activity, thus incorrectly increasing the fraction of time taken by bursts. Moreover, since the continuous component and the burst activity values are correlated, the introduction of a new variable was needed to separate more efficiently the different background contributions.
For this reason we define now as *burst fraction* the fraction of time within the considered period, in which the average rate exceeds by at least 20% the baseline value. This quantity is strictly connected with the highly variable contribution of bioluminescence spikes, in contrast with the baseline which mainly reflects the behaviour of the ^{40}K and of the bioluminescence continuous component.
The LCMs will here be numbered from 1 to 5, with increasing numbers corresponding to increasing depth. Only one ARS per OM is able to generate CRM events, and they are labeled 0, 2 and 4 respectively for OM 1, 2 and 3.

In figure 4.10 the time evolution over the entire period of baseline and burst

[16] We recall here, as already mentioned in section 3.2.1, that a frame contains data collected in each $13.1072\ ms$ time span and the precount is the unit of measure chosen for counting the events.

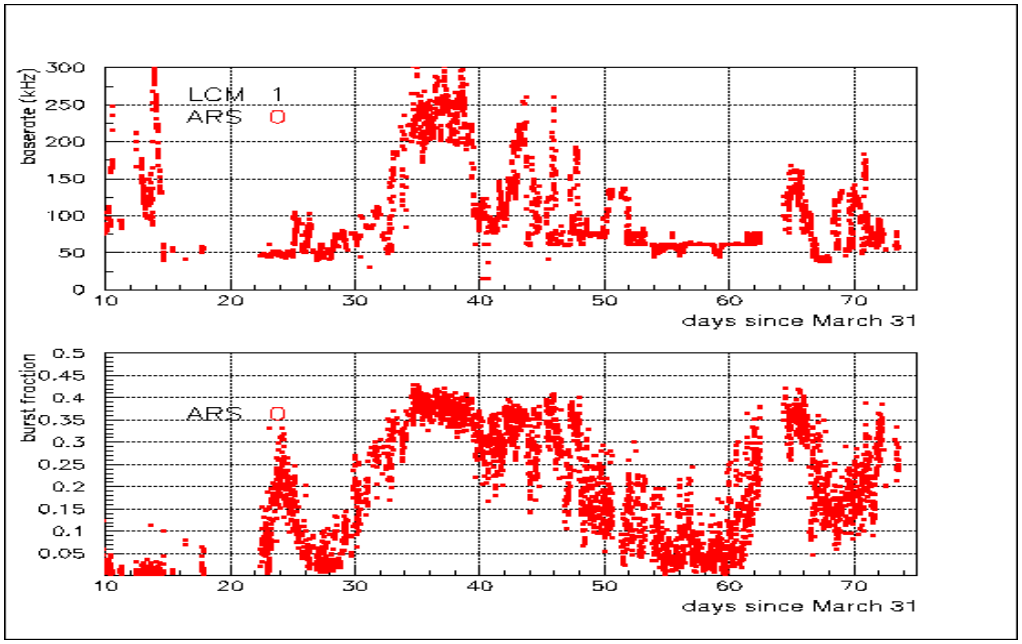

Figure 4.10: Time evolutions of Baseline (top) and Burstfraction (bottom) for LCM 1, ARS 0 from the Prototype Sector Line.

fraction is shown for a single optical module; no remarkable differences have been noticed in the behaviour of different OMs at the same time. Surprising behaviours are registered at the beginning of April and in the second week of May: the baseline rate is extremely high with respect to the general trend of $50 \div 70\ kHz$, often higher than $250\ kHz$. Moreover, while in May this could be explained with the huge increase of bioluminescence activity, in April the burst fraction is unexpectedly low. This high baserate is again another indication that a continuous bioluminescent component has to be considered together with the $30\ kHz$ contribution from ^{40}K.

The high background rate, whatever its origin, is an unexpected problem for the ANTARES experiment because it will lead to a dead time higher than foreseen at the detector design stage. A deeper understanding of the background seasonal variations is, therefore, useful.
The study of correlations between burst fraction and water current speed and direction for the entire operating period has been made impossible by the MIL failure. However, some indirect information on the current speed has been deduced

from measurements of the string inclination. When the zenith angle of the string was appreciable, the orientation of the inclination could be measured with reasonable errors[17].

During high activity periods, the identification of a definite direction of light emission from the relative light intensities registered by the different OMs of a given storey has also been possible. The computed N-S and E-W light asymmetries are shown in figure 4.12. Some periods of intense light emission from a definite direction can be identified. From a comparison of single LCM results in figures 4.11 and 4.12, it appears that the largest asymmetries occur when the largest tilt angles are recorded. Unfortunately, the errors on tilt direction are too large for data within the period of interest, hence no direct check of collimation of light and current directions can be made. However, a comparison of the light direction asymmetries computed in figure 4.12 with previous measurements of water current (see for example figure 4.7) shows that the light direction is parallel to the average current direction at the ANTARES site. These results support the idea that bioluminescence takes place around the string because of the turbulence produced by sea currents.

The analysis presented in detail in the following sections concerns the PSL data and is focused on the last two weeks of data taking. Since June 26, in fact, the trigger rate has been measured not only using the CRM counter, but also in a new way which turned out to be not-redundant: the FPGA-software was modified in order to keep also directly the number of L0 triggers in a frame[18], without a precount structure. The differences in data manipulation in the ARS chip and in the FPGA have also produced other advantages, as will be further explained in the next section. The data sample ideally includes runs $1647 \div 1682$, $4332 \div 4344$ and $9214 \div 9232$ (from June 26 to July 9), however several corrupted or empty files belong to this sample. Besides, some other runs are useless because the data acquisition lasted too little (less than 15 minutes, which is the minimal data sample used to evaluate baseline and burstfraction). The whole data sample then corresponds to about 200 hours altogether: 785 $15'$-samples for OMs in LCM 5, slightly less for the other OMs which were sometimes switched off.

As already mentioned, the MIL had serious problems which hampered the monitoring of the environmental parameters (water optical properties, salinity, temperature, current speed and direction) during the PSL operating period. The re-deployment of the old test line at the end of June partially remedied the failure,

[17]The error on the direction of tilt is about 40^o for a tilt of 0.3^o.

[18]Stored in the variable `nbItemsOrg`. See section 3.2.1.

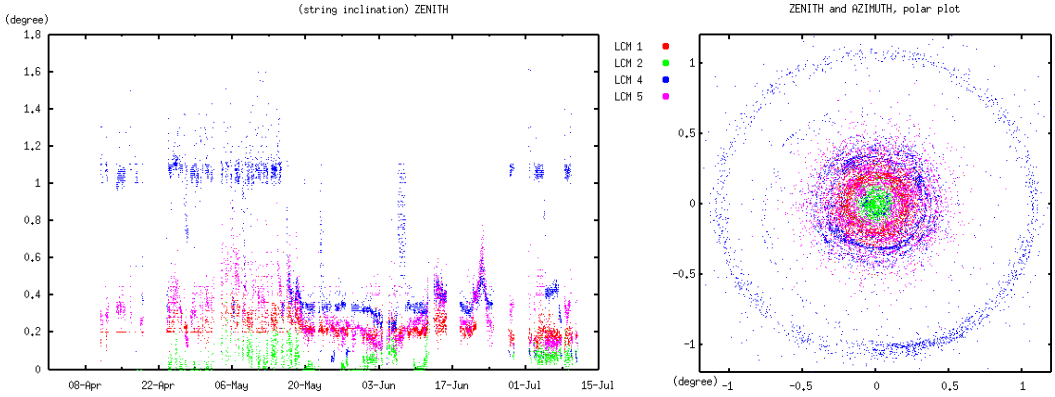

Figure 4.11: *Left:* zenith inclination of the PSL string as a function of time. Rigth: polar plot of the absolute inclination direction. Right is North, Top is West, the distance of the point from the origin corresponds to the zenith inclination angle (in degrees). Different colours correspond to different storeys, as shown by the LCM labels in the figure.

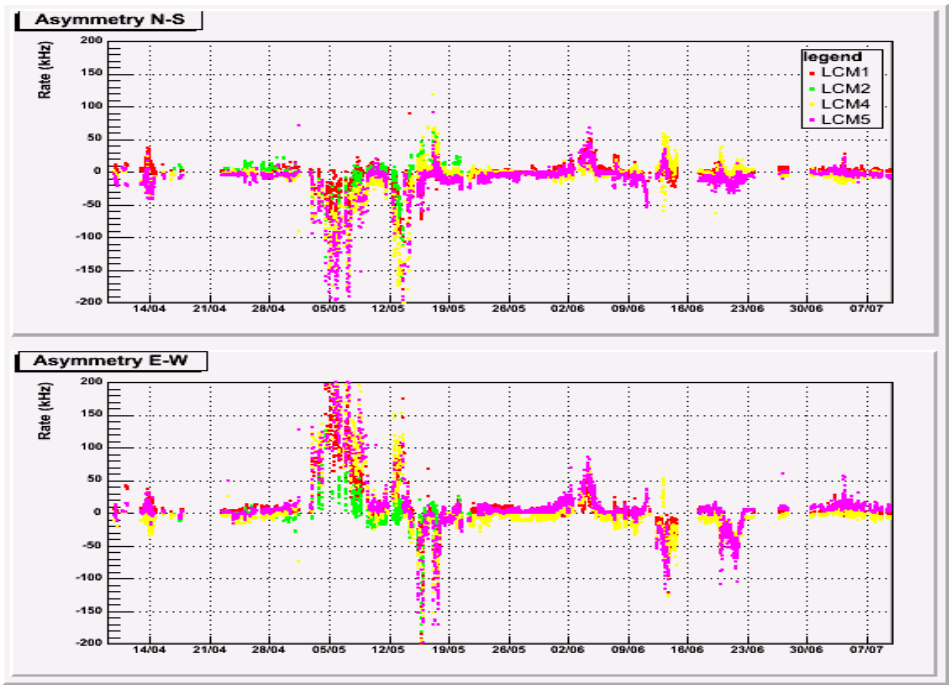

Figure 4.12: North-South (top) and East-West (bottom) rate asymmetries as functions of time.

supplying information on the current for almost two weeks and two $15'$-samples of background rate to be compared with the PSL results.

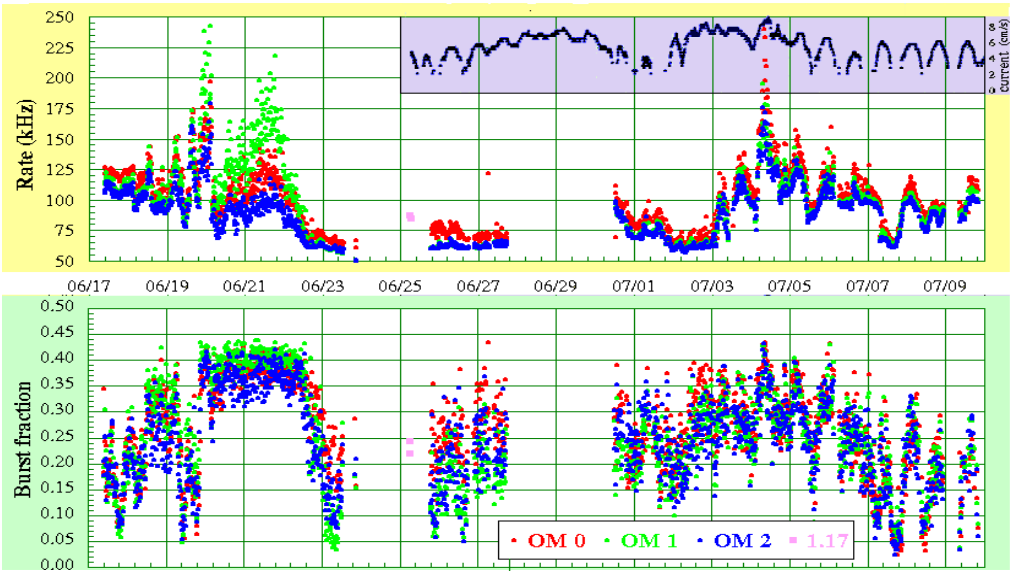

Figure 4.13: Results from test 1.17 and comparison with PSL data in the same period. The only two set of values obtained from test 1.17 are the pink points on June 25. Current measurement vs time are shown as an inset in the baseline plot. [35]

Even though, unfortunately, the PSL was not taking data when test 1.17 did, the baseline and burstfraction values obtained are not incompatible with the results provided by the PSL in the previous and following hours (see the two points in pink in figure 4.13).

Far more worthy and interesting have been the results on the correlation between background and current: comparing the current speed and the burst fraction time evolutions, a strong correlation is evident. As shown in figure 4.13, the measured rates follow the periodic behaviour of the current due to the Coriolis effect (see section 4.1.3) and the same oscillation is visible in the burst fraction data.

4.3 CRM and L0

A CRM event has been treated in the PSL as a SPE event, hence the format was the same (6 bytes) though one byte was set to zero. The events were stored in an intermediate 16-bytes buffer which was then transferred to the CPU memory only

when full (see figure 3.11). At the beginning of a new time slice everything was cleared, so the events in a buffer which was not completely full (and often also the previous event, if it was truncated in the last filled buffer) were lost. As a result, depending on the precount setting, some preferred values for the rate appear in data.

It is important to remember that the problem does not affect the standard DAQ of the ANTARES experiment. When the clock works, in fact, the buffer is continuously read at eack clock cycle. Moreover, without the clock failure there would not have been the necessity of using self-generating CRM events instead of the clock-triggered SPE data.

As an example, table 4.1 shows the results of setting the precount to `pc`=50, which was the preferred value in the last two weeks of acquisition. The problem is

true rate: min (kHz)	3.8	7.6	11.4	15.2	19.1	22.9	...	1144.4	1148.2
true rate: max (kHz)	7.6	11.4	15.2	19.1	22.9	26.7	...	1148.2	1152.0
CRM	1	2	3	4	5	6	...	300	301
bytes	6	12	18	24	30	36	...	1800	1806
buffers sent	0	0	1	1	1	2	...	112	112
`nbItems`	0	0	2	2	2	5	...	298	298
rate loss (kHz)	3.8	7.6	3.8	7.6	11.4	3.8	...	7.6	11.4
measured rate (kHz)	0.0	0.0	7.6	7.6	7.6	19.1	...	1136.8	1136.8

Table 4.1: True rate and rate loss, taking into account the buffering problem of CRM events. Precount set to 50.

more acute for high precount values and is significant also at high rates, though the fraction of data lost is comparably small. The quantization resulting from precount and buffering affects the baseline calculation, because all the tiny fluctuations are removed and preferential values appear. If the computed baseline is lower than the true one, a larger number of the points above the chosen cut[19] will be considered as bursts, thus even in a stable situation one obtains a large number of "bursts". The fact that computations of baseline are performed by cumulating several time slices does not change the previous conclusion if the burst fraction is computed on the basis of individual time slices. The obvious solution of reducing the precount value is not applicable because of the high dead time which affects the CRM: the time needed to "read" an event has been estimated to be about $5\ \mu s$, hence a significant fraction of counts would be lost if the precount were set to very small

[19] 20% or 5σ above the baseline: see below.

values. A saturation rate around $1 \cdot (5\ \mu s)^{-1} = 200\ kHz$ is expected when the precount is set to 1, and analogously for a precount equal to 10 (saturation at $\approx 2\ MHz$) or 50 (saturation at $\approx 10\ MHz$). These are not incompatible with the experimental evidence discussed below.

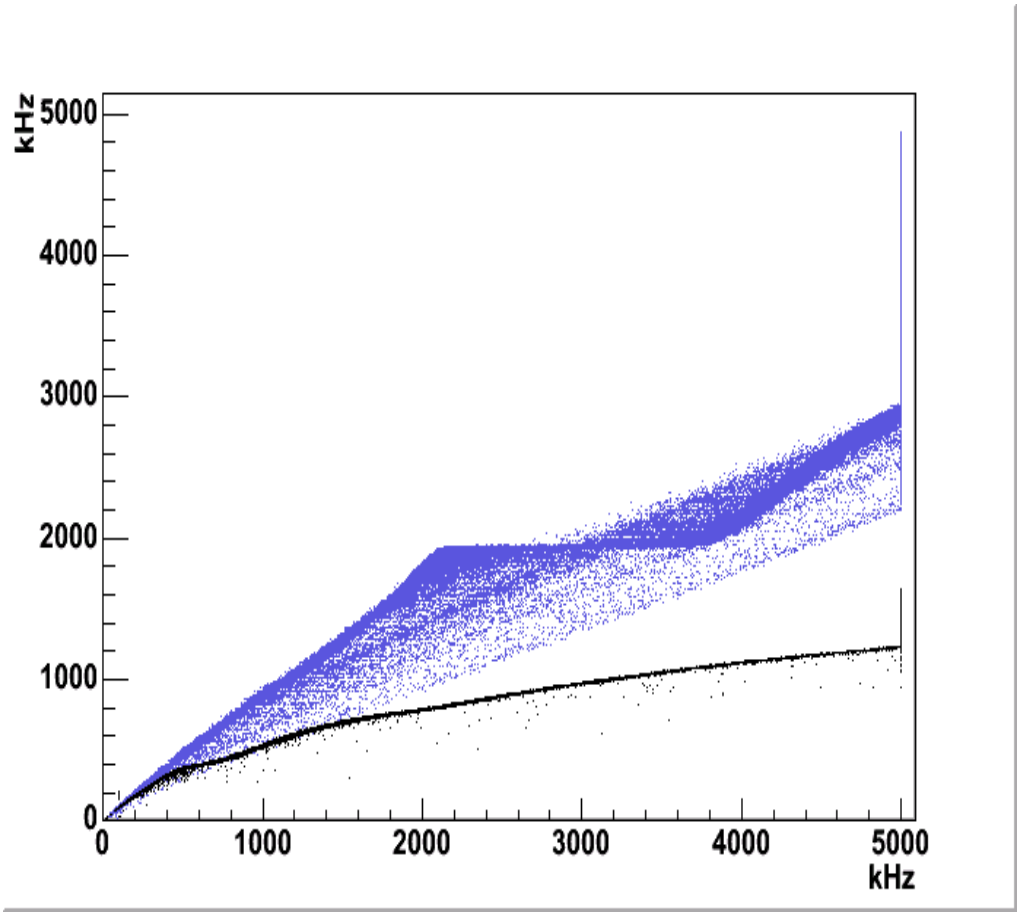

Figure 4.14: CRM vs L0 rates for LCM 5 ARS 0. Data with different CRM-precount values are shown in different colours: purple is 50, black is 10.

The awareness of these problems led to the decision of introducing another counter to perform cross checks. The number of L0-triggers has also been counted directly by the FPGA[20], stored as a 2-Byte word, and referred to as the variable `nbItemsOrg`. While the high dead time in CRM events is the cause of

[20]No intermediate buffering is present, and the dead time is negligible.

`nbItems` saturation far before the 2-Byte size becomes a problem, this is not the case for the raw L0-trigger counts, which is about a factor `pc`=precount greater than CRM counts[21] and could then easily exceed the maximum value $2^{16} - 1 = 65535$. This results in a saturation rate of $\approx 5\ MHz$ for the L0 counter, as shown in figure 4.14.

This same plot confirms the CRM saturation problem mentioned above and shows also an unexpected (and not yet understood) feature of CRM events. Besides the expected deviation from linearity[22] due to the dead time affecting CRM events, some preferential rates can be identified, corresponding to values of `nbItems` around $2^9,\ 2^{10}$ and so on. In the scatter plot, for CRM data with precount equal to

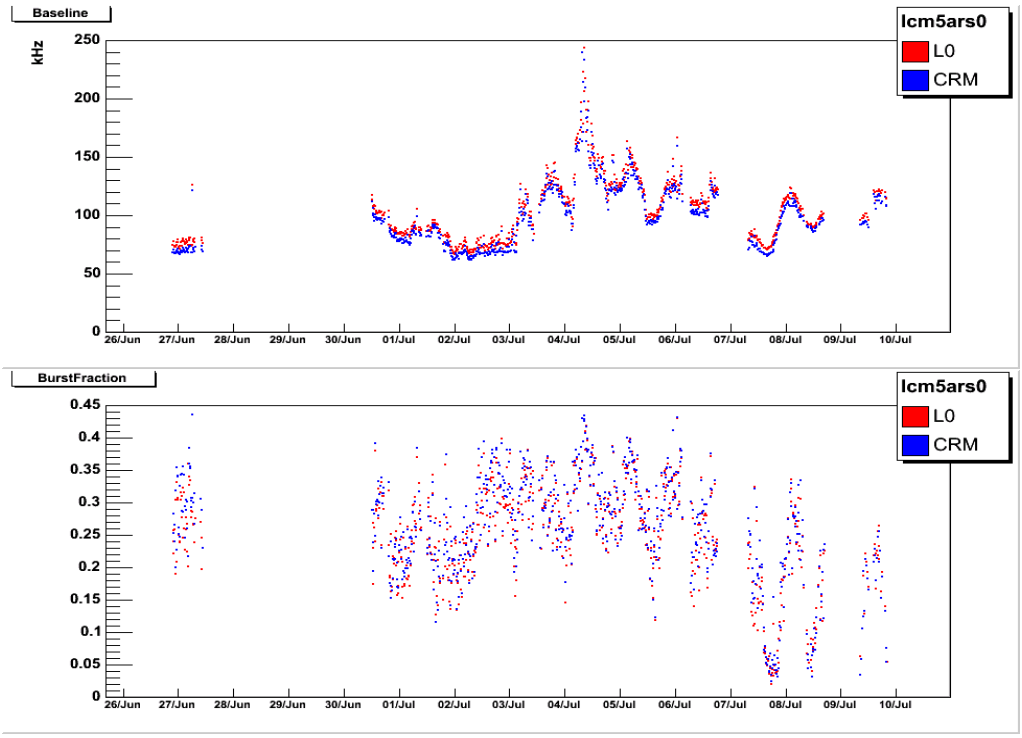

Figure 4.15: Baseline (top) and BurstFraction (bottom) vs Time. Both CRM and L0 data from LCM 5 ARS 0 are used.

50 only the flat zone due to `nbItems` around 2^9 is visible ($\approx 1950\ kHz$) since the following steps are hidden by the L0 saturation. Data with the precount equal

[21] It should be ideally a CRM event with precount set to 1 and without the buffering problem.

[22] (CRM·pc) vs L0 should be characterized by a coefficient around unity for high rates.

to 10 show also the second step, though both[23] are less visible since the entire curve is “flattened” by the dead time problem.

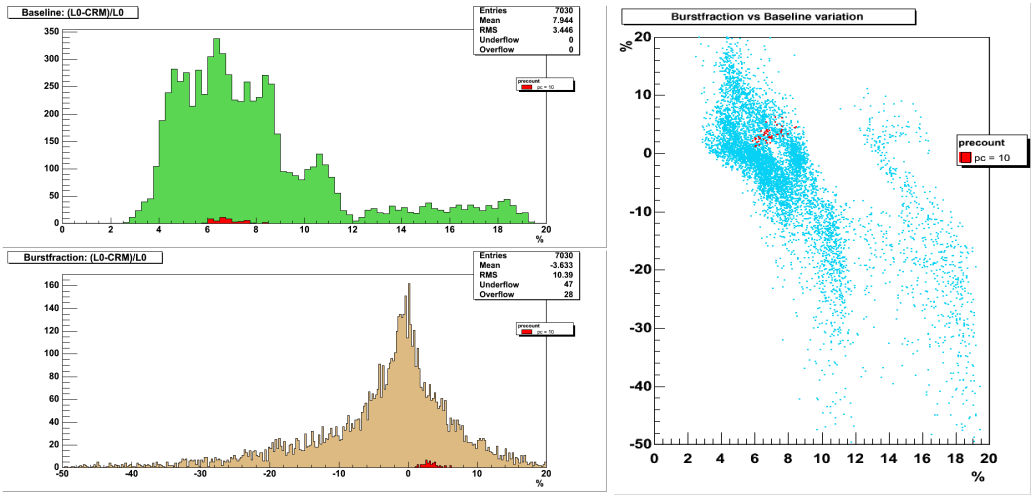

Figure 4.16: Top left: distribution of differences (in $\%$) between baseline values obtained using L0 and CRM. Bottom left: distribution of differences (in $\%$) betwen burstfraction values obtained using L0 and CRM. *Right:* correlation between percentage difference in burstfraction and percentage difference in baseline. Precount set to 50 or 10 trigger counts.

Figures 4.15 and 4.16 highlight the results on baseline (BL) and burstfraction (BF) values obtained using L0 rather than CRM events. The values obtained using the CRM are lower than the ones obtained using L0 by up to $10\ kHz$ in absolute value and by up to 20% in percentage. Moreover, as the scatter plot of figure 4.16 shows, for small (≈ 3) BL differences in percent, positive BF percentage differences are found, while for larger BL differences the corresponding difference in BF becomes negative and eventually large in absolute value.

In summary, the analysis shows that the L0 data are preferable for the study of background. They are absolutely necessary when a thorough characterization of single bioluminescence peaks is needed. From now on, hence, the L0 data sample will be the only one used.

In figure 4.17 is shown the time dependence of the baseline for all OMs for which L0 data are available. It can be noted, as it was already evident in the CRM data, that no noticeable difference appears in the time dependence of the trigger rates recorded by the single OMs, but for an overall relative scale factor between

[23] At about $390\ kHz$ and $780\ kHz$.

them. From now on, therefore, the data will be analyzed without distinction between different OMs.

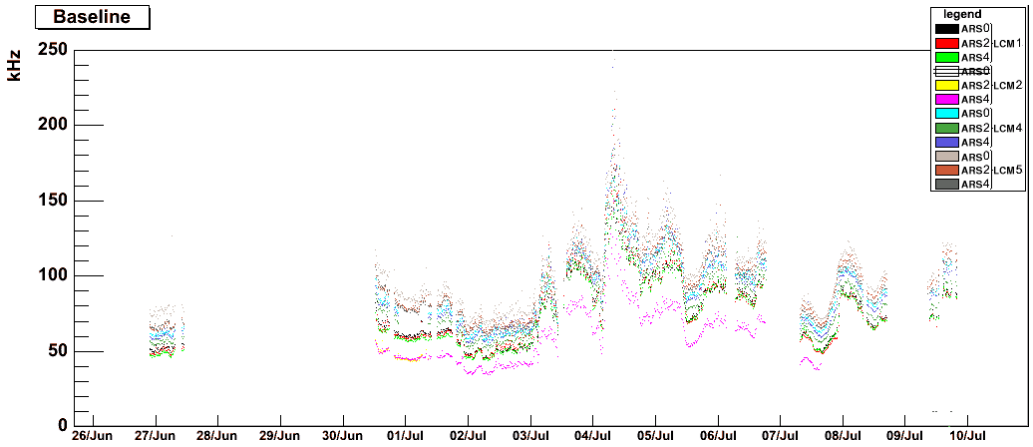

Figure 4.17: L0-Baseline for all the OMs.

4.4 Burst analysis

Although no direct information on the characteristics of bioluminescence at the ANTARES site is available in the literature, some information may be obtained by extrapolating from what is known about the fauna at different depths or different sites. It is likely, for example, that the dinoflagellates, very common bioluminescent species in the sea, are abundant also around the detector; hence, most bursts should show those characteristics which are peculiar to such species: a time duration of about $200\ ms$ and a total yield around 10^8 photons.

A set of routines has been developed to locate bursts in the raw data, to define their characteristics and to fit them to definite mathematical expressions.

To search for bursts, the software scans sequentially the raw data looking for a rate larger than a *threshold* defined as the baseline plus 5σ, where σ is the Poissonian baseline fluctuation[24]. The corresponding frame marks the beginning of a burst. The end is taken as the last frame in the sequence where the rate is still larger than the above threshold. The variables used in the present analysis to characterize a burst are shown in figure 4.18.

[24]That is `Nbitems` or `NbitemsOrg` $> 5\sqrt{N} + N$, where N is the median number of counts in a frame-time: $N =$baseline$(kHz) \cdot 13.1072\ ms$

The maximum resolution one may achieve in defining the time duration of a burst is equal to the frame-time duration. It is not possible to analyze bursts shorter than this. Anyway we know that a bioluminescent flash lasts for at least tens of ms. We are, therefore, sure that no inner structure could appear on a shorter time-scale. Burst Duration, Time to Maximum and Time after Maximum

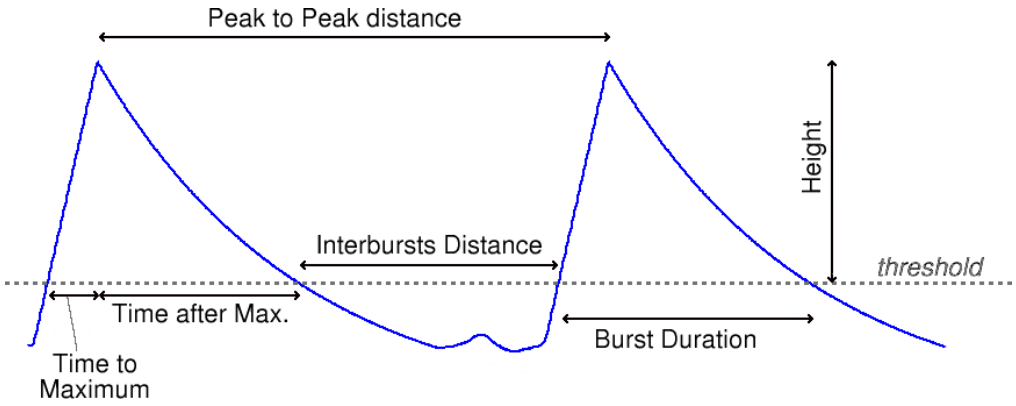

Figure 4.18: Schematic summary of definitions of quantities characterizing a burst.

cannot extend to times longer than $\approx 6\ s$, since, for technical reasons, a maximum value had to be chosen for the number of frames constituting a burst. As a result, the average values of the distributions of these quantities are smaller than the true ones, although not by large amounts: the fraction of events above this cutoff is negligible with respect to the total.

The burst height could be defined in another (maybe more appropriate) way, i.e. relatively to the baseline rather than to the threshold value. The difference between these two values is just an offset depending only on the baseline rate, hence results using the two definitions are comparable to some extent. On the opposite, a definition referred to the baseline is not equally usable for the burst duration: the overlap between consecutive bursts makes the beginning and end of a burst not clearly defined at the baseline level. In order to be coherent and to avoid artificial results when looking at correlations among variables, therefore, the entire analysis presented will use the threshold as a reference, in computing the burst height as well as all the remaining variables characterizing a burst.

4.4.1 Raw burst analysis

Most of the information is obtained from the raw distributions. As already anticipated, the present analysis has been carried out putting together the information available from all the optical modules in the PSL that were not affected by problems additional to the clock failure (11 OMs at all). The only cut applied to the data in this section is that of a low burst fraction (less than 0.22), which improves the efficiency of the algorithm, reducing the probability of overlap between consecutive bursts. The choice of this value is based on the analysis of correlations between burst fraction and number of bursts, as will be explained below.

Statistics shown on the plots are the ones automatically computed by ROOT by using the binned histograms, without taking into account overflows and underflows. Statistics computed directly from data will be always shown in the captions.

Figure 4.19 shows the Burst Duration and the Burst Height distributions. From these histograms we see that fast (less than $200\ ms$) and not very intense (less than $100\ kHz$) bursts constitute the major part of the background. The peak which appears around $5\ MHz$ in the burst height distribution is the obvious consequence of the L0-saturation at $4999.92\ kHz$.

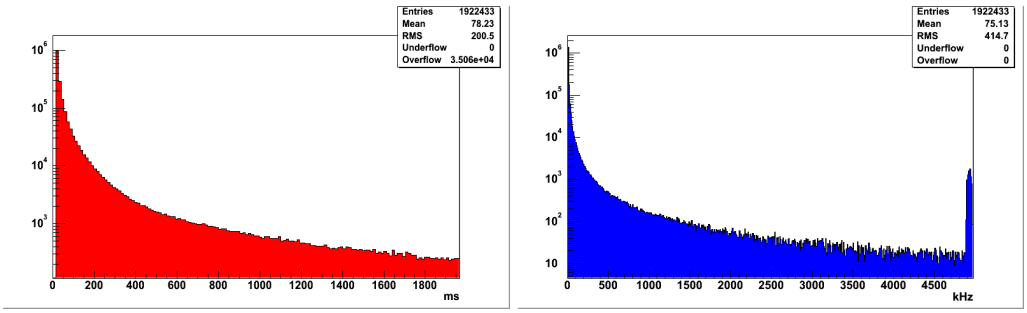

Figure 4.19: *Left:* Burst Duration. Mean value is $147\ ms$, RMS is $572\ ms$. *Right:* Burst Height. Mean value is $75\ kHz$, RMS is $413\ kHz$.

An attempt to fit the distribution of Burst Duration with simple analytic functions has been made, but with no encouraging results. Some improvement is obtained using the superposition of at least three exponentials. However the variety of bioluminescent species is probably too large to allow identification of the individual contributions in the global histogram: fitting the distribution with the sum of tens of different functions would not provide much insight.

Figure 4.20 shows the distribution of the Burst Scale Factor, i.e. the ratio between Height and Duration. The peaks in the light-blue histogram in the figure

are due to both the L0-saturation and time discretization: the excess of events occurrs, in fact, in correspondence of $\frac{4999.92\ kHz}{(13.1072\ ms)\cdot\ n}$, i.e. consists of those bursts of any (discretized) length but of height equal to the maximum allowed. The ratio between burst height and burst duration being not constant leads to the conclusion that the spread in values for the distributions in figure 4.19 is mainly due to the presence of different burst shapes rather than to a variety of distances between a source with definite characteristics and the PMT.

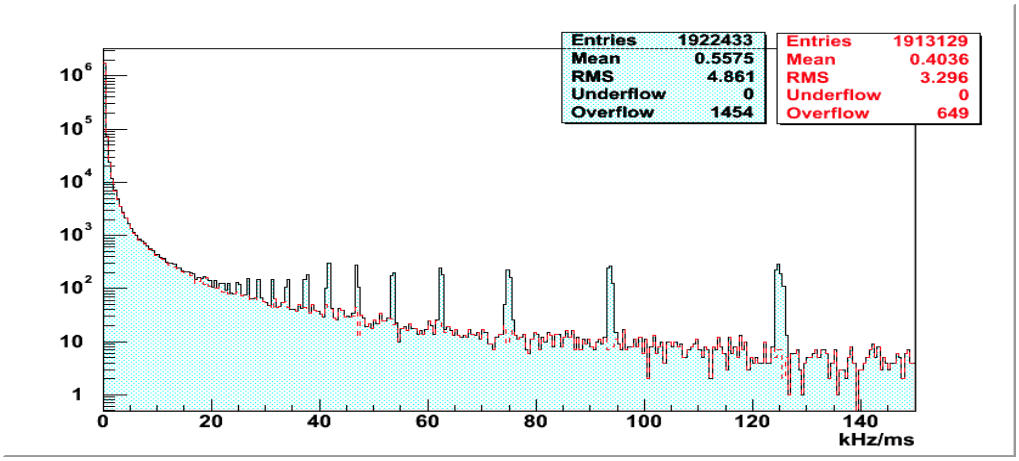

Figure 4.20: Burst Scale Factor. Mean value is $0.8\ kHz/ms$, RMS is $9\ kHz/ms$. Further cut for the dotted red histogram: Height$< 4875\ kHz$

As already observed, the effect of defining burst quantities referring to a threshold (called *threshold effect* from now on) is a decrease of Burst Height, Duration, Time to Maximum and after Maximum with respect to the "real" values obtainable when use is made of the baseline offset as a reference. These variations affect in a quantitevely different way each variable, leading to a distortion of the distribution of the above variables. The distortion, at a fixed threshold level, is dependent upon the height of the burst above the baseline. A simulation which assumes a fixed burst shape[25] and varies the distance between the source and the OM[26] was able to roughly reproduce the shape of the distribution of figure 4.20. However the simulation also shows that the threshold effect is inadequate to explain the long

[25] See analitic function in 4.1.

[26] Hence varies the number of photons reaching the PMT, i.e. the burst height over the the baseline.

tail in the distribution: once the parameters of the function have been fixed, the minimum and maximum apparent Scale Factors are univocally determined in the simulation and they differ by a few tens of kHz/ms at most.

An old simulation of the background, introduced at the ARS digitization level in the Software Trigger Simulation, represented a bioluminescence burst as a linear rise followed by a flat top at saturation and an exponential decay. The typical rise/fall times of the flash were supposed to be long[27] compared to the frame duration, justifying an approximately constant rate during each frame. Hence the background was generated accordingly.
In figure 4.21 are shown the distributions for the Time to Maximum and the Time after Maximum. These highlight that the approximations used in the simulation just mentioned are not justified: the time constants of bursts are on average very short and the median value of the distributions are even shorter. A possible new description of bioluminescence bursts in a precise trigger simulation should take this information into account.

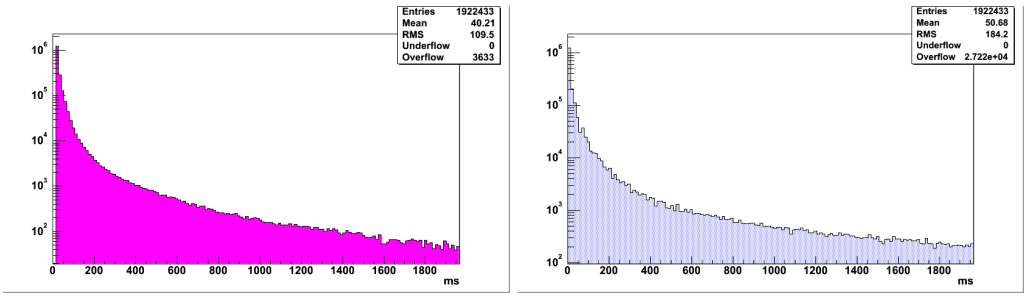

Figure 4.21: *Left:* Time to Maximum. Mean value is $46\ ms$, RMS is $177\ ms$. *Right:* Time after Maximum. Mean value is $101\ ms$, RMS is $475\ ms$.

The inter-burst distance (IBD) is defined as the time delay between the end of a burst and the beginning of the following one. Its distribution is displayed in figure 4.22-left.
If we compare the distribution of Burst Duration (figure 4.19-left) with that of IBD (figure 4.22-left) we notice that the former has a considerably smaller mean value. This reflects the fact that the fraction of events at very small values of Burst Duration is much larger than for IBD, or else the tail of this second distribution is longer. In other words, larger distances between bursts are more likely than long bursts. From a biological point of view this could naively be explained considering

[27] By an order of magnitude.

that bioluminescent emission cannot last for long periods, but on the other hand, no such limitation is present on the interval between consecutive emissions.

A different way of defining the distance between consecutive bursts is given by the time delay between the peak[28] of two consecutive bursts (figure 4.22-right). The ”peak to peak” (P2P) distance reflects however the combined effect of delay between bursts and burst length. The excess in the first bin noticed in the previous distribution is here spread out over several bins because of the different possible lengths of bursts, for a fixed distance between consecutive bursts.

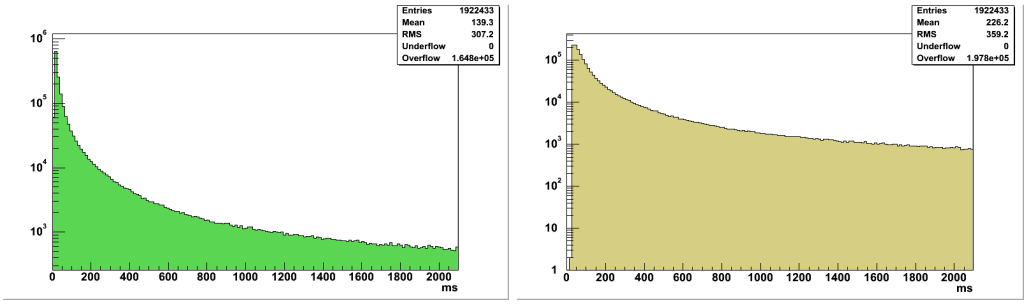

Figure 4.22: *Left:* Distance between consecutive Bursts (IBD). Mean value is $918\ ms$, RMS is $12432\ ms$. *Right:* Peak to Peak distance. Mean value is $1069\ ms$, RMS is $12452\ ms$. Observe the different range of the logarithmic scale, due to the lack of events in the first bins.

We have next analysed correlations of all the variables characterizing a burst with baseline or burst fraction (both used as x-axis variables). Profile histograms are used to visualize the average trend.

Results which do not bring significant information, like the correlations with BL[29], or which are redundant, like the correlations with Time after Maximum[30], are not shown.

An analysis of correlations between number of bursts and BF, together with that between IBD and BF, suggests[31] evidence for a failure of the algorithm in separating overlapped consecutive bursts. As figure 4.23-left shows, the number of bursts increases only up to values of BF around 0.22; at larger BF values the

[28]The *peak* is where the burst reaches its maximum rate for the first time.

[29]Which show no correlations.

[30]Which are equally deducible from the correlations with Duration and Time to Maximum.

[31]It could not be superfluous to underline that the deductions in the following are based on the hypothesis that a higher burst fraction means a higher number of bursts, a different time duration of them. This idea is anyway well consistent with all data results.

effect of burst overlap causes a flattening and then a decrease in the distribution. This is consistent with what can be seen in the right part af the same figure: increasing the BF, the IBD first decreases, as it should, but then it flattens out at BF $0.20 \div 0.25$.

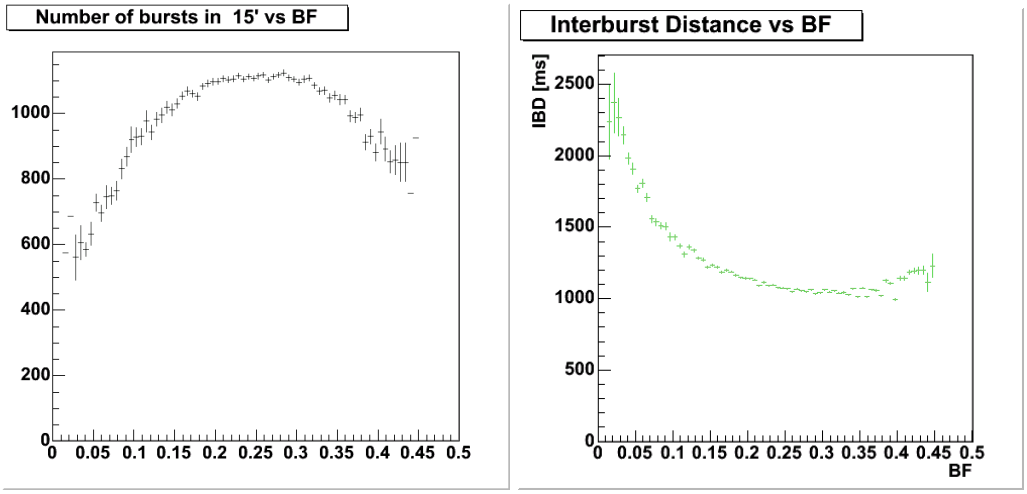

Figure 4.23: *Left:* Profile histogram of Number of bursts vs BF. *Right:* Profile histogram of Inter-bursts Distance vs BF.

In figure 4.24 correlation plots of Burst Duration and Height vs BF are shown.

We see that Burst Duration increases on average as a function of BF, in an almost linear way up to BF values of ≈ 0.3, but a sudden change in the rate of increase occurs for larger BF values. This may again be explained as a result of burst overlap.

A similar conclusion may be drawn from an inspection of the dependence of Burst Height (and of Time to Maximum or after Maximum, not shown) upon BF, shown on the right in the same figure.

The observation of this effect is what has led to the decision of applying a cut at 0.22 on BF in order to select only really isolated bursts.

The resulting scatter plots (figure 4.25) of average[32] Burst Height and of average Burst Time to Maximum vs Burst Duration exhibit a clear trend: the time to

[32] Nothing could be seen directly from the scatter plots: because of the asymmetric shape of all the distributions, the plots present high densities of points at small values of all the variables and tails along the axes (large values for two variables at the same time are unlikely). Therefore, correlations between burst quantites presented below are not evaluated using individual bursts but burst variables averaged over a fixed time interval. The natural choice has been the same 15' interval in which BL and BF are defined.

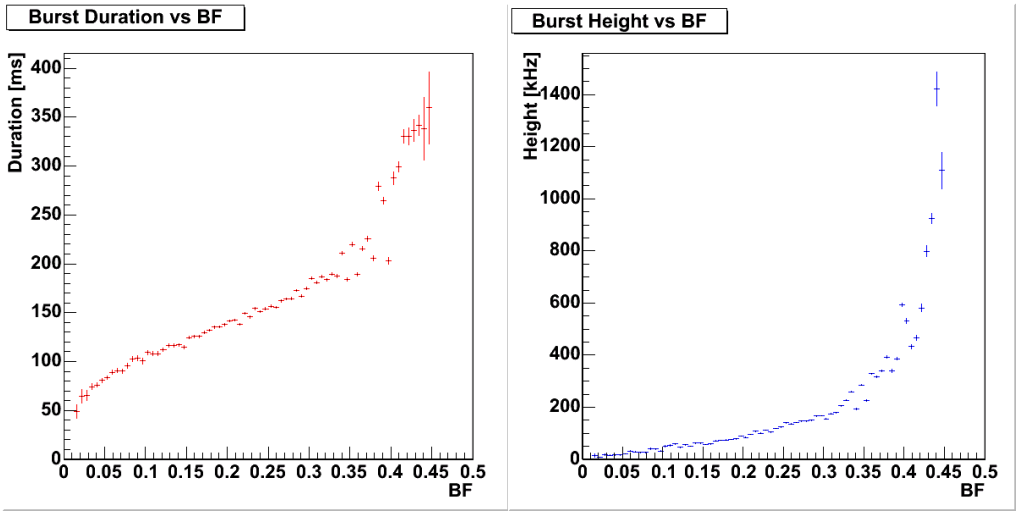

Figure 4.24: *Left:* Profile histogram of Burst Duration vs BF. *Right:* Profile histogram of Burst Heigth vs BF.

reach the maximum and the maximum rate reached increase proportionally to the burst duration. Hence one could imagine that, among all the possible shapes, one type of burst occurs more often and that the parameters which change when moving along the correlation line may be either the already mentioned *threshold effect* or the different light yield from different species, or a combination of both[33].

4.4.2 Analysis on fitted bursts

The results of the previous analysis led us to improve our understanding of bursts (for biological interest as well as physics purposes) trying to define burst shapes and characteristics.

Although several functions (e.g. gaussian, exponential rise and decay, landau) have been tested, the faster and best performing[34] fitting procedure makes use of a function already widely diffuse in biology and within the ANTARES experiment itself [24, 39, 40]: a continuous function consisting of two parts, a linear

With the purpose of making the average a sensible quantity, a cut on bursts has been applied excluding those averages performed on samples having a limited (≤ 5) number of bursts.

[33] And maybe some residual effect of burst overlap may still be present.

[34] The choice of the function finally used has been made by comparing the number of burst rejected by the procedure before 20 bursts are successfully fitted with a renormalized χ^2 smaller than 500.

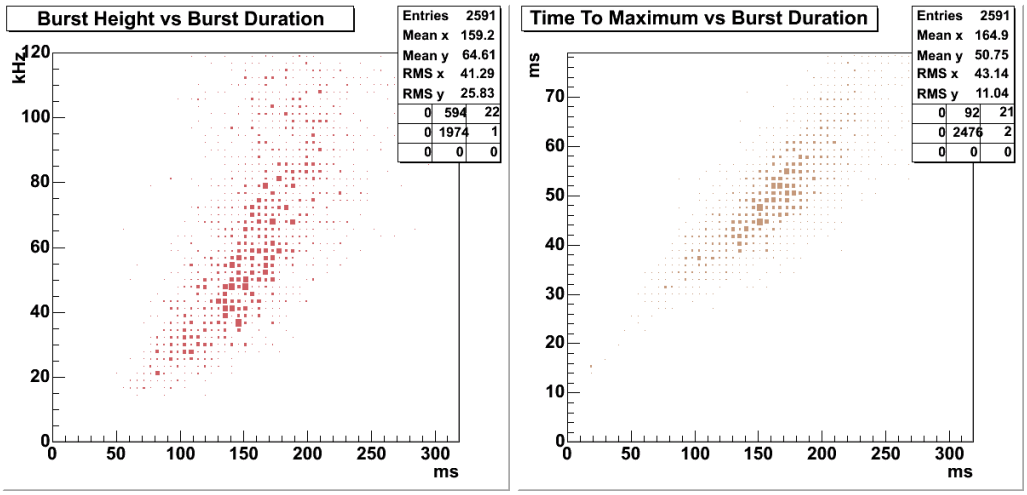

Figure 4.25: *Left:* Average Height vs average Duration scatter plot. *Right:* Average Time to Maximum vs average Duration scatter plot.

rise followed by an exponential decay. Equation 4.1 is the analytical expression implemented in the program. Examples of both a single burst and a double burst fit are shown in figure 4.26.

$$y = A \cdot \theta(x - x_0) \left\{ \theta(x_p - x)(x - x_0) + \theta(x - x_p)(x_p - x_0) \cdot e^{-\frac{x - x_p}{\tau}} \right\} \quad (4.1)$$

The time of the actual beginning of the burst, denoted by x_0, has been introduced to correct a possible misinterpretation by the algorithm: it can only be positive and its maximum value is half frame-time lower than the Time to Maximum computed in the raw data. Other constraints on the parameters are imposed according to their physical meaning. The range of the actual time to reach the peak (x_p) is set in such a way as to have $x_p + x_0 \approx$(Time to Maximum $\pm \frac{13.1072}{2}\ ms$). The slope of the linear rise, corresponding to the parameter A, ranges from 0 to $\frac{5\ MHz}{1\ ms}$. The time constant τ of the decay exponential is allowed to vary from 0 to the entire burst length. The range of the parameters is broader than necessary in order to loosen the bias introduced with the choice of a definite burst shape.

Bursts with a strongly attenuated photon yield cannot provide meaningful information on bioluminescence characteristics. Due to the fact that the bursts stick out of the baseline, the same burst with different attenuation factors would rise above the threshold with different fractions of its entire area: its characteristics

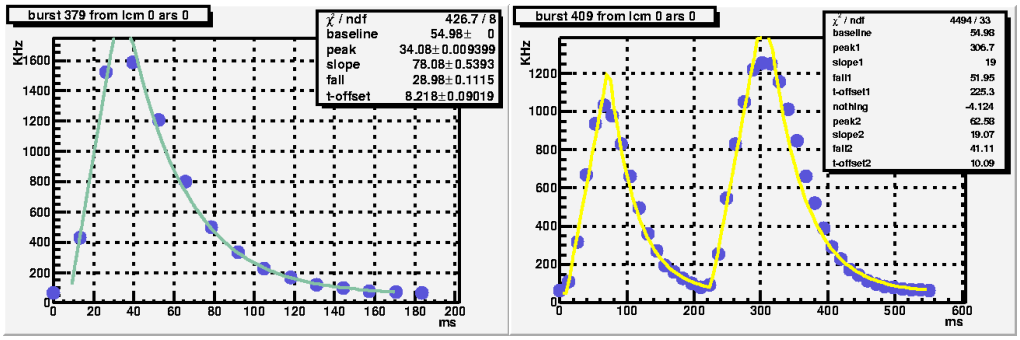

Figure 4.26: Example of single (on the left) and double (on the right) fit. Run 1650 (June 27). The first and last point in the graph show the threshold value (i.e. the maximum rate which could be found in that frame) and are not used as points for the fit.

would hence incorrectly appear different in different instances[35]. For this reason bursts having a low height have been discarded without ever trying to fit them.

The weakest burst visible comes from dinoflagellates: 10^8 photons in $\approx 200\,ms$, with a symmetric wavelength spectrum peaked around $480\ nm$. Since background correlations are found to be weak for separations between OMs larger than $10\ m$ [30], attenuation is supposed to be unimportant at distances of a few meters from the Benthos sphere. An organism 4 meters away will illuminate a cone of $0.002\pi\ sr$, hence assuming an isotropic emission, only 0.05% of the photons will reach the photocathode. Adding the convolution of the PMT quantum efficiency with the emission spectrum and taking the L0-threshold (0.3 p.e.[36]) into account, the total number of counts for each burst will be $\approx 4.1 \cdot 10^4$. The corresponding lower limit[37] on the burst height is $\approx 350\ kHz$,. Therefore, a preliminary cut of bursts with a height lower than $400\ kHz$ seems to be reasonable in order to select only events close to the OM.

After fitting, only those bursts having a normalized χ^2 below 500 were kept.

The possibility of performing a *double fit*, i.e. to use the superposition of two fitting functions with different parameter values (see figure 4.26-right), on what the raw algorithm had recognized as a single burst had also been implemented,

[35] See the other comments about the threshold effect on page 95.

[36] This threshold leads to a loss of the left tail of the 1 p.e. peak and makes no distinction between single- and multi-photon events. The latter are quite abundant because the minimum width of the L0 signal is few tens of nanoseconds, an order of magnitude longer than the average delay between photon arrival times.

[37] The estimate is computed assuming a scalen triangle shape for the burst.

with the hope to increase the statistics by "rescuing" part of bursts made unusable because of overlaps.

However, the double-fit results did not appear satisfactory at a visual inspection, hence the final analysis uses the results of single fits only.

The cut on burstfraction, applied to the raw data, is not necessary in the case of fitted data: the overlap problem is solved, to a large extent, by rejecting bursts with $\chi^2/n.d.f. > 100$.

The number of fitted events available is not large enough to allow an estimate of the efficiency of the fit procedure when bursts start overlapping. However, when the correlation between the average number of bursts and the burst fraction (not shown) is plotted for fitted data, the behaviour seen is almost the same as in figure 4.23: for high BF values, the number of bursts starts decreasing, since bursts distorted by overlaps are rejected by the fit procedure. A confirmation of the latter observation comes from the scatter plot of $\chi^2/n.d.f.$ for single fit vs BF (not shown), from which we find that the average χ^2 doubles at large burst fraction values.

For the parameters A and x_p, a comparison with the quantities, extracted from the raw data, which have an analogous meaning is possible: Height/(Time to Maximum) can be compared with A and Time to Maximum with x_p. In each of the figures 4.27 and 4.28, both raw and fitted data are shown: the same cuts applied before to the raw data are now applied to both the raw data (dark coloured histograms) and the fit data (clear histograms) distributions. As already mentioned, a lower cut on burst height was applied to the raw data before being passed to the fitting procedure. Hence this same cut has been applied to the raw data in the distributions[38] of figures 4.27 and 4.28. The distributions of the fitted variables when only a cut on χ^2 is applied are also shown in the figures, as light coloured histograms.

The compatibility of the distribution shapes is satisfactory at least for $A \geq 20$ in figure 4.27. In figure 4.28 the raw data distribution has a much longer tail, as expected from burst overlap. Both results give robustness to the hypothesis used to choose the fit algorithm: the assumed burst shape is close enough to the real one.

This give us some confidence in the τ parameter distribution, shown in figure 4.29. Three different populations of events are distinguishable, even after applying a tighter cut on χ^2 (though the tail above $600\ ms$ is slightly reduced if $\chi^2/n.o.f. <$

[38]The strange peaks at the beginning of the grey histogram in figure 4.27, occurring around $\frac{400\ kHz}{n \cdot 13.1072}$, are a consequence of this cut.

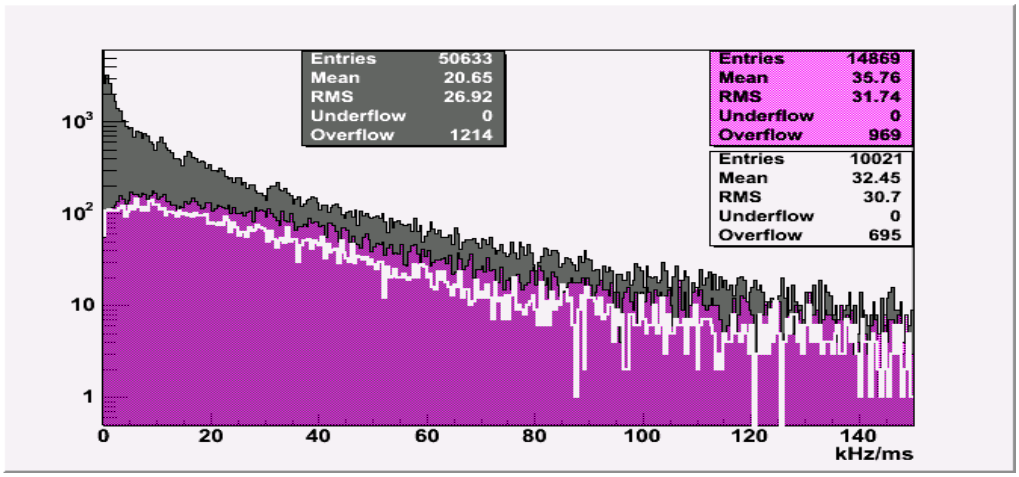

Figure 4.27: The histogram in light-purple gives the distribution of the constant A obtained in the fits when a cut $\chi^2/n.d.f. < 100$ is applied. The clear histogram (white thick line) is the same distribution when a cut on BF and burst height is applied. The grey histogram shows the distribution, obtained from the raw data, of the ratio between Burst Height and Time to Maximum, where a lower ($400\ kHz$) and an upper ($4875\ kHz$, as in figure 4.20)) cut on burst height have been applied together with the cut on BF.

50).

An interesting interpretation may be that burst characteristics for different species have been identified. It is however suspicious that such a definite structure is not equally well identified in the distributions of the other parameters. In figure 4.30 correlation plots are hence built using τ on the x-axis, in order to reach a better understanding of the shape seen in figure 4.29. The plot on the left has x_p on the y-axis, while the one on the right has A.

We notice on both distributions the presence of two different populations. In the scatter plot on the left we see a rich population at small x_p and τ values, well separated from a second one at values of $\tau \simeq 300$, extending to slightly larger x_p values than the first one. A similar separation is noticed in the scatter plot shown on the right.

In figure 4.31, two correlation plots between burst quantities obtained by the fitting algorithm are shown. Three groups of events, each corresponding to a definite range for the τ parameter, are distinguished in the figure using different colours.
In the scatter plot on the left, the correlation between x_p and Duration is shown,

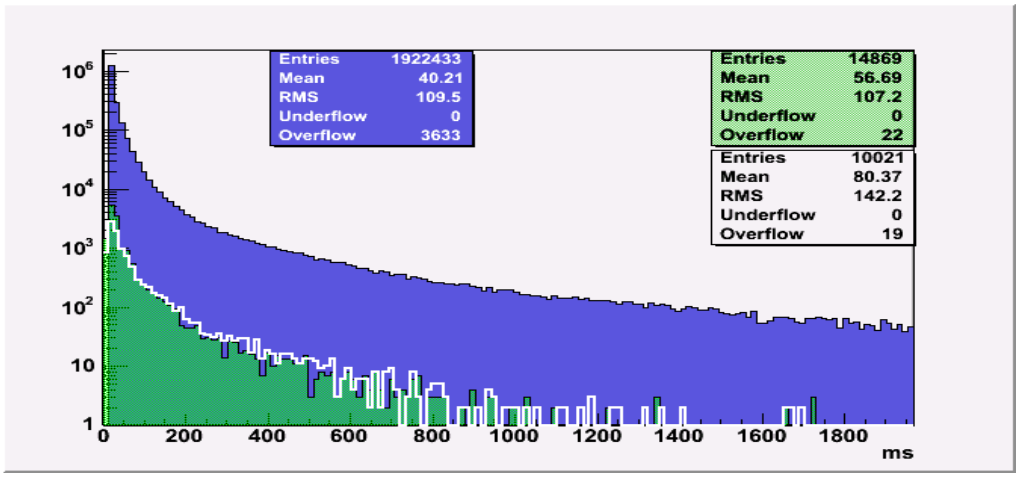

Figure 4.28: The histogram in light-green shows the distribution of the x_p variable obtained in the fits when a cut $\chi^2/n.d.f. < 100$ is applied. The clear histogram (white thick line) is the same distribution when a cut on BF and burst height is applied. The blue histogram shows the distribution for the variable Time to Peak from the raw data when a lower ($400\ kHz$) cut on burst height has been applied together with the cut on BF (notice the difference in statistics in comparison with the grey histogram in figure 4.27).

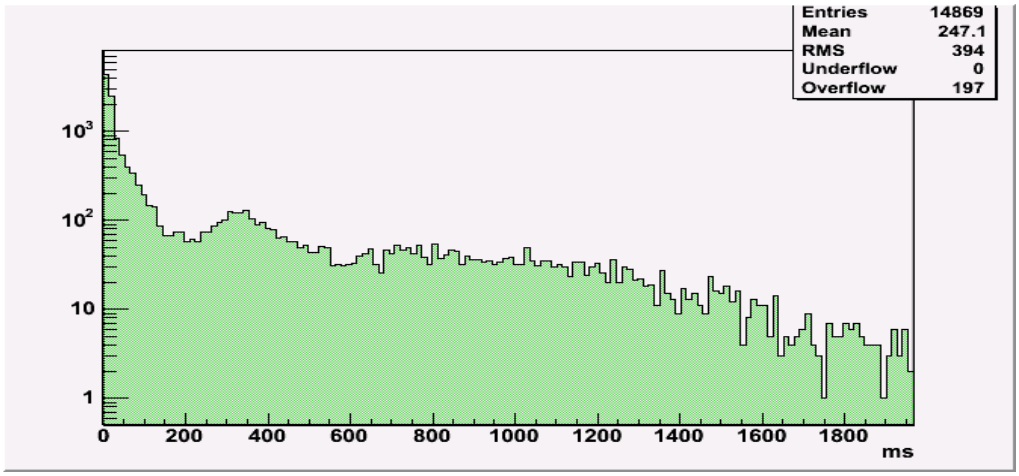

Figure 4.29: τ distribution. Only the standard cut on $\chi^2/n.o.f. < 100$ is here applyied: compare with light-coloured histograms in figures 4.27 and 4.28.

while the one on the right shows the correlation between Height and Burst Inte-

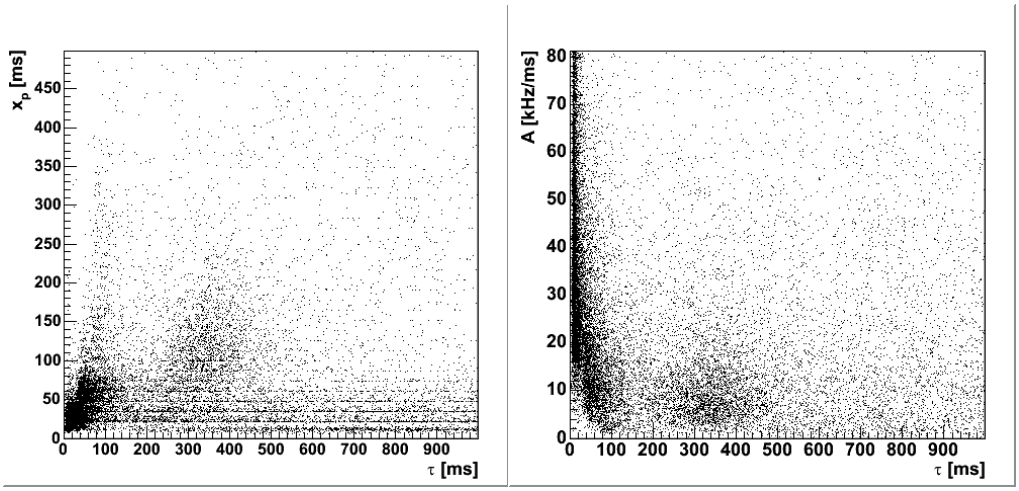

Figure 4.30: *Left:* Scatter plot of x_p vs τ. *Right:* Scatter plot of A vs τ . For both graphs the range on both axes has been zoomed on the zone of interest.

gral[39].
The shift of points towards the right with increasing τ can be explained if one recalls the boundaries imposed on τ during the fit procedure: large values of the decay constant are allowed only for long bursts. The spread in duration, which increases with the one in τ, confirms this consideration. We believe that a large fraction of the blue points are related to poor fits due to burst overlap rather than to a physically different mechanism.

A check of consistency is provided by the integral of the fitted function 4.1 within the burst duration range, which represents the total number of L0 triggers in a bioluminescence event.

The average value approximately corresponds to the lower estimate computed at the beginning of this section, $\approx 5 \cdot 10^4$ counts, supporting the self-consistency of the analysis. The burst height is here computed as the product $A \cdot x_p$. It is again easy to understand the behaviour with increasing τ of the scatter plot in figure 4.31-right: for a definite burst height, larger τ values correspond to longer bursts and hence the integration leads to a higher total L0 rate.

[39]The integral of the fit function: see below.

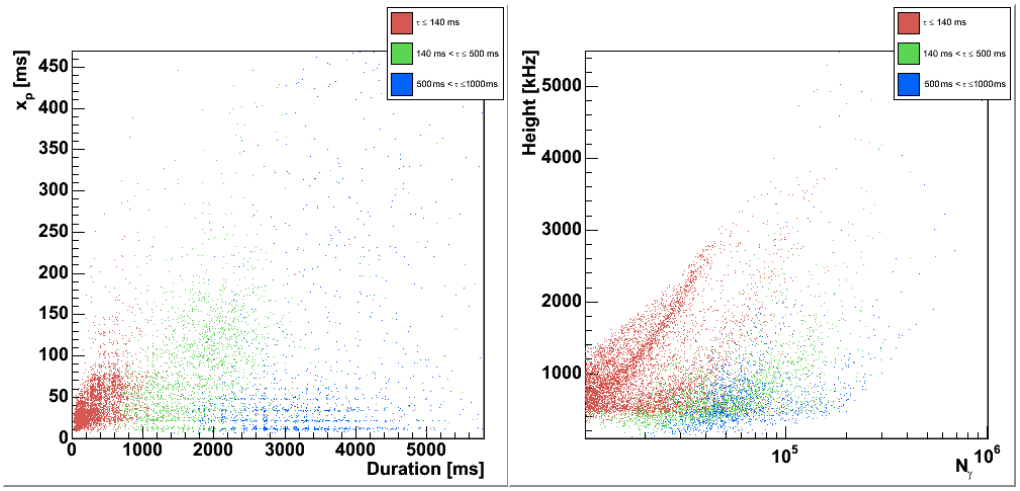

Figure 4.31: *Left:* Time-to-Peak vs Duration scatter plot. *Right:* Computed Burst Height vs Burst Integral scatter plot. Note the logarithmic scale on x-axis. On both plots, points in red refer to $\tau \leq 140\ ms$, points in green refer to $140\ ms < \tau \leq 500\ ms$, points in blue refer to $500\ ms < \tau \leq 1000\ ms$

4.4.3 Comparison with a simulation.

The optical background has been simulated [39] in order to analyze its effect on the trigger rate of the 12-string detector. The same simulation has been applied to the PSL configuration in order to perform a comparison with real data.

The background was modeled as a fixed contribution of $60\ kHz$[40] from ^{40}K and a large variety of contributions from luminescent animals, flashing after collisions in the turbulence layer around the OMs, LCMs and EOC. Figure 4.32 shows the distribution of collision events.

Animals of different sizes, distributed according to a power law $(\frac{r}{r_0})^{\eta}$, have been taken into account. The parameters to be specified within reasonable ranges are hence the total density of organisms in water[41], their minimum and maximum sizes[42], the power law index[43] η, the characteristics for different animals (number

[40] It is known that the real ^{40}K contribution is less than half of this value (see section 4.1.1): the excess counts may be thought of as an additional contribution of continuous bioluminescence.

[41] $1,\ 3$ or $10\ m^{-3}$.

[42] $9.9 \div 10\ mm,\ 10\mu m \div 10\ mm$ or $10 \div 11\ \mu m$.

[43] Fixed to 3.

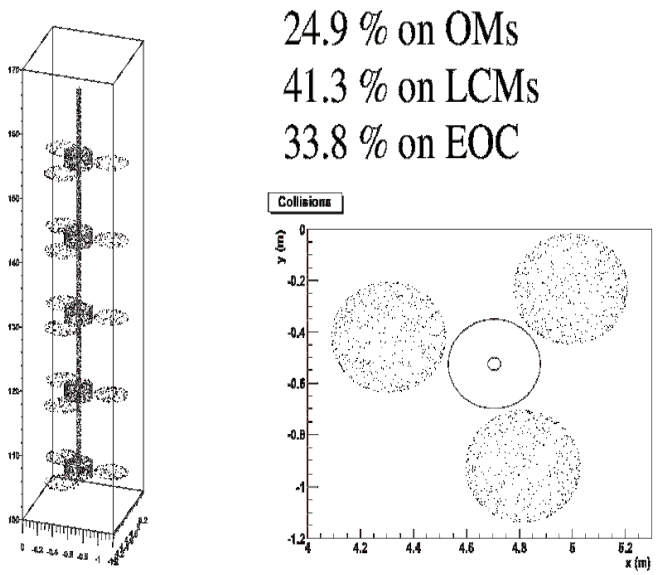

Figure 4.32: Space distribution of simulated collision events (represented by small dots) along the PSL string. The percentage of collisions with the OM, LCM and EOC are also given. The drawing on the right represents a top view of a single storey. [39]

of photons per burst $N_\gamma(r)$, $x_p(r)$, $\tau(r)$) and the water speed[44]. The lower limit on burst intensity is the one set by what we know from biology: $N_\gamma \sim 10^8$. The wide baseline variations when the burst fraction is low are simulated introducing an additional bioluminescent component $N_\gamma^{bio} \propto (1 + \alpha v_w)$, with $\alpha = 10^4$.

The data output is the counting rate of single OMs in the standard frame-time. Results of the simulation for the ANTARES detector are shown in table 4.2.

The reasonableness of the simulation has been checked by applying the same algorithm used in the analysis of real data.

The available simulations provide a maximum of 10^5 frames per OM, corresponding to slightly more than a 15'-period. Therefore, only one value for baseline and burstfraction per OM can be computed within a single run.

Figures 4.33, 4.34 and 4.35 show the distributions of burst quantities, computed as in the case of real data.

No cuts on burstfraction have been applied since the number of events sat-

[44] 1, 5 or 10 cm/s.

		$v_w\,(m/s)$		
		0.01	0.05	0.10
$n\,(m^{-3})$	1	0.08	0.84	1.4
	10	0.38	10 [1.1]	392 [121]
	100	17 [2.2]	50110 [617]	**

Table 4.2: Trigger rates (kHz) for the ANTARES detector depending on values of current speed and animal density assumed in the simulation. Numbers in brackets show simulation results when ignoring OMs with too high counting rates. Notice that available simulations for the entire detector have sometimes been produced using parameter values different from the ones used in the simulations of the PSL.

isfying the selection criteria is extremely small: almost all simulation runs are characterized by a burstfraction equal to 0.5.

Looking at individual runs, the only relevant dependence of the results on parameter values is on the total density of animals and water speed. Though the

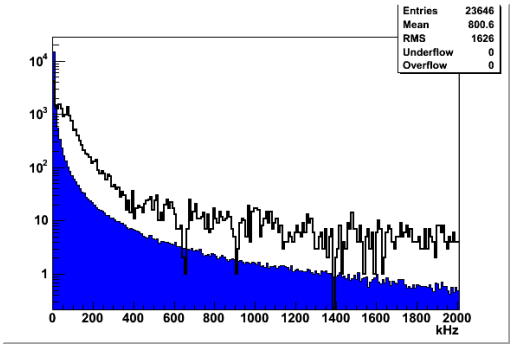

Figure 4.33: Burst Height distribution. The shape of the distribution is compared with the one resulting from the analysis of real data (shown in blue).

discretization of these parameter values may not help to get smooth histogram shapes, the double-peaked structure of the individual contributions shows that the simulation is not fully trustworthy.

The lack of very short bursts can be due to the choice of too short a range of distances between the bioluminescence events and the OMs. Bioluminescence emission probably does not occur only within the $20 \div 30\ mm$ turbulence layer around the obstacle, though these events are the main contribution.

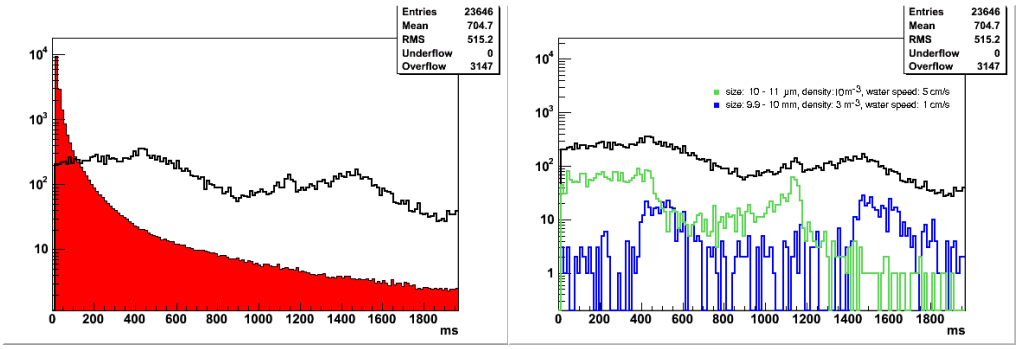

Figure 4.34: Burst Duration distribution. *Left:* The shape of the distribution is compared with the one resulting from the analysis of real data (shown in red). *Right:* Superimposed histograms show the contributions from two samples with different characteristics. Notice the multi-peaked structure in individual contributions.

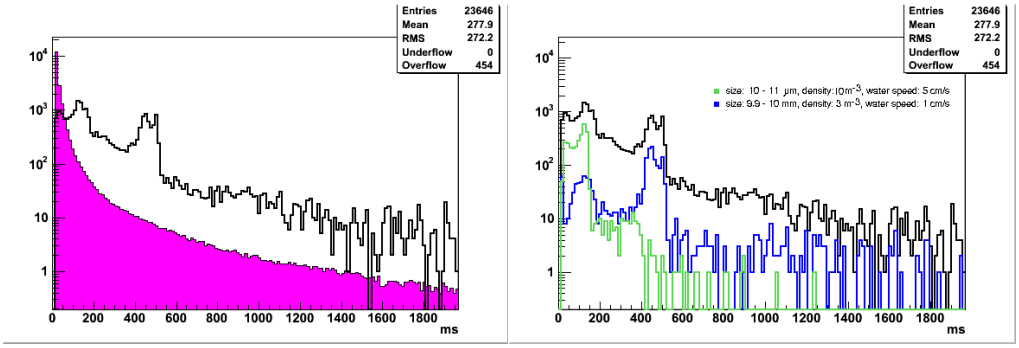

Figure 4.35: Time to Maximum distribution. *Left:* The shape of the distribution is compared with the one resulting from the analysis of real data (shown in purple). *Right:* Superimposed histograms show the contributions from two samples with different characteristics, as well as the total. Notice the multi-peaked structure in the individual contributions.

Another possible explanation is a wrong choice of the weight function for populations of different sizes (light yield and time characteristics). If this were true, it could also account for the double peaked structure of the histograms, which hence would come from too simplified a weight function and too small a range of animal sizes.

A discussion of the results of this very preliminary analysis is still under way with the author of the simulation, to define possible adjustments and to evaluate consequences on triggering.

Chapter 5

An attempt to improve the performance of a large underwater Čerenkov detector through the use of Hybrid PhotoDiodes (HPD)

5.1 Characteristics

The HPD is a photodetector consisting of a photocathode, deposited on the inner side of the entrance window, and a solid state sensor -as anode- encapsulated in a vacuum envelope. It is similar to a standard PMT for the photocathode, but it differs from the former for the lack of the dynodes: the emitted photoelectrons are accelerated by a potential difference of the order of $10 \div 20\ kV$ directly onto the silicon sensor which is usually kept at ground potential. The electric field can be shaped by means of electrodes in order to provide suitable electro-optical properties, e.g. a linear demagnification between the photocathode and the silicon diode sensor. The kinetic energy of the photoelectrons absorbed by the silicon pad gives rise to the creation of electron-hole pairs in the silicon sensor, suitably depleted, resulting in a detectable current.

HPDs combine the high sensitivity of photomultiplier tubes with the excellent space and energy resolution of solid state detectors. Further features are the high intrinsic speed and the excellent linearity in gain as a function of HV.

As it is clearly visible from a comparison of an HPD and a PMT in figure 5.1, the HPD pulse height spectrum is characterized by a small value of the relative

charge amplitude fluctuation $\frac{\sigma_1}{Q_1}$, lower at least by a factor of 4 compared with the one of a conventional PMT [50]. This excellent peak separation can lead to

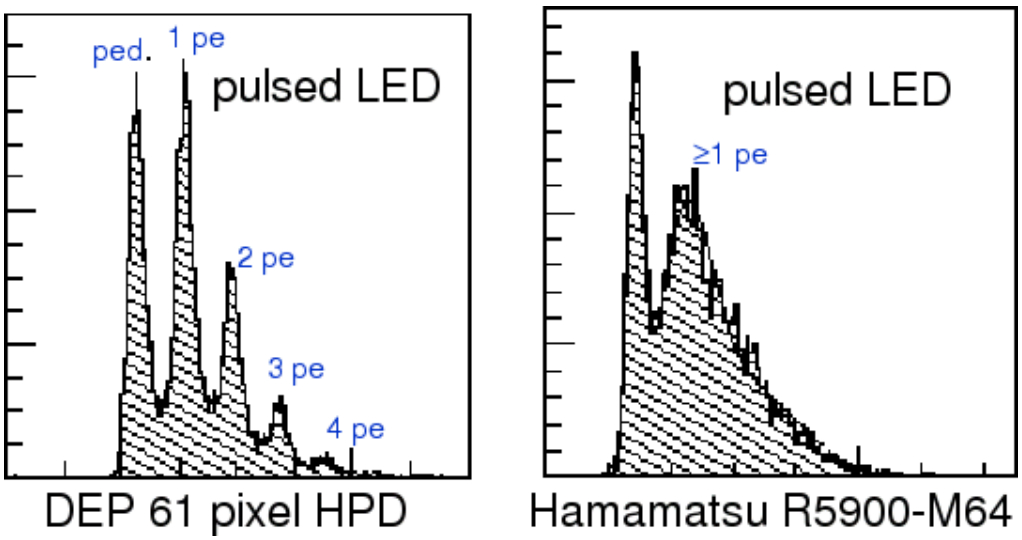

Figure 5.1: Example of calibration spectra for an HPD (left) and a PMT (right). Visible photoelectron peaks are marked by a blue label.

interesting implications when exploited in light detection for neutrino telescopes: it would improve background rejection and signal amplitude measurement, with welcome consequences on speed and quality of event reconstruction.

	ϵ_Q [%]	gain G	$\Delta G/G$ [%]	photon counting	spatial resolution
HPD	25 max.*	10^3	$1 \div 4$	yes	up to 2048 pixels
PMT	25 max.*	10^8	$40 \div 70$	limited	up to ≈100 pixels*
APD	$70 \div 80^\dagger$	10^2	200	poor	no

* Spectral sensitivity depends on photocathode type: $\epsilon_Q \approx 25\%$ at $400\ nm$ for bialkali.

* This limited imaging capability is obtained with multi-anode PMTs, at the price of reduced Q.E. and gain uniformity over the photocathode surface.

† Higher q.e. in red/infrared region, decreasing towards the UV.

Table 5.1: Comparison of the characteristics of a standard Hybrid PhotoDiode with a PhotoMultiplier Tube and an Avalanche PhotoDiode.

A drawback of the HPD is its small gain, which implies the need of an external low-noise amplifier.

Windows and photocathodes

Depending on the specific application, HPD's can be produced with various photocathode and window types. The key parameters are the energy threshold of the photocathode, its spectral sensitivity $S(\lambda)$ or quantum efficiency $\epsilon_Q(\lambda)$ and the cut-off wavelength of the window. Widely used photocathodes are of the bialkali (K_2CsSb) or multialkali (SbNaKCs) type. For special applications also VUV sensitive CsTe or negative electron affinity cathodes (GaAs, GaAsP, InGaAsP) are available.
The effective sensitivity of the HPD is limited by the transmission of the entrance window, with lower wavelength cutoffs ranging from $300\ nm$ for lime glass down to $160\ nm$ for fused silica quartz and even $105\ nm$ for LiF single crystal windows.

Silicon sensor and gain mechanism

The accelerated photoelectrons bombard a backward biased silicon sensor and impinge to a depth of a few μm. The number of created electron-hole pairs per photoelectron, i.e. the gain of the device, is given by $G = (\Delta V - E_0)/W_{e-h}$.
Here $W_{e-h} = 3.61\ eV$ is the average energy needed for the creation of a single electron-hole pair in silicon, E_0 is the energy ($\approx 1 - 2\ KeV$) which is lost in non-active material layers over the Silicon detector (aluminium contact layer, n^+ layer) and ΔV is the potential difference applied between the photocathode and the silicon sensor. For $\Delta V = 20\ kV$ a gain of about 5000 is achieved.
The small penetration depth of the electrons results in sub-ns rise and fall times for the output signal.

The charge amplification process is purely dissipative and non-multiplicative, i.e. in contrast to a PMT, where large gain fluctuations are due to the Poisson-distributed number of electrons resulting at every dynode. The HPD gain variation is given by the quadratic sum of a σ_0 contribution due to the pedestal noise and $\sigma_n = \sqrt{GFn} = \sqrt{n}\sigma_G$, where $F \approx 0.1$ denotes the Fano factor for silicon, $n = 1, 2, 3..$ the number of photoelectrons: $(\sigma_n^{tot})^2 = \sigma_0^2 + n\sigma_G^2$ [43]. In practice σ_n variations are much smaller than the noise σ_0 of the readout electronics. Hence, it is the pedestal width which will finally determine the energy resolution of the HPD.

When electrons with relatively low energies ($20\ keV$) impinge on the silicon sensor, there is a 20% probability that the electron will be back-scattered into the vacuum, hence depositing only a fraction of its energy in the silicon; this gives rise to a continuous background on the low energy side of each peak. This effect limits

the photon counting performance of the detector when irradiated with a relatively large average number of photons.

Imaging

Segmenting the silicon sensor in diode strips, pixels or pads, which may be individually read out, results in a photodetector with high spatial resolution. The spatial resolution of the HPD is, however, determined not only by the granularity of the sensor but also by the electro-optical properties of the HPD. Distorsion of the electric field as well as the distribution of the emission angle and energy of the photoelectrons at the photocathode lead to a reduced space resolution, characterized by the *point spread function*. Carefully designed optics are able to partly correct for the aberrations and achieve point spread functions below $50\ \mu m$ at $20\ kV$. The number depends on the initial kinetic energy E_k of the photoelectron, the high voltage ΔV and the length L_{HPD} of the electron drift path, approximatively through the following relation: $\propto \sqrt{L_{HPD}\frac{E_k}{\Delta V}}$.
Above a certain number of channels (a few hundreds) it becomes impractical to readout the detector through individual vacuum feedthroughs. In this case the readout electronics has to be integrated in the vacuum envelope. The signals, either digital or analog, are then read out in a multiplexed scheme through a relatively small number of feedthroughs. This tecnique requires components which are conform with the tube processing (vacuum bake-out) and long term operation in vacuum (minimum outgassing[1] and low power consumption).

General considerations on HPD fabrication

HPD's have to be operated under excellent vacuum conditions. Typical values reported in the literature lie in the range $10^{-7} \div 10^{-8}\ Pa$. Collisions of the fast electrons with atoms of the residual gas create ions which are accelerated back onto the photocathode. Feedback induced noise and a continuous degradation of the cathode efficiency will be the consequence. In order to reach these vacuum conditions the deposition apparatus including the envelope and the silicon detector have to undergo a bake out cycle at temperatures up to $300\ ^oC$ [45].

HPD's can be produced in two basically different types of processes:

[1] Reached with the help of *getters* put inside the envelope.

Internal processes The silicon detector is mounted inside the vacuum tube before the photocathode is deposited. The evacuated glass tube is closed, with the exception of small lateral pipes through which small evaporation sources can be inserted. These openings are afterwards sealed off by melting the glass. The front-end electronics will be obviously bound to the silicon pad only after the evaporation process, when temperature is again far below $300\ ^oC$. This technique is the same widely used for photo-multiplier tubes.

External processes There are two main variants of external processes.
1) The photocathode is first deposited on a separated window. The window is then used to seal the vacuum tube which contains already the silicon detector.
2) The vacuum tube has a removable bottom plate. The photocathode is deposited onto the top window through the bottom hole. The tube is afterwards sealed off by means of the base plate which carries the silicon detector and the front-end electronics.

5.2 Development status

Hybrid Photodiodes, although developed more than 30 years ago, have only recently received attention by the high energy physics community. At the moment, only few companies [2] commercialize these detectors.

Current and future applications in high energy physics lie in the fields of scintillator readout, particularly for Čherenkov light detection. Hybrid Photodiodes can be classified with respect to their electro-optical design, which basically falls into three categories:

Proximity focusing This design leads to compact and, thanks to the small gap between photocathode and silicon sensor, highly B-field tolerant detectors. Since there is no demagnification, the photosensitive area of the detector is limited by the size of the silicon sensor.

Cross focusing A cross focusing design is chosen when high resolution imaging is required, because the electrostatic lens effect largely compensates for the spread of the photoelectron velocity and emission angle at the photocathode.

[2] DEP (Delft Electronic Products), Hamamatsu and INTEVAC Corporation, to name the most important.

Cross focused tubes allow for strong demagnification; they however imply a relatively large distance between cathode and solid state sensor, which results in a pronounced magnetic field sensitivity.

Fountain focusing It represents an alternative to the cross focused HPD if a reduced spatial resolution is acceptable. This optics does not correct for the emission angle distribution but results in a simple and compact tube design combined with a linear demagnification over the full acceptance. The sensitivity to magnetic fields is similar to the cross focusing design.

5.3 Proposal for a 10" hemispheric HPD

The specific requirements that a new photodetector must satisfy for being useful in a neutrino telescope, have been formulated on the basis of the ANTARES experiment requirements [25, 26].

- First of all, it should present all the advantages of the Hamamatsu PMT R7081-20 [27] already chosen for the ANTARES experiment or, when this is not possible, it must at least respect the minimum requirements stated by the collaboration [25]:
  - 10-inches hemispheric photocatode, which allows a large field of view: an effective area of at least $400\ cm^2$ and good collection efficiency over 60^o off the PMT axis.
  - high quantum efficiency in the wavelength range of interest: the choice of the same photocathode and window materials should reproduce the PMT Q.E. and its spectral response, with the exception of small differences due to the window thickness or the evaporation process.
  - peak to valley ratio, computed from the charge spectrum, greater than 2. See [26] for the exact definition used.
  - fast response: electron transit time below $80\ ns$, signal rise time below $5\ ns$ and FWHM below $12\ ns$.
  - short Transit Time Spread: for the PMT used in ANTARES the TTS is below $3.4\ ns$ at the nominal gain of 10^8.
  - good signal linearity: the saturation limit should be for a signal of $60 \div 100$ photoelectrons.

For an HPD the linearity is always satisfied, because the signal amplitude is proportional to the number of e-h pairs produced in the silicon, which in turn is linear in the HV supply. The dynamic range is however limited by the signal shaper in the front-end electronics.

- We also ask for some additional features, peculiar to the HPDs:
  - good imaging: linear demagnification and good spatial resolution, with the hope of being able in the future to take advantage of the spatial information for triggering and during the event reconstruction process.
  - strong demagnification power, in order to keep limited the silicon pad dimensions while using a rather large photosensitive surface.
- In the detector design attention must be paid to the following constraints:
  - the single photoelectron amplitude must be at least a factor of ten higher than the noise level of the electronic circuit.
  - the detector should be concretely feasible at a reasonable cost: one must deal with problems concerning the evaporation process, the envelope resistance to the high vacuum level, the possible discharge due to high voltages applied between close electrodes.
  - the whole object design must fit the Benthos sphere dimensions[3] and weight limits[4]: taking into account the fact that part of the OM has to be occupied by additional apparatus, the total HPD height is limited to $35\ cm$ and the photocathode radius of curvature is limited to $19\ cm$.
  - the detector should have a minimum life of ten years. This is maybe the hardest condition to satisfy: if we start now the development of a new device to be used within the next seven years, the time for tests will probably not be sufficient.

The simulation of the electron optics has been carried out within this thesis work using the commercial software SimIon 7.0. The program allows to draw three-dimensional electrodes and to study the fly of ions of adjustable charge, mass and initial energy through them.

[3] Its inner diameter is $40.2\ cm$.

[4] The weight of the present PMT is about $1\ Kg$.

Though the HPD production through an external process has the essential advantage of avoiding the risk of contaminating the silicon detector during the photocathode evaporation, its choice requires the availability of a specific deposition apparatus. The entire process needs high vacuum around the tube, the silicon sensor and the other components which will be sealed together after the evaporation. Such a device, moreover, allows to work on a single HPD a time, making the production time too long for the number of tubes needed by a km^3 telescope. By choosing the standard evaporation process used for commercial PMTs, one may also pay less attention to the geometrical constraints imposed by the available deposition apparatus. However, in this case, the high temperature suffered by the silicon pad and its possible contamination by Cesium during production will have to be taken into account.

The final design is shown in figure 5.2. The photocathode is slightly elliptical ($a = 115\,mm,\ b = 125\,mm$), with the minor axis parallel to the axis of symmetry of the tube. The maximum distance between the photocathode and the aluminium layer which covers the silicon pad is $230\ mm$.

The signal to noise ratio requirement contrains the PMT amplification to be at least $5 \cdot 10^7$. Due to the different structure of an HPD this high gain is not necessary, as well as impossible to achieve. The output signal of a silicon sensor is very small, but a subsequent amplification stage would make it processable by the standard electronics. The main noise source which should be taken into account for the HPD is the amplifier itself, which usually contributes to the pedestal charge with some hundreds of electrons (see below for an estimate performed on the basis of the chosen electronics). An HPD gain of 5000 is then the minimum allowed to get a good signal to noise separation.

The photocatode is therefore set to $-20\ kV$, the anode (the aluminium layer above the silicon pad) to $0\ V$. The ring electrodes, left to right in figure 5.2, are set to $14.5\ kV$ and $11\ kV$.

The electrons emitted by the photocathode have been generated within the proper energy range[5] $0 \div 1.88\ eV$ and angular distribution for the direction of emission [6] (the Lambert distribution, see [46]). The gain will be $\frac{2{\cdot}10^4\ eV - 2000\ eV}{3.6\ eV} \approx 5000$.

[5] Computed by considering the work potential of the Bialkali photo-cathode, $2.25\ eV$, and the wavelength sensitivity range $300 \div 600\ nm$ of a Bialkali photocathode deposited on a borosilicate-glass window.

[6] However, some preliminary tests have shown that, thanks to the high potential difference applied to the electrodes, the initial direction of the low energy photo-electrons can be neglected for the study of the TTS.

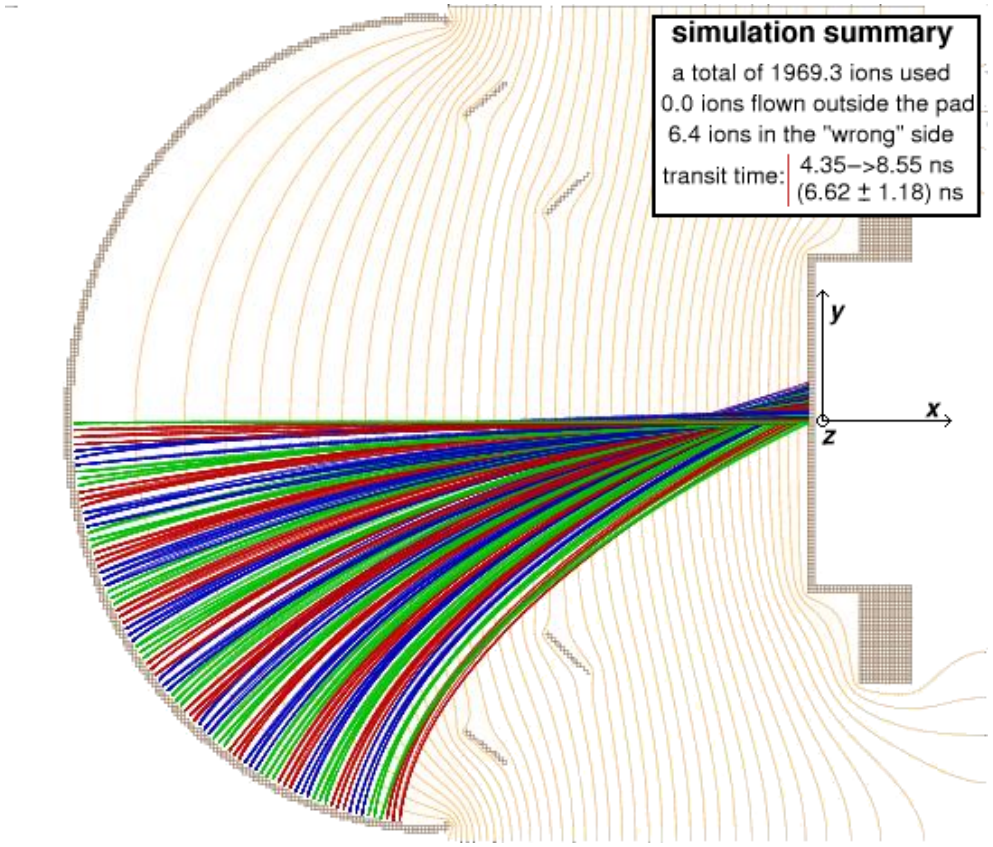

Figure 5.2: Design of the HPD proposed. Two-dimensional section of the device as designed for the electron optics simulation. Trajectories of all 446 ions simulated are shown: different colours (red, green and blue) draw a distinction between nearby groups of 5 ions for sake of clarity. Equipotential surfaces in steps of $0.5\ kV$ are shown in orange.

In order to take into account the project feasibility, an industrial silicon pad has been chosen. It is a 7-pad silicon sensor, $25\ mm$ in diameter, (see figure 5.3) already under development by the DEP Company for a proximity focusing HPD. The electron optics has been optimized for focusing and imaging in such a $25\ mm$-large silicon pad. The depletion depth is $300\ \mu m$ for a typical bias voltage of $80\ V$, the capacitance is $30\ pF$ for each external pixel and $20\ pF$

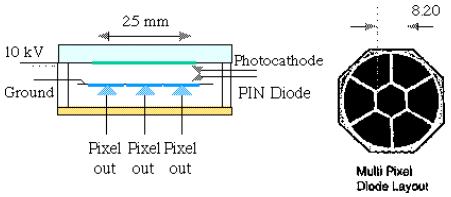

Figure 5.3: Schematic and tube structure of the 7-pixel DEP HPD.

for the central one.

Simulation results are shown in figure 5.4. In the TTS distribution, each ion is considered with a weight equal to $2\pi r$, where $r = R\sin\alpha$ is the distance of the point of photoelectron emission and the simmetry axis of the HPD[7]. The use of weights allow to use a manageable two-dimensional ion generation for a three dimensional analysis.

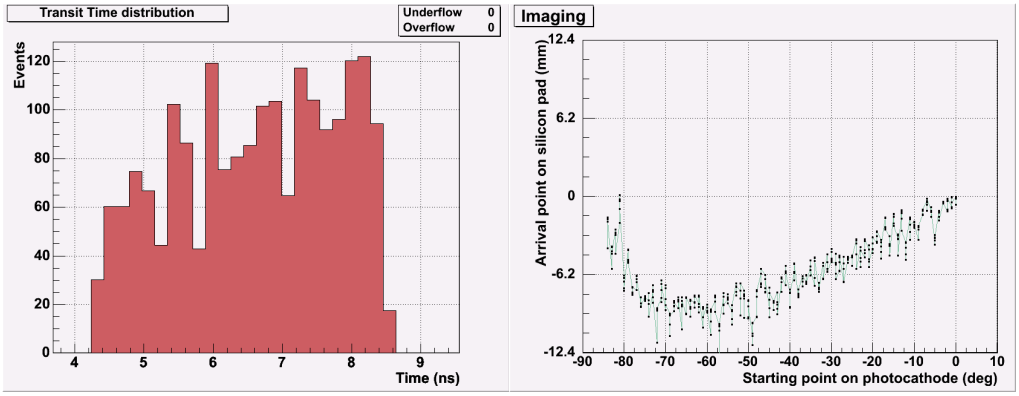

Figure 5.4: Result of the electron optics simulation (see figure 5.2-left). *Left:* Transit Time distribution. *Right:* Correlation between photocathode and silicon pad. The ordinate is the y-coordinate of the arrival points at the silicon pad; the abscissa is the angle between the HPD symmetry axis ($y = 0$) and a line drawn between the point of photoelectron emission and the photocathode center of curvature.

The TTS distribution appears rather flat, with a full width of about $3\ ns$ and a σ width of $1.18\ ns$. Better results could be achieved by increasing the HVs applied to the photocathode (and the electrodes), but too large potential differences between close electrodes should be avoided.

Thanks to the cylindrical symmetry of the detector, also the correlation between photocathode and silicon pad can be studied as a two dimensional problem, through the projection on the xy-plane. A linear correlation which perfectly fits the $8\ mm$ width of the smallest pixel in the pad could be obtained at the cost of reducing the angular acceptance to $\pm 80^o$ or by adding at the photocathode edge a *bleeder* electrode[8]. Limiting at $\pm 78^o$ the photocathode layer and taking into

[7] α is the angle between the HPD symmetry axis and a line drawn from the photocathode center of curvature and the point of photoelectron emission, the same used in the imaging plot; R is the major axis of the ellipse which constitutes the photocathode (the one ortogonal to the symmetry axis).

[8] An electrode accurately designed to locally change the field lines

account the shadow effect due to dead zones between silicon pixels, the effective area of the HPD turns out to be about $470\ cm^2$, still within the ANTARES experimental requirements. The excluded ions are also the fastest ones, hence also the TTS distribution can be sharpened.

These simulation results have been considered satisfactory to demostrate the feasibility of an electron optics satisfying the requirements. I started hence to deal with other aspects of the feasibility.

The amplification stage introduce a delay in the detector output which was absent for the PMT. However the reduced transit time of the HPD with respect to the PMT ($6\ ns$ instead of $78\ ns$) compensates for it. Another point is instead more critical in dealing with the electronics: the shaping time of the standard electronics is hardly below $50\ ns$. One of the best possible choices is for example the combination of the trigger chip TA32cg and the preamplifier and shaper chip VA32C from Ideas ASA Company[9], which reaches a peaking time of $75\ ns$. Hence the requirement of a fast response for the detector is not yet satisfied: a dedicated electronics should (and could[10]) be developed. However, it is clear even now that developing electronics with the required large dynamic range and low noise imposes a multichannel readout. The configuration proposed above, for example, which is one of the most suitable at present, is characterized by a $40 + 12/pF\ e^-$ RMS noise[11] and a dynamic range of $9 \cdot 10^4\ e^-$ per channel, equal to 18 p.e. only (when using the proposed HPD with the low gain of 5000).

The pulse height spectrum of an HPD is highly dependent upon the silicon pad. However, since no simple estimate can be obtained from the characteristics of the sensor given in the data sheet, the pulse height spectrum characteristics are taken from a real HPD already built by the TOM[12] group. Taking from measurements the σ of the gaussian pedestal and the fraction of backscattered events, a simulation which reproduces the data can be implemented.

A simplified gaussian model [43] for the photoelectron peaks is used. Once we set the average number of p.e. we know from Poisson statistics the probability of each p.e. peak. For each event, the charge deposited by every p.e. in the silicon pad is randomly generated from the gaussian s.p.e. distribution and added to a

[9] www.ideas.no

[10] [47, 48] and private communication from Riccardo De Salvo.

[11] For the chosen silicon pad, we have $30\ pF$ capacitance per pixel, i.e. a noise of $400\ e^-$ per channel.

[12] A small project from INFN-Pisa, which has studied the possibility to upgrade the CLUE telescope performance replacing the focal planes sensors with 10" HPDs, manifactured with Rb_2Te photocathodes on quartz windows.

noise charge generated from the pedestal distribution. The additional contribution to σ_n/Q_1, the width of the n^{th} p.e. peak, $\sqrt{GFn}/G = \sqrt{0.1 \cdot n/5.5 \cdot 10^3} = 4 \cdot 10^{-3} \cdot n$, is neglected. The electronic noise is white noise, hence the pedestal distribution is a gaussian. Backscattering can be approximately treated as a constant probability on the left side of a gaussian (see figure 5.8), and the ratio between the area of this constant left tail and the total area is set by experimental measurements. The comparison of a real spectrum and its simulation in figure 5.5 shows the robustness of the approximation.

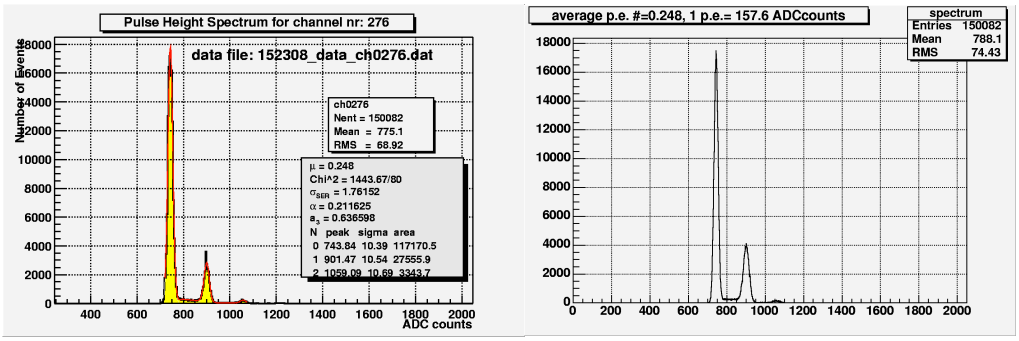

Figure 5.5: *Left:* an example of the Pulse Heigth Spectrum of one channel of the 10" HPD developed by TOM [50]. The superimposed fit uses a model for the spectrum which is slightly better than the raw simulation used in this work. *Right:* A simulation of the Pulse Height Spectrum, using the simple model described in the text and σ_{peak}, gain and backscattering fraction from real measurements.

The 7-pad silicon detector proposed has an average pixel capacitance of $28\ pF$, significantly higher than the $1\ pF$ capacitance of the single pixels for the TOM HPD. Hence it is also reasonable to assume, together with the decrease of $Q_{p.e.} - Q_0$, an increase of the pedestal width.

A preliminary analysis, by using the commercial software ANSYS, has been performed by Fabrizio Raffaelli[13] to evaluate the resistance to stress of the designed envelope. The result when an external pressure of $1\ atm$ is applied is shown amplified in figure 5.6: the maximum deformation is $9\ \mu m$. The stress reaches $6\ N/mm^2$ in the critical joint between the photocathode and the rest of the envelope. The maximum stress which could be beared by borosilicate glass is $7\ N/mm^2$, hence these preliminary results are satisfying.

To think at the HPD as a real possibility for a neutrino telescope, another problem that must be solved is related to the HV power supply. The dimensions of the

[13] INFN, Pisa.

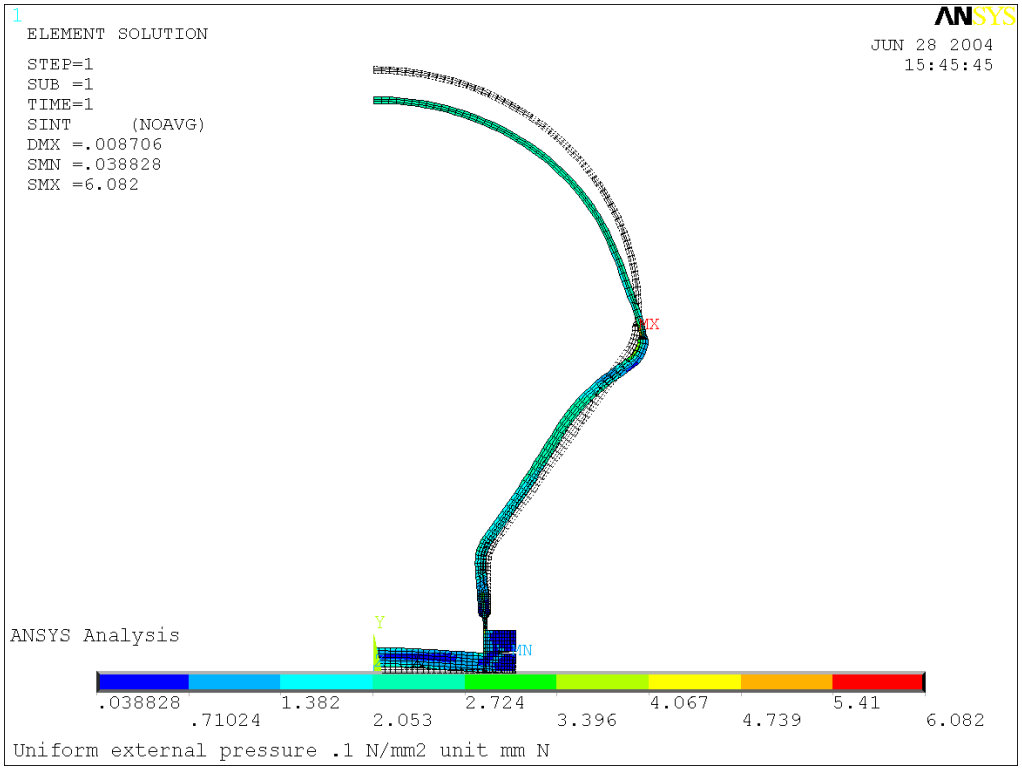

Figure 5.6: Envelope compression when an external uniform pressure of $1\ atm$ is applied. The original envelope shape is shown in black, the deformation is amplified and shown as a coloured shape. Colours show the result of stress analysis performed by using the criterion of the maximum shear stress. Points of maximum and minimum stress are labelled MX and MN. Kindely provided by Fabrizio Raffaelli, INFN Pisa.

standard[14] box housing a HV generator from $24\ V$ to $20\ kV$ are approximatively $180 \times 80 \times 40\ mm$. Though it is a much bigger space than the one now used in the Benthos sphere for the PMT base, it is not impossible to find a solution to fit the $26\ cm$-long HPD and the $18\ cm$-long power box within a sphere of $43\ cm$ diameter. Probably custom HV power supplies or slightly bigger pressure spheres could solve the problem, or even the HV could be generated outside the Benthos sphere. This last solution is maybe the most dangerous, due to possible water leaks along cables which lay in the water, however it would also avoid the heating of the sourrounding electronics due to the output power of $\approx 20\ W$.

[14] See www.iseg-hv.com or www.etps.co.uk, for example.

5.4 Analysis of the consequences of using an HPD in a large scale neutrino telescope.

The time needed to develope such a device is rather long, and it is impossible to think at the HPD as an actual possibility for the ANTARES $0.1\ km^2$. The effective advantages of using a Hybrid photodetector instead of a standard phototube could be then exploited for the envisaged km^3-scale neutrino detector.

The HPD usefulness has been tested implementing its behaviour in the Monte Carlo of such a detector and analysing how the reconstruction efficiency changes, in particular at low muon energies.

The starting point was the study already performed by Dimitrii Zaborov within the ANTARES and NEMO collaborations [56, 57] to adapt the ANTARES MonteCarlo tools to a km^3 detector and study the detection efficiency for several possible geometrical configurations. At high energies (tens of TeV) the amount of Čerenkov light is extremely high, hence the strings may be quite far from each other. Cylindrical symmetry with respect to the vertical axis may help to reduce azimuthal asymmetries in the reconstruction efficiency.

5.4.1 Detector configuration

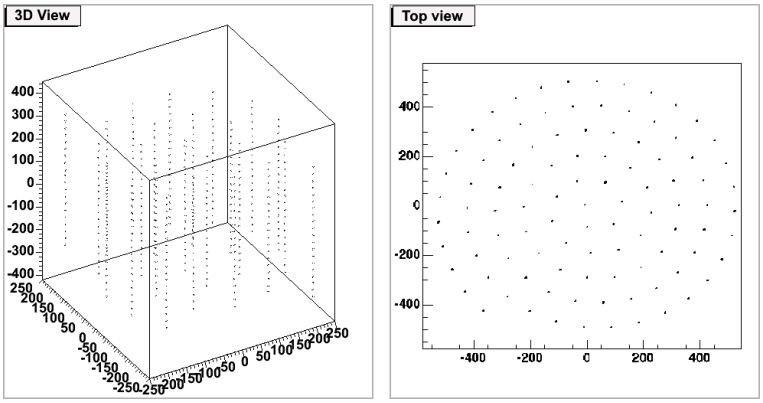

Figure 5.7: Detector layout. Distances are expressed in meters.

A very simple configuration has been considered in the following work. One hundred strings are deployed following a spiral having a maximum radius of about $460\ m$ (see figure 5.7), with an average distance between strings of about $100\ m$.

Each string consists of 20 storeys with a step of $30\ m$ between them. The storey configuration is the ANTARES one, with three optical modules looking at 45^o below the horizontal. One tiltmeter is assumed on each storey, and one hydrophone on each sector. No sea current was introduced in the simulation. However the position resolution was assumed to be $0.5\ m$ in the horizontal (x and y) directions and $0.1\ m$ in z, while the resolution in tilt and header were respectively 0.1^o and 0.02^o.

Each optical module contains one 10" light-detector, which can either be a PMT or an HPD. The light detection simulation is implemented in the packet GEASIM [53], and is used within the programs KM3 [54] and MODK40 [55, 53].

The Hamamatsu R7081-20 PMT (see page 27) is the default simulation in the ANTARES software, and its parameters are automatically used. Only two characteristics have been modified to simulate the HPD: the Pulse Height spectrum (simulated by the routine RANGAIN) and the Transit Time Spread distribution (simulated by the routine RANTTS). In figure 5.8 the distributions used for the PMT and HPD are compared.

Figure 5.8-left shows the output of the routine RANGAIN, which takes as input

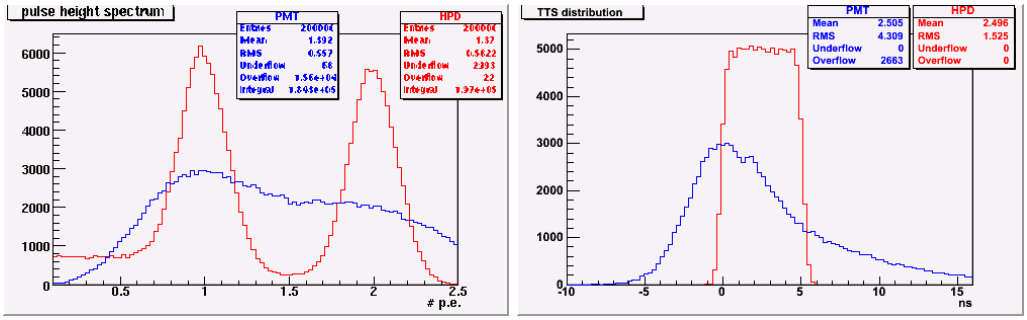

Figure 5.8: Raw output of simulation implemented in the GEASIM packet for the PMT (in blue) and the HPD (in red). *Left:* Pulse Height distributions. *Right:* Transit Time Spread distributions.

the number of photoelectrons produced on the photocathode for each event and randomizes it as the dynode chain would do. In the figure two p.e. peaks are shown, generated with the same statistics: since within the RANGAIN routine no information on the relative weight of each photoelectron peak is present (this information is generated at a previous stage, during the conversion at the photocathode), the figure is intended just for a direct comparison between the two photodetector types and should not be thought of as the simulation of real spectra.

Figure 5.8-right shows the output of the routine RANTTS, which takes as input the FWHM of the Transit Time distribution and generates as output an additional (either positive or negative) delay with respect to the average transit time. Again, both distributions are generated with the same statistics. For the HPD TTS simulation I did not use the raw (optimistic) result obtained with SimIon: the distribution has been spread a little bit more, taking into account that an additional TTS could appear by using front-end electronics slower than the PMT one. Moreover the HPD TTS distribution has been shifted in order to reproduce the same average transit time as in the PMT case.

Effective area, quantum efficiency, dark current noise, shape, height and time duration of the anode signal may be left unmodified because they depend on the photocathode only (like the first two characteristics) or because I assumed that they may be properly adjusted with the right choice for the front-end electronics (all the output signal characteristics fall into this category).

5.4.2 Simulation parameters

A general description of the ANTARES software can be found in appendix B. The files describing detector configurations have been processed using the program GENDET to obtain the detector geometry file, then the program GENTRA (package GENNEU) has been used to generate the files describing the muon flux as follows:

- The muon flux is distributed as E^{-1} within an energy range $100\ GeV \div 500\ TeV$.

- Muons are distributed uniformly in solid angle. We are interested only in detector efficiency, hence it is also interesting to estimate the fraction of downgoing misreconstructed events.

- Starting points of the tracks are on the surface of a cylindric volume. The can radius is $860\ m$, its height is $2400\ m$.

Only 40000 muon tracks have been simulated, because of limitations in simulation time and disk space. The track data have been used as an input for the main simulation program KM3. KM3 simulates emission and propagation of Čerenkov light in the water within the generation can defined by GENTRA. The same input file has been used for both PMT and HPD simulations, thus exactly the same

tracks have been propagated into water using KM3. Spectral and angular characteristics of optical modules (light detector and glass sphere) have been considered as identical in both PMT and HPD cases, except for the modifications already described in the previous section.

The MODK40 program simulates light noise and signal digitization taking into account integration and dead time. No simulation of the pedestal noise is present in the standard software. The ambient noise rate which has been simulated is $70\ kHz$, again because of limitations in simulation time and disk space. After the signal digitization the information of hit origin (noise or signal) is lost, hence a separate simulation assuming no noise has been also necessary to understand the effect of background in event reconstruction.
Since the MODK40 runs after the light detection simulation (and requires itself the light detection simulation for the optical background), the p.e. noise distributions which have been used for the two light devices are not exactly the same. However the difference is not significant: it is only related to statistical fluctuations between two simulation runs.

The next step is muon track reconstruction by the program RECO. Only the *Aart Strategy* algorithm has been used. An attempt to apply the *Classic 3D Strategy* results in a smaller number of reconstructed tracks, and no further investigation on possible reasons has been done. The causality filter (used to select hits for track prefit) improved by Zaborov [56] has been used during this work.
One may set a minimum amplitude of digitized hits to be used for track reconstruction. Two different values (0.5 and 1.5 p.e.) of this threshold, which will be simply called "cut" from now on, have been used during this work. The minimum number of hits (anywhere in the detector) required for the prefit was set to 5.

5.4.3 Simulation results

The difference in results between the PMT and the HPD case is primarily due to the different pulse height spectra, though also the reduced TTS contributes. It is therefore of primary importance to quantify the differences in the digitized hit distributions, in order to better understand results on reconstruction efficiency and angular resolution.

Digitization results

In figure 5.9 the raw distribution of digitized hits (for low and high muon energies separately) is shown. As expected, in the "clean" pulse height spectra without ^{40}K

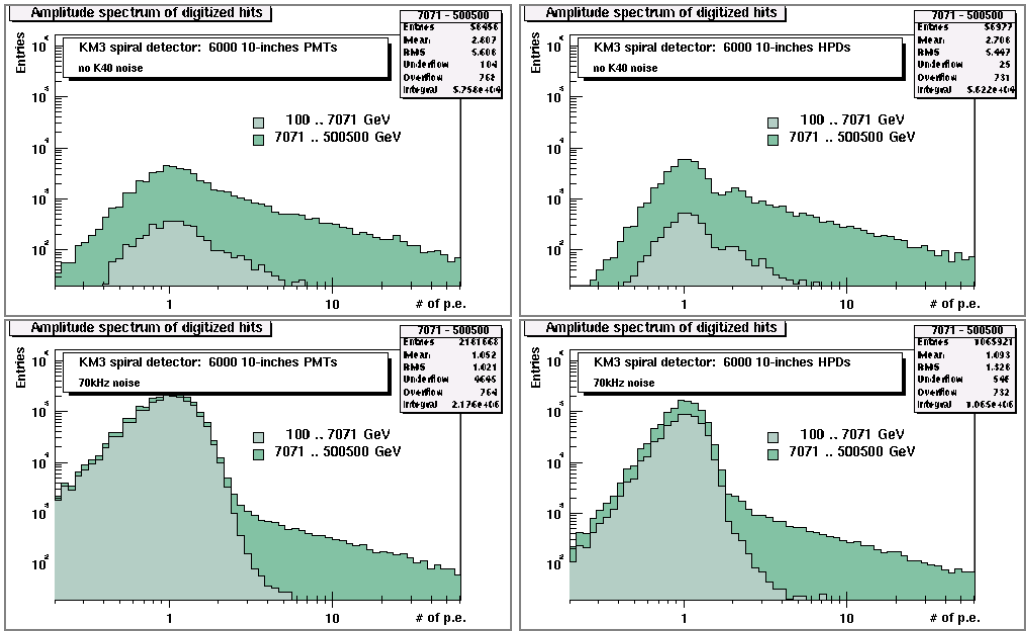

Figure 5.9: Comparison of amplitude spectra (expressed as number of photoelectrons) obtained for PMT (left column) and HPD (right column). No background noise is simulated in the two upper plots, while in the lower plots an additional $70\ kHz$ single p.e. contribution describes the background.

noise (upper plots), three photoelectron peaks after the first one are clearly visible in the HPD case, while the PMT spectra allows only a weak identification of the first two p.e. peaks. Moreover, a smaller number of signal hits are located below 0.5 p.e. amplitude in the HPD case, hence reconstruction which uses the 0.5 p.e. cut will have a higher efficiency than in a telescope using the PMTs.

When ^{40}K noise is "switched on" (lower plots), in both cases the first and the second p.e. peak height increase by more than one order of magnitude,while from the third p.e. peak on the distribution is almost unaffected.

The 0.5 p.e. cut is used to reject electronics noise. Thanks to the sharp HPD pulse height spectrum a better separation between electronics noise and signal is reached: less noise triggers the detector and a lower number of real hits are lost as a result of the cut; thus the angular resolution in reconstruction should be enhanced, even more than what can be predicted using the present MC. One must remember that no simulation of the pedestal is implemented in the MC, thus no check of the purity of the sample left after applying the cut has been possible.

A better evaluation may be obtained by looking at the integral spectra in figure 5.10. When no noise is present, a cut at 0.5 p.e. leaves 95% of the signal in the PMT case and 99% of the signal when using the HPD. The same cut when noise is taken into account shows that a largest fraction of digitized hits is rejected by using the HPD. Since we already concluded that this is not a signal loss, the result implies a better noise rejection.

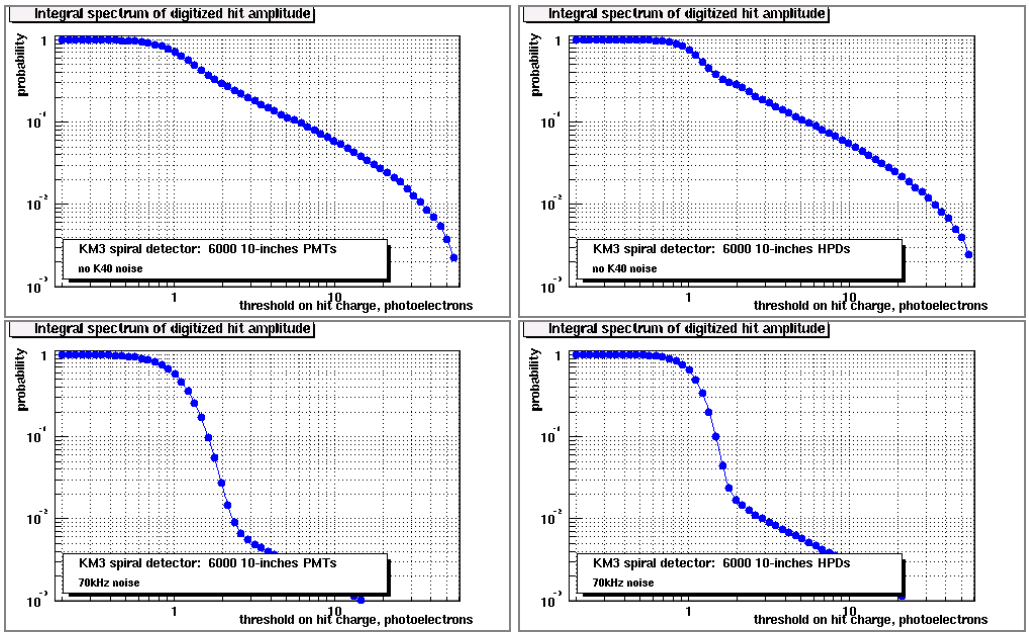

Figure 5.10: Comparison between PMT (left column) and HPD (right column) results: integral amplitude spectra. No background noise is simulated in the two upper plots, while in the lower plots the background is simulated as an additional $70\ kHz$ single p.e. contribution.

By looking at the plots with $70\ kHz$ noise added, we also find that a sudden drop in efficiency occurs at an amplitude of about 2 p.e. in both PMT and HPD cases. The drop is much less pronounced in the integral spectrum without noise, confirming that the effect is due to ^{40}K contamination which only affects the first two photoelectron peaks. From these considerations it has been chosen to apply also a cut at 1.5 p.e. for event reconstruction in order to perform a comparison. The effect of the 1.5 p.e. cut has also been studied in the simulation with no noise. The efficiencies for signal when using such a cut are 40% and 35% respectively for the PMT and the HPD case.

Reconstruction results

A total of about 4000 events are reconstructed by both the PMT and HPD telescopes when the p.e. cut is set to 0.5. The number of reconstructed tracks decreases to about 2500 for a p.e. cut at 1.5.

Though the numbers are not striking, the HPD results in a slightly better performance of the simulated neutrino telescope.

For a more accurate analysis, first of all we compare the reconstruction efficiency and angular resolution for the PMT and the HPD case when no noise is present.

Figure 5.11 shows the results obtained when a low cut of 0.5 p.e. is applied to the digitized hits.

The effective areas for reconstructed events are perfectly comparable. At $500\ TeV$ the effective areas are similar: $1.09\ km^2$ in both PMT and HPD simulation for all reconstructed events, $0.65\ km^2$ for the PMT-telescope and $0.74\ km^2$ for the HPD-telescope after quality cuts. At low energies a comparison of the "quality" of reconstructed events favours even more the HPD case .

The angular resolution is better in the HPD-telescope for the entire energy range, by almost a factor 2 both when using all reconstructed events and when only events selected by a quality cut are used. It must be remarked that statistics available for the computation of the low energy point in the angular resolution plot is a few hundred events.

Limiting the attention to the upward tracks only (for which the detector geometry is optimized), the HPD telescope angular resolution after quality cuts results in 0.06^o, two times better than the PMT telescope resolution.

In figure 5.12 the results of recostruction are shown for the case of a 1.5 p.e. cut applied to digitized hits.

The effective area below $50\ TeV$ is dramatically reduced by the higher p.e. cut. This is well understandable since "slower" muons generate less Čerenkov light, and hence 2 p.e. hits are unlikely. As already said, the 1.5 p.e. cut is disadvantageous in the HPD case since it (correctly) recognizes 65% of events as s.p.e. hits, while in the PMT case only 60% of events are below the same cut.

However at high energies the effective areas for reconstructed events are the same (a maximum of $0.98\ km^2$ for the PMT-telescope and $0.97\ km^2$ for the HPD-telescope) and, when limiting to events which passed the quality cuts results are even slightly better for the HPD ($0.73\ km^2$) than for the PMT ($0.65\ km^2$). The

"quality" of reconstructed tracks is enhanced in the HPD case (almost all the reconstructed tracks passed the quality criterion) for the entire energy range, and the effect is particularly advantageous at low energies, where only a very small number of events is reconstructed by both telescopes.

The results for low energies would require a higher statistics than the one available: few tens of events are not enough to draw conclusions at energies below few TeV. However, as already observed for the 0.5 p.e. cut, the angular resolution in event reconstruction above TeV energies is always better in the HPD case ($0.09^o \div 0.11^o$, even better after quality cuts) than in the PMT case ($0.16^o \div 0.3^o$, never lower than 0.13^o even after quality cuts).

Limiting the attention to the upward tracks only results are exactly the same as in the previous case of 0.5 pe cut.

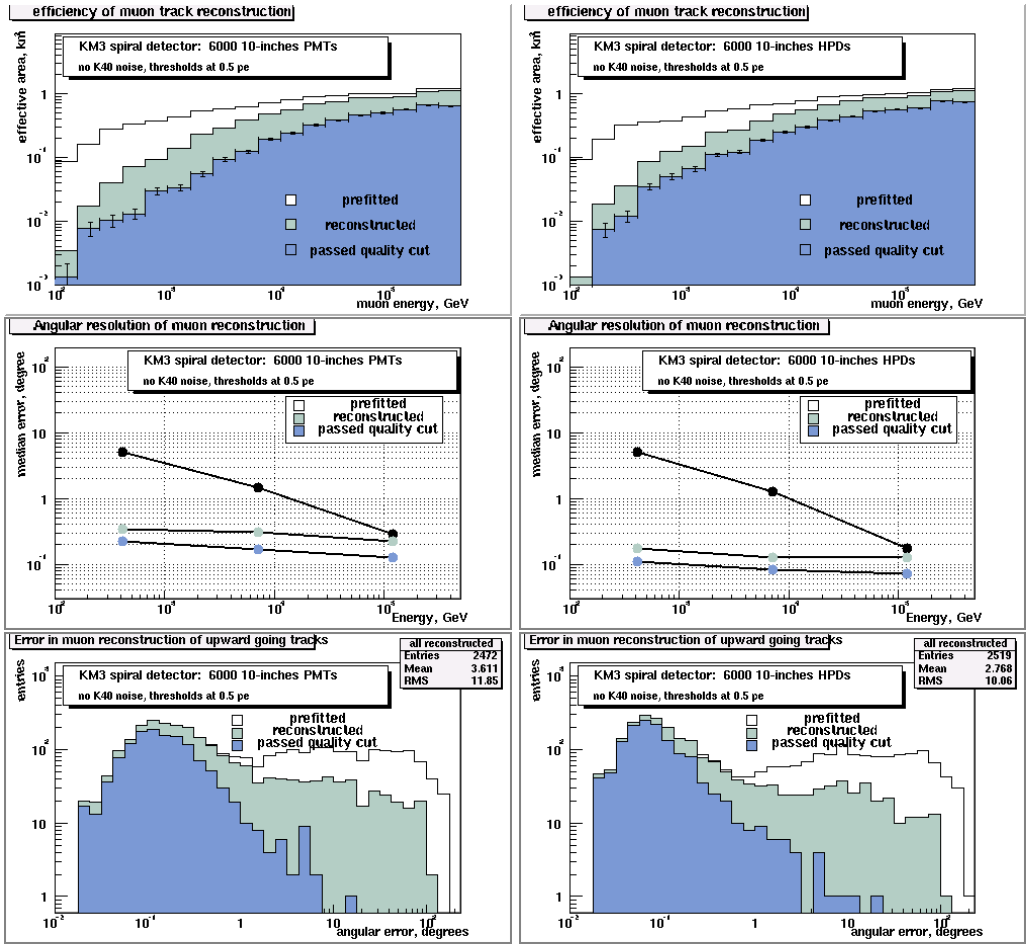

Figure 5.11: Comparison between PMT (left column) and HPD (right column) reconstruction results: effective area and angular resolution as functions of energy, distributions of angular errors in event reconstruction for upward tracks. No background noise simulated. Threshold set to 0.5 pe.

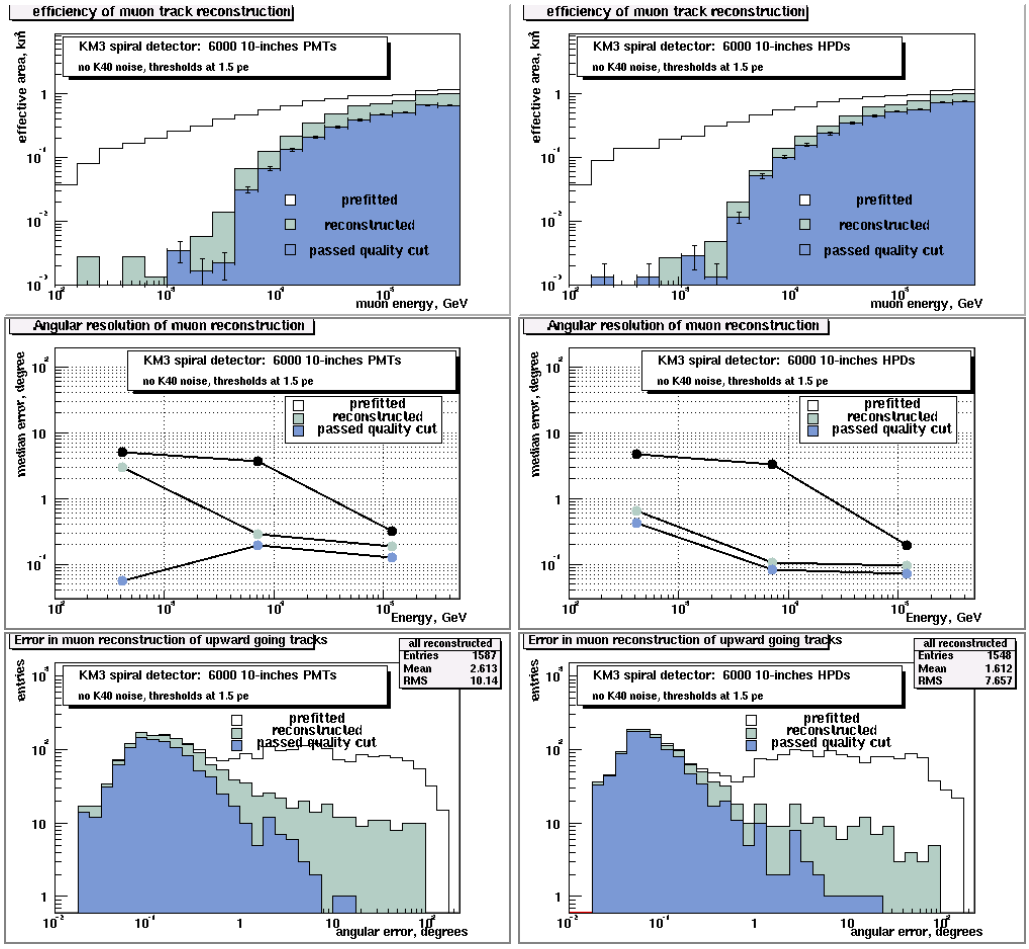

Figure 5.12: Comparison between PMT (left column) and HPD (right column) reconstruction results: effective area and angular resolution as functions of energy, distributions of angular errors in event reconstruction for upward tracks. No background noise simulated. Threshold set to 1.5 pe.

In figures 5.13 and 5.14 the results of the complete simulation including the $70\ kHz$ ^{40}K noise are shown.

In both the PMT and HPD telescopes with 0.5 p.e. cut (figure 5.13), the presence of noise hits reduces the effective area after a quality selection to $0.45\ km^2$ and $0.52\ km^2$ respectively (while the effective area for all the reconstructed events is $1.15\ km^2$ for PMT and $1.25\ km^2$ for HPD, very close to the values of figure 5.11).

Noise also degrades the angular resolution of reconstructed events, but leaves almost unaffected the resolution for events which pass the quality selection (a minimum resolution of 0.07^o and 0.11^o respectively for the HPD and PMT case). However, also before the quality cuts the HPD telescope results (0.14^o above TeV) are better than the PMT ones (0.25^o).

The median angular resolutions for upward going tracks after quality cuts are 0.12^o and 0.07^o respectively for the PMT and the HPD case.

When the 1.5 p.e. cut is applied in reconstruction (figure 5.14), almost all the ^{40}K noise is rejected in the HPD telescope: the effective areas before and after the quality selection are very close to their value in the simulation without noise, even at low energies. The PMT telescope, instead, loses accuracy in reconstruction at low energies, resulting in a further worsening of performances respect to the HPD telescope.

As already observed for the simulation without noise, the small[15] statistics below TeV energies does not allow to compare angular resolutions in this energy range. At higher energies, however, the resolution is rather good for both reconstructed and selected events. The HPD shows, as before, its better performance (by almost a factor 2) when compared with the PMT.

The angular resolution for upgoing tracks is highly better in the HPD case: though less events are reconstructed a larger fraction of them satisfies the quality cuts. The median angular resolutions for reconstructed upgoing tracks are 0.18^o (PMT) and 0.07^o (HPD), for selected tracks they are 0.12^o (PMT) and 0.06^o (HPD).

The conclusions that may be drawn from these very preliminary results are that an improvement is obtained using the HPD, in terms of angular resolution and reconstruction efficiency at low energies. The gain at low energies is unclear, because of the limited statistics obtained in this simulation.

[15] This time, no statistic at all is available for the PMT telescope! This explain the median value of 180^o for the point at $400\ GeV$.

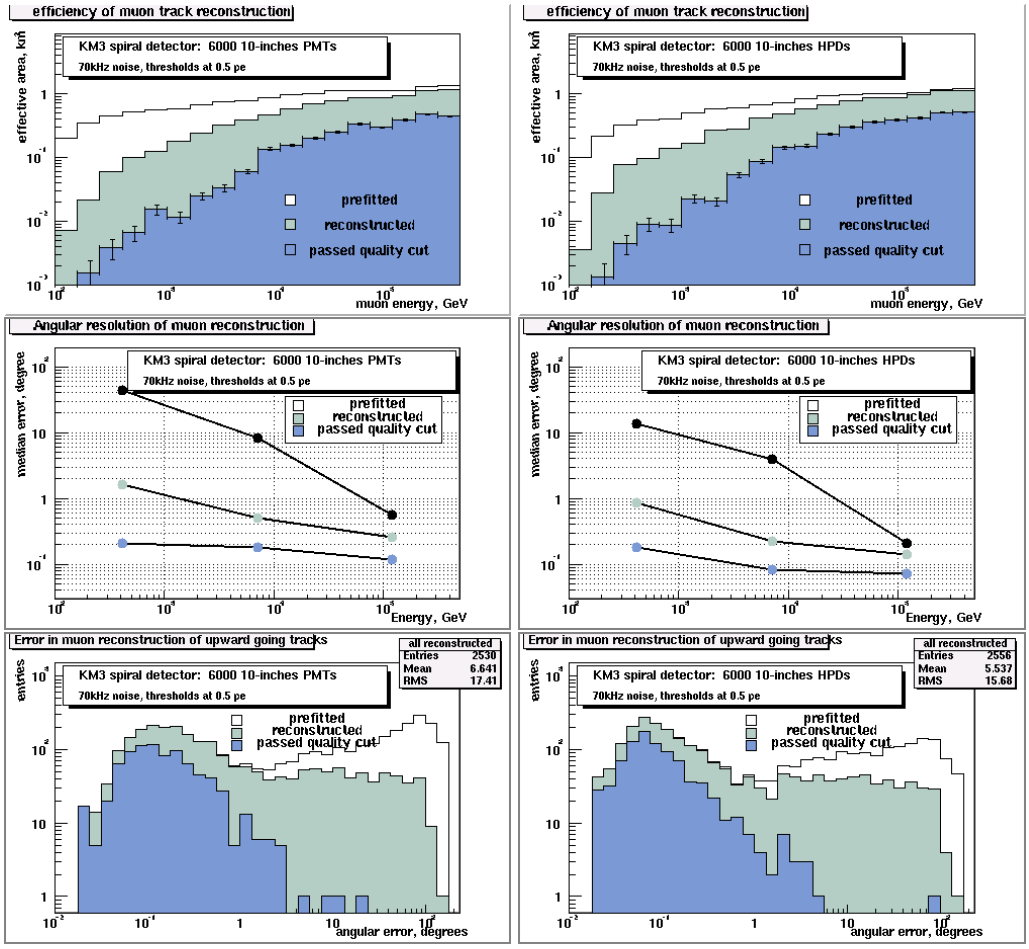

Figure 5.13: Comparison between PMT (left column) and HPD (right column) reconstruction results: effective area and angular resolution as functions of energy, distributions of angular errors in event reconstruction for upward tracks. Background is present. Threshold set to 0.5 pe.

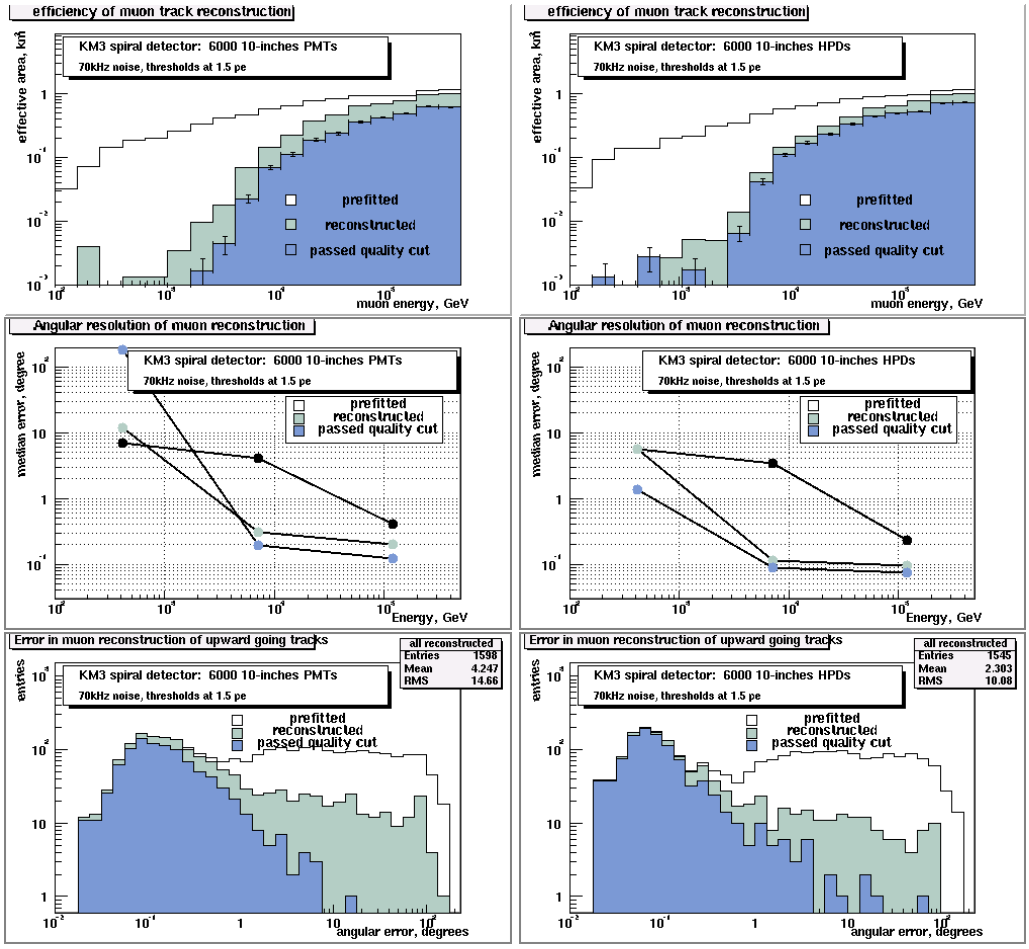

Figure 5.14: Comparison between PMT (left column) and HPD (right column) reconstruction results: effective area and angular resolution as functions of energy, distributions of angular errors in event reconstruction for upward tracks. The background is simulated. Threshold set to 1.5 pe.

5.5 A possible further improvement: the use of the spatial information by segmenting the silicon pad

The Genova group working in NEMO/ANTARES is developing and testing a light collector for multianode devices to be used in conjunction with a multianode light detector. The idea is basically an implementation of an array of Winston cones which couples the inner surface of the pressure resistant sphere with the front window of the photodetector (see figure 5.15). This collector slightly increases the light collection efficiency for directions near the normal to the axis (mainly due to the presence of the mirror at the bottom of the system, which is not oriented along a diameter of the same sphere as all the other mirrors), whereas there is a very good correspondence between incoming light direction and illuminated photocathode region. This device could then improve the recostruction of the position of the track with respect to the optical module. A complete simulation of the performance of such devices implemented in a km^3 detector is expected within the end of the year.

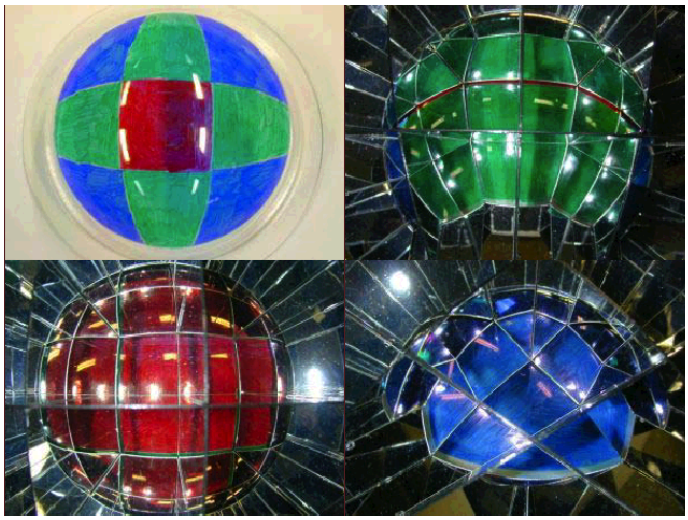

Figure 5.15: Different views of a coloured dome through the light collection. [69]

If, as coupled multianode device, the HPD is chosen, the advantage of a good pulse height spectrum is added to that following the use of the spatial information. The number of pixels (and hence the spatial resolution) is limited by the requirement of external electronics (too many feedthroughs cannot be used) and by the

point spread function of the device (in figure 5.4 one can see that the spread on the silicon sensor for each starting position is of a few mm). However the light collector itself and the recostruction program do not need too s refined spatial resolution: four (as the hybrid PMT of Genova) or seven (as the proposed HPD) pixels are enough.

If the positive advantages of the use of angular information in event reconstruction were demostrated, a detailed study of the HPD point spread function and of the possible cross talk between silicon pixels will be needed, in order to verify the concrete possibility of adopting such device.

Chapter 6

Summary and conclusions

In this work, after a discussion of the main astrophysical sources of high energy neutrinos and of experiments now underway for their detection, I have given a detailed description of the Antares experiment, in the framework of which this study has been carried out.

I have analysed in detail the most important noise sources affecting the experiment: ^{40}K radioactive decays and bioluminescence.

Using data collected in the spring of 2003 by a prototype detector, I have analysed the time behaviour of bioluminescence and its correlation with ambient variables, like sea currents. I have developed algorithms aiming at extracting from the data isolated bursts of light emission from biological sources, and studied their frequency of occurrence and shape.

The average duration of bursts, even during periods of high biological activity, is found to be substantially shorter than half a second.

The height of bursts may exceed (as expected from biology) $5\ MHz$, but small bursts of few tens of kHz above the baseline rate are 10^4 times more frequent.

I find that the shape of bursts can be well reproduced by a fast linear rise, followed by an exponential decay. From an analysis of the distribution of the decay time constant and its correlation with other burst variables an indication emerges that at least two distinct regions in the space of parameters are involved in the process.

This has been interpreted as due to the prevalence of two main emission mechanisms belonging to different biological population. A comparison with data from biology may lead to the identification of the species. Since bioluminescence is highly season-dependent, and each species may probably have a different life cycle, this information may help in planning and optimizing the operation of the

detector.

A first attempt has been made, using the same algorithms, to analyse Monte-Carlo generated bursts, provided by a member of the ANTARES collaboration. The very preliminary results I have obtained are still unsatisfactory. There is hope that, introducing in the MonteCarlo code the information I have obtained from real data, a more satisfactory simulation may be obtained.

In view of an envisaged future extension of the detector to one of a much bigger size, I have studied the possibility of replacing the conventional PMTs, now being used, with hybrid photodetectors (HPDs). I have designed one such HPD, checked its electro-optical and mechanical characteristics and computed, using an existing montecarlo program, the acceptance and background rejection power of a large detector using HPDs. The behaviour of such a detector has then been compared with one that uses conventional PMTs. The, still very preliminary, results obtained look promising.

Bibliography

Neutrino Telescopes

[1] A. Hallgren. **High-energy neutrino telescopes.** *NIMA 454 (2000) 61-72*, 2000.

[2] D. J. L. Bailey. **Calculation of effective muon ranges and application to overall effective areas.** *ANTARES-Phys/2001-07*.

[3] J. Brunner. **The refraction index at the ANTARES site.** *ANTARES-Site/2000-001*.

[4] Baikal coll. **The Baikal deep underwater neutrino experiment: results, status, future.** *Progr. Part. Nucl. Phys. 40 (1998) 391-401*.

[5] V.A. Balkanov *et al*. **The Lake Baikal Experiment.** *Nucl. Phys. B (Proc. Suppl.) 77 (1999) 486-491*.

[6] V. Ayutdinov *et al*. **Results from the BAIKAL Neutrino Telescope.** *The 28th International Cosmic Ray Conference*, 2003.

[7] V.A. Balkanov *et al*. **The BAIKAL neutrino project: status report.** *Nucl. Phys. B (Proc. Suppl.) 118 (2003) 363-370*.

[8] AMANDA coll. **The AMANDA neutrino telescope.** *Nucl. Phys. B (Proc. Suppl.) 77 (1999) 474-485*.

[9] J. Ahrens *et al.* **Search for extraterrestrial point sources of neutrinos with AMANDA-II.** *astro-ph/0309585*, 2003.

[10] J. Ahrens *et al*. **Search for Neutrino-Induced Cascades with the AMANDA Detector.** *Phys. Rev. D 67 012003*, 2003.

[11] J. Ahrens *et al.* **IceCube - the next generation neutrino telescope at the South Pole** *Nucl. Phys. B (Proc. Suppl.) 118 (2003) 388-395*.

[12] S. E. Tzamarias. **NESTOR: a deep-sea neutrino telescope.** *NIMA 502 (2003) 150-154*.

[13] L. K. Resvanis. **High-energy neutrino telescopes.** *Nucl. Phys. B (Proc. Suppl.) 122 (2003) 24-39.*

[14] E. G. Anassontzis, P. Koske. **Deep-sea station connected by cable to shore.** *Sea Technology 44, n.7,* 2003.

[15] ANTARES coll. **A Deep Sea Telescope for High Energy Neutrinos.** *astro-ph/9907432, 1999.*

[16] NEMO coll. **The NEMO project.** *Workshop on Technical Aspects of a Very Large Volume Neutrino Telescope in the Mediterranean Sea, Amsterdam, 2003*.

[17] A. Capone *et al*. **Measurements of light transmission in deep Sea with the *AC9* trasmissometer.** *NIMA 487 (2002) 423*.

[18] N. Palanque-Delabrouille. **Site comparison with test 3'.** *ANTARES-Site/2003-001*.

ANTARES

[19] W. Bednarek, G. F. Burgio, T. Montaruli. **Galactic discrete sources of high energy neutrinos.** *astro-ph/0404534*, 2004.

[20] ANTARES coll. **Technical Design Report of the ANTARES** $0.1\ km^2$ **project.** *v. 1.0, July 2001*.

[21] N. Palanque-Delabrouille. **Blue and UV transmission in the ANTARES site (Test3').** *ANTARES-Site/2001-002*.

[22] W. H. W. Schuster, D. J. L. Bailey. **Optical properties at the ANTARES Site: what we know and what we don't know from Test 3'.** *ANTARES-Site/2002-001*.

[23] L. Moscoso. **Geometrical surface area of the Antares detector.** *ANTARES-Soft/2002-013.*

[24] R. Donders. **Study of the on-shore Trigger.** *PHD-thesis, Nikhef,* 2002.

[25] S Basa, H. Lafoux. **Photomultiplier Specifications for the ANTARES Project.** *ANTARES-Opmo/1999-001.*

[26] S. Basa, H. Lafoux, F. Desages. **Photomultiplier specifications and measurement procedures for the** $0.1\ km^2$**.** *ANTARES-Prot/2000-02.*

[27] M. Karolak, H Lafoux. **Test results of 80 10" Hamamatsu PMT.** *ANTARES-Opmo/2000-7.*

[28] D. Lachartre. **ARS1 Analogue Ring Sampler** $\&$ **ARS_CONV Users Manual Version 1.9**. *ANTARES-Elec/2000-6.*

[29] A. Heijboer. **An algorithm for track reconstruction in ANTARES**. *ANTARES-Soft/2002-002.*

Optical Background

[30] N. Palanque-Delabrouille. **Optical background measurements. Test 1.6 and 1.8 in the ANTARES site, Test 1.7 in Corsica.** *ANTARES-Site/1998-002.*

[31] J. Brunner. **Simulation of** ^{40}**K signals.** *ANTARES-Site/1999-002.*

[32] H. Lafoux. ^{40}**K simulations.** *ANTARES-Opto/1999-002.*

[33] N. Palanque-Delabrouille. **Optical background measurements by test 1.10 in the ANTARES site.** *ANTARES-Site/2000-003.*

[34] F. Devillez, C. Racca. **Optical background measurements by test 1.12 in the ANTARES site.** *ANTARES-Site/2001-003.*

[35] J. P. Schuller. **Test 1.17 Results.** *ANTARES Coll. Meeting, Sept 2003.*

[36] J. Brunner. **Baseline rates and burst fraction from PSL data.** *ANTARES Coll. Meeting, Jun 2003.*

[37] **The Bioluminescence Web Page.** http://www.lifesci.ucsb.edu/∼biolum/

[38] S. Vecchio. **Burst Characterization.** *ANTARES Coll. Meeting, Sept 2003.*

[39] G. de Vries. **Simulation of bioluminescence.** *ANTARES Coll. Meeting, Dec 2003.*

[40] A. S. Cussatlegras. **Dynamique spatio R temporelle de la bioluminescence marine en Mer d'Alboran et sur le Plateau Continental Atlantique Français.** *PHD-thesis, 2001*.

[41] I. G. Priede. **Bioluminescence and ESONET.** *ANTARES Coll. Meeting, Jun 2003.*

[42] E. A. Widder. **Bioluminescence and the pelagic visual environment.** *Mar. Fresh. Behav. Physiol., vol. 35, n. 1-2, pp.1-26,* 2002.

HPD

[43] C. D'Ambrosio *et al.* **Photon counting with a hybrid photomultiplier tube.** *NIMA 338 (1994) 389-397.*

[44] C. Joram. **Large Area Hybrid Photodiodes.** *NIMB 78 (1999) 360-365,* 1999.

[45] A. Braem *et al*. **An Apparatus for the Fabrication of Large Area Hybrid Photo-Diodes.** *CERN/EP, Geneva, Switzerland,* 1998. LHCb/98-007 RICH.

[46] M. Giunta. **Sviluppo dell'HPD, un nuovo fotorivelatore per la fisica delle astroparticelle**. *Tesi di Laurea, Università di Pisa*, 2002.

[47] A. Braem. *et al*. **Development of 10-inch HPD with Integrated Readout Electronics.** *NIMA 504 (2002) 19-23,* 2003.

[48] A. Braem *et al*. **Highly segmented large-area hybrid photodiodes with bialkali photocathodes and enclosed VLSI readout electronics.** *NIMA 442 (2000) 128-135*, 2000.

[49] P. Weilhammer. **Silicon-based HPD development sensor and front ends.** *NIMA 446 (2000) 289-298,* 2000.

[50] M. Giunta. **The HPD Detector.** *Proceedings of VLVνT Workshop, Amsterdam 2003*.

Software

[51] A. Heijboer. **Description of the ANTARES data files.** *ANTARES-Soft/2002-019.*

[52] B. van Rens. **Data formats for online datafilter.** *ANTARES-Soft/2003-001*.

[53] S. Navas. **A Comparison between GEASIM and KM3 generators.** *ANTARES-Soft/1999-002*.

[54] D. J. L. Bailey. **KM3 v2r1 : User Guide.** *ANTARES-Soft/2002-006*.

[55] J. Brunner. **Available Software: muon propagation and tracking MC.** *http://antares.in2p3.fr/internal/software/codes.html#mc*.

[56] D. Zaborov. **Simulation of ANTARES KM3 detector.** *ANTARES-Soft/2002-008.*

[57] D. Zaborov. **Comparison of different KM3 designs using Antares tools.** *Proceedings of VLVνT Workshop, Amsterdam 2003*.

Other subjects

[58] A. Letessier-Selvon. **Theoretical and Experimental Topics on Ultra High Energy Cosmic Rays.** *astro-ph/0006111*, 2000.

[59] F. Halzen, D. Hooper. **High-energy neutrino astronomy: the cosmic ray connection.** *Rept. Prog. Phys. 65 (2002) 1025-1078*.

[60] R. Blanford, D. Eichler. **Particle acceleration at astrophysical shocks: A theory of cosmic ray origin.** *Phys. Rep., vol. 154, n. 1*, 1987.

[61] E. Waxman, J. N. Bahcall. **High energy neutrinos from astrophysical sources: An upper bound.** *Phys. Rev. D 59 (1999) 023002*.

[62] C. M . Hoffman *et al*. **Gamma-ray astronomy at high energies.** *Rev. Mod. Phys., vol. 71, n. 4*, 1999.

[63] SNO Coll. **First results from the Sudbury Neutrino Observatory.** *Nucl. Phys. B (Proc. Suppl.) 111 (2002) 122-127*.

[64] KamLAND Coll. **First results from KamLAND: evidence for reactor anti-neutrino disappearance**. *Phys. Rev. Lett. 90 (2003) 021802*.

[65] M. Miura. **Results from Super-Kamiokande and K2K.** *Nucl. Phys. Proc. Suppl. 111 (2002) 158-162*.

[66] L. A. Kuzmichev. **On the velocity of light signals in the deep underwater neutrino experiments.** *hep-ex/0005036*, 2000.

[67] C. M. Lederer, V. S. Shirley. **Table of Isotope, seventh edition.** *Ed's. John Wiley and Sons, Inc. New York*, 1978.

[68] R. H. Stewart. **Introduction to Physical Oceanography.** *Texas A & M University, 2003*

[69] A. Bersani. **Development of Large Effective Area and Direction Sensitive Photodetector** *Proceedings of VLVνT Workshop, Amsterdam 2003*.

Appendix A

List of acronyms

ADC	Analog to Digital Converter
ADCP	Acoustic Doppler Current Profiler
AGN	Active Galactic Nucleum
ARS	Analog Ring Sampler
ASIC	Application Specific Integrated Circuit
ATP	Adenosine TriPhosphate
BF	Burst Fraction
BL	BaseLine
BR	Branching Ratio
BSS	Bottom String Socket
CRM	Counting Rate Monitor
CTD	Conductivity Temperature Depth
DAQ	Data Acquisition
DC	Direct Current (also dc)
EM	Electromagnetic
EMC	Electro-Mechanical Cable
EO	Electro-Optical
EOC	Electro-Optical Cable
FPGA	Field Programmable Gate Array
FWHM	Full Width Half Maximum
GPS	Global Positioning System
GRB	Gamma Ray Burst
GUT	Grand Unified Theory
GPEP	General Purpose Experimental Platform

GZK	Greisen Zatzepin Kuzimin
HPD	Hybrid PhotoDyode (or Hybrid PhotoDetector)
HV	High Voltage
IBD	InterBurst Distance
IL	Instrumentation Line
JB	Junction Box
LCM	Local Control Module
LED	Light Emitting Device
MIL	Mini Instrumentation Line
MLCM	Master Local Control Module
OB	Optical Beacon
OM	Optical Module
OMF	Optical Module Frame
pe	photoelectron (also p.e.)
P2P	Peak to Peak distance
PMT	PhotoMultiplier Tube
PSD	Pulse Shape Discriminator
PSF	Point Spread Function
PSL	Prototype Sector Line
QE	Quantum Efficiency
RMS	Root Mean Square (also rms)
RoR	Read out Request
ROV	Remote Operated Vehicle
RTS	Reset Time Stamp
SC	Slow Control
SCM	String Control Module
SPE	Single Photo Electron (also s.p.e.)
SPM	String Power Module
TCP/IP	Transmission Control Protocol/Internet Protocol
TOT	Time Over Threshold
TS	Time Stamp
TT	Time Transit
TTS	Time Transit Spread
TVC	Time to Voltage Converter
UV	Ultra-Violet
W&B	Waxman-Bahcall
WF	Waveform
WIMP	Weak Interactive Massive Particle

Appendix B

Monte Carlo simulation tools

The ANTARES software, still in evolution, is organized in several packages which can be used in different combinations to build the simulation chain. The chain of programs can be separated into three steps:

- *The physics generator.* The instrumented detector volume is surrounded by a cylindrical *can*, which defines the limit of simple particle propagation versus propagation plus Čerenkov light generation. The can extends typically 3 attenuation lengths beyond the instrumented volume. The relevant numbers are illustrated in figure B.1.
  Neutrino energy generation is done according to $E^{-\gamma}$ which allows later reweighting with different flux models.
  The generation can be be done with:

  genhen It generates neutrino events in the surroundings of the detector and supports all three flavours and both interaction channels (neutral current NC and charged current CC). If the neutrino vertex is inside the can volume, all final state particles of the interaction (after hadronization and decay of short-lived particles) are stored for further processing with the Čerenkov light simulation. If the interaction occurs outside the can, only the muon is propagated to the can surface and its kinematic variables at the intersection with the can surface are stored.

  hemas-propmu It generates muon bundles from cosmic ray interactions in the atmosphere. A full simulation of the atmospheric shower is performed, followed by the propagation of the remaining muons to

the detector position. The muons are stored at the can surface for further processing. At this level an energy cut of $20\ GeV$ is applied: it is the minimum energy which can ensure that they will produce a detectable signal in the detector, since the range of less energetic particles is shorter than the distance from the can surface to the instrumented volume.

gentra It is a generator for single tracks on the can surface or within its volume. The particle nature can be chosen between all the standard GEANT types.

In case of neutrino generation, the event weight contains also a factor which takes into account the opacity of the earth as function of neutrino energy and zenith angle.

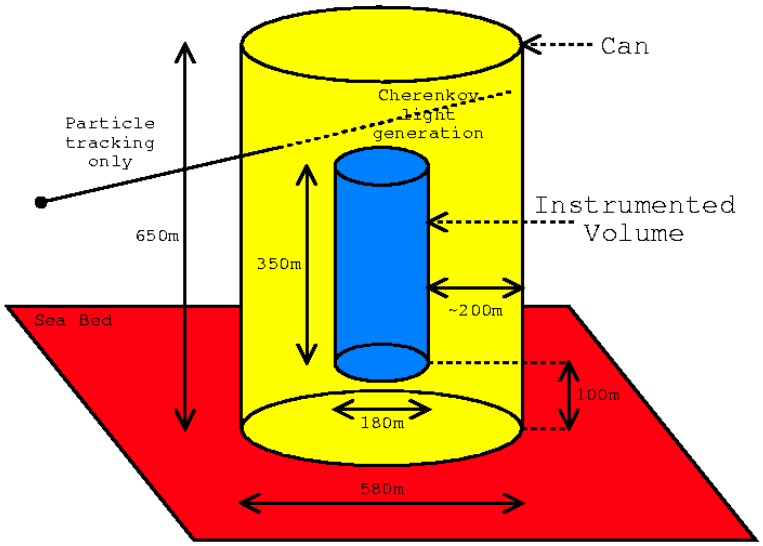

Figure B.1: Instrumented volume and "can" volume used for Čerenkov light simulation.

- *The Čerenkov light emission and propagation* (plus, if necessary, the ^{40}K background hits), simulated through:

  geasim GEANT based simulation, useful for all particle but muons. Light production of the electromagnetic showers is parametrized from

the known angular distribution of Čerenkov light emitted by an electromagnetic shower, which is independent from the initial shower energy over a wide range of energies. This allows a significant amount of CPU time to be sapred.
All long-lived particles which are stored as output of the physic generators are tracked through the water in the can volume. At each tracking step the Čerenkov cone which is produced by charged particles is calculated. For all OM which are in the cone, the hit probability is determined and converted into a photoelectron number using Poisson statistics.

km3 High energy muon simulation including the effect of light diffusion. "Scattering tables" are created by sending $1\ m$ long muon track pieces to GEANT. Differently from the above description, here individual Čerenkov photons are generated and tracked in the water. A diffusion and absorption model has been implemented which allows to track each photon through various scattering processes until it gets absorbed or leaves the volume. Each time a photon penetrates one of several concentric spheres around the muon track origin, its position, direction and time are stored in the scattering tables. Muons from physics generator events are then tracked in the usual can volume, and after each tracking step the hit probabilities for all OMs are evaluated using the scattering tables: no Čerenkov photon tracking is necessary at this step.

The composition and density of the water is adjusted to the values at the experimental site. A wave length window of $300 \div 600\ nm$ is considered and the wavelength dependent absorption length, quantum efficiency and transmission coefficients of the glass sphere and the gel are used to evaluate the hit probability. The relative orientation of the PMT with respect to the Cherenkov front and its angular acceptance is also taken into account. The arrival time is calculated based on the group velocity of the photon front and includes smearing factors from the transit time spread of the PMT as well as from the wavelength dispersion.

- *The response of the photomultiplier tubes and its digitization*. The only program which perform this step is **modk40**. The ARS behaviour is approximated by setting few parameters like integration time, dead time and saturation.

As the name itself suggests, the routine also modifies the ^{40}K contribution to the raw hits. A constant noise level is assumed, and local variations due to bioluminescence bursts are ignored in the present implementation.

Apart from these steps there are secondary inputs from calibrations and external measurements: all lines are freely floating in the sea currents and their movement must be permanently monitored. On the basis of the sea current speed the deformation of the detector lines are calculated, then data from the acoustic system and the orientation measurements are simulated including a realistic smearing for each value. Another calibration simulation is performed for the LED and laser beacons to perform an absolute time calibration for the PMTs.
No other specific simulation programs exist for other calibrations: for the main simulation of physics events one assumes usually that the detector has been calibrated and only the precision of the calibration is used as additional factor.

After these steps, the program **reco** simulates the trigger logic and performs the track reconstruction. It is based on an old FORTRAN routine called POSEIDONIA, and several reconstruction strategies may be chosen within it. The *Classic 1D Strategy* reconstructs events using a single string; it is useful for events which produce short tracks, like hadronic showers from NC interactions or electromagnetic showers from ν_e events. The *Classic 3D Strategy* reconstructs events which trigger more than one string. The *Aart Strategy* is an improvement of the standard 3D (fit and prefit) strategy which uses a maximum likelihood method that includes the likelihood of hits from background light. The *Carmona Strategy*, based on a different prefit algorithm, make use of the geometrical relationships that exist between the hits and the track due to the constant Čerenkov angle. It can be used for reconstructing events when the arrival direction is known (as for externally triggered events, like for example neutrinos from Supernovae or GRB) or in the more general case in which all the 5 parameters of the track have to be determined.

All the output data files can be transformed from ASCII files to the ROOT system format for further processing with the package antROOT.